Optics Designs of Final-Focus Systems for Future LHC Upgrades

Abelleira, J L (CERN)

18 February 2014

The EuCARD-2 Enhanced European Coordination for Accelerator Research & Development project is co-funded by the partners and the European Commission under Capacities 7th Framework Programme, Grant Agreement 312453.

This work is part of EuCARD-2 Work Package **1: Management and Communication (MANCOM)**.

Optics designs of final-focus systems for future LHC upgrades (M.Vretenar, R.S.Romaniuk, Editors), Vol24

Abelleira, J L (EPFL)

23 May 2014

The research leading to these results has received funding from the European Commission under the FP7 Research Infrastructures project EuCARD, grant agreement no. 227579.

This work is part of EuCARD Work Package **2: DCO: Dissemination, Communication & Outreach**.

Optics Designs of Final-Focus Systems for Future LHC Upgrades

THÈSE N^{O} 6113 (2014)

PRÉSENTÉE LE 18 FÉVRIER 2014
À LA FACULTÉ DES SCIENCES DE BASE
LABORATOIRE DE PHYSIQUE DES ACCÉLÉRATEURS DE PARTICULES
PROGRAMME DOCTORAL EN PHYSIQUE

ÉCOLE POLYTECHNIQUE FÉDÉRALE DE LAUSANNE

POUR L'OBTENTION DU GRADE DE DOCTEUR ÈS SCIENCES

PAR

José Luis ABELLEIRA FERNÁNDEZ

acceptée sur proposition du jury:

Prof. R. Houdré, président du jury
Prof. L. Rivkin, Dr F. Zimmermann, directeurs de thèse
Dr J.-P. Koutchouk, rapporteur
Dr T. Pieloni, rapporteur
Prof. A. F. Wrulich, rapporteur

ÉCOLE POLYTECHNIQUE
FÉDÉRALE DE LAUSANNE
Suisse
2014

"The worthwhile problems are the ones
you can really solve or help solve, the ones
you can really contribute something to."
— Richard P. Feynman

"Do not go where the path may lead,
go instead where there is no path and leave a trail."
— Ralph Waldo Emerson

Dedicated to all the people I learned something from.
Dedicated to all my teachers and professors,
to my family and very specially to my parents

Acknowledgments

The first and main acknowledgment is to my CERN supervisor, Dr. Frank Zimmermann. I really appreciate his trust in me when he accepted me as his student. I remember when we had our first interview in his town, Buxtehude. His smile and optimism motivated me to work under his supervision and encouraged me over all my Ph.D. He is not only a brilliant scientist, but also a honest and kind person.

Secondly, I want to thank my thesis advisor, Professor Leonid Rivkin, for his suggestions and support during this time. Thank you also for giving me the opportunity of working as a teaching assistant in the Masters course “Introduction to particle accelerators”, which was a very enriching experience.

I am greatly indebt with Bernard Holzer. He takes a lot of care with the students of the ABP section and his door was always open for any question I always had. I also express my gratitude to Massimo Giovanozzi, section leader of ABP-LCU.

I want to acknowledge Stephan Russenschuck, with whom I collaborated for the design of the double-half quadrupole. His expertise in accelerator magnets and in the ROXIE software were essential to accomplish a conceptual design of this new magnet.

I would like to acknowledge as well the following persons to whom I collaborated at different stages of this work: Rogelio Tomás, Héctor García, Riccardo de Maria (whose code for the magnet computation was the starting point of my LHC flat-beam calculations), Xavier Buffat (with whom I collaborated in the MD Large Piwinski Angle) and Octavio Domínguez, for the work in HE-LHC. Besides, I would like to stand out the fruitful conversations with Eduardo Marín, Stéphane Fartoukh. I want to thank also Matteo Solfarolli, Benoît Salvant and Damien Anderson.

The colleagues of INFN-LNF in Frascati deserve a special mention, among themselves Catia Milardi, Mikhail Zobov and Marica Biagini. Apart from their expertise in the crab-waist collision scheme, thanks to them I had the great opportunity to work in the control room of the DAΦNE collider, participating in the machine meetings and performing important optics measurements. I want to thank their hospitality during my two stays at LNF-INFN.

Finally, I have also some words to the people I have known in those 3 years, non-work related. Thanks to my football team El Equipo C and to my futsal team, CERN-XV. I am very proud of the excellent persons I have known and the relations I have made.

Abstract

The main topic of the thesis is the study of a novel option for the high-luminosity upgrade of the Large Hadron Collider (LHC) comprising a large Piwinski angle, flat beams, and crab waists. Flat beams and crab waists are not only pre-requisites for a crab-waist scheme, but, even by themselves; each of these two elements alone could boost the luminosity of the existing collider as built.

The new optics involves an upgrade of the interaction region of the two high-luminosity experiments, ATLAS and CMS, in order to provide them with a substantially higher luminosity. To this end, a flat-beam optics scenario has been explored for the High Luminosity LHC (HL-LHC), with a much reduced vertical beta function at the interaction point (IP), β_y^*. In addition, a large Piwinski angle is considered. Advantages of a large Piwinski angle include a reduction in the hourglass effect over the length of the collision area, which allows for the significant β_y^* decrease. In addition there is a reduction of the beam-beam effect so that the same beam-beam tune shift is reached only for much brighter beams, with a consequent luminosity increase. Flat beams and large Piwinski angle can boost the luminosity of the existing LHC as built, but they also open up the possibility to implement a crab-waist collisions scheme. The challenge here was to apply the collision concept, which so far has been employed only in the DAΦNE e^+e^- ϕ factory, to a much bigger collider with pp collisions, which do not easily allow for a symmetric optics.

The second important concept implemented in this version of the LHC upgrade is a (partially) local chromatic correction scheme, by installing chromatic sextupoles near the IP. For this purpose, the interaction region had to be redesigned. As the optics for the crab-waist scheme must be symmetric, the polarities of the final quadrupoles must change with respect to the present configuration. This includes the region where the two beams share the same aperture. In this case, a novel magnetic element called “double-half quadrupole” (DHQ) is proposed, which would provide quadrupolar fields of opposite sign at opposite locations from the centre. The element then acts as a horizontally defocusing element for either beam, and helps focusing the vertical beta-function to the small value required at the IP.

Finally, this thesis includes some considerations on applying the same optics and collision concepts to the High Energy LHC (HE-LHC) and to a design of the final-focus system for the LHeC electron line, which is also equally based on a local chromatic correction scheme.

Keywords: LHC, HE-LHC, LHeC, accelerators design, beam optics, beam dynamics, crab waist, final-focus systems, flat beams, large Piwinski angle, local chromatic correction,

luminosity.

Work supported by the European Commission under the FP7 Research Infrastructures project EuCARD, grant agreement no. 227579.

Résumé

Le thème principal de cette thèse est l'étude d'une nouvelle option pour le programme d'augmentation de la luminosité du Grand Collisionneur de Hadrons (LHC), option réalisée avec un grand angle de Piwinski, des faisceaux plats, et des « crab waists ». Les faisceaux plats et le grand angle de Piwinski sont nécessaires dans le cadre d'un système de « crab waists », mais il est important de noter que chacun de ces deux éléments peut aussi être utilisé seul pour permettre d'augmenter la luminosité du LHC.

La nouvelle optique implique une modification de la région d'interaction des deux expériences à haute luminosité, ATLAS et CMS, dans le but de leur fournir une luminosité nettement plus élevée. À cette fin, un scénario de faisceau plats a été exploré pour le HL-LHC, avec une fonction beta verticale très réduite au point d'interaction (IP), β_y^*. En outre, un grand angle de Piwinski est considéré. Les avantages d'un grand angle de Piwinski comprennent une réduction de l'effet sablier sur la longueur de la zone de collision, ce qui permet la diminution significative de β_y^*. Par ailleurs, il y a une réduction de l'effet faisceau-faisceau de sorte qu'une déviation donnée du nombre d'onde dû à cet effet faisceau-faisceau peut être atteinte pour les faisceaux beaucoup plus brillants, ce qui permettrait d'augmenter la luminosité. Faisceaux plats et grand angle de Piwinski ouvrent aussi la possibilité de mettre en œuvre un régime de collisions dit « crab waists ». Le défi ici était d'appliquer ce concept de collision — qui jusqu'à présent n'a été employé que dans le collisionneur d'électrons et de positrons DAΦNE — à un collisionneur protons-protons de grande taille qui ne se prête pas facilement à l'utilisation d'une optique symétrique.

Le deuxième concept important mis en œuvre dans cette version de plan d'amélioration du LHC est un schéma (partiel) de correction locale de la chromaticité, à l'aide de sextupôles chromatiques qui devraient être installés près de l'IP. A cet effet, la région d'interaction doit être redessinée. Comme l'optique du régime de crab waist doit être symétrique, la polarité des quadripôles finaux doit changer par rapport à la configuration actuelle. Cela inclut également la région où les deux faisceaux ont la même ouverture. Dans ce cas, un nouveau élément magnétique intitulé "quadripôle double moitié" (DHQ) est proposé, qui permettrait des champs quadripolaires de signe opposé de part et d'autre du centre. L'élément se comporte alors comme un élément défocalisant horizontal pour les deux faisceaux, et aide à l'obtention d'une valeur réduite de la fonction beta verticale à l'IP.

Finalement, cette thèse comporte des considérations sur l'application de cette optique et de ces concepts de collision au projet de LHC aux Hautes Energies (HE-LHC) et à une conception du système de focalisation final pour la ligne d'électrons du LHeC, qui est également basé sur un schéma de correction locale de la chromaticité.

Mots-clés : LHC, HE-LHC, LHeC, conception d'accélérateurs, optique des faisceaux, dynamique des faisceaux, crab-waists, faisceaux plats, grand angle Piwinski, correction locale de la chromaticité, luminosité.

Travail soutenu et financé par la Commission Européenne dans le cadre du projet FP7 Infrastructures de recherche EuCARD, convention de subvention no. 227579.

Introduction

This thesis work concerns the study of novel final-focus concepts for LHC upgrades. Its main part is the design of a new symmetric interaction region for a high luminosity LHC, but it covers as well a few closely related topics for other proposed future LHC upgrades. In the following, a synopsis is given of the work reported in each thesis chapter.

Chapter 1 introduces the beam dynamics concepts used throughout this thesis, from the most basic on single-particle dynamics to the processes related with the collision and with the emission of synchrotron radiation. It includes a complete deduction of the conditions for a chromatic correction with sextupoles, together with a description of different schemes for the aberration compensation, some of them essential for core parts of this thesis work.

The structure of the LHC is presented in Chapter 2. Several aspects are explained, like its flexibility for adapting to different interaction-region optics constraints and its chromatic correction. It also includes a small overview of the future plans. Of importance here is the study of the optical symmetric properties of accelerators in general and of the LHC in particular, as a starting point for the discussion of flat beam optics in the subsequent chapters.

Chapter 3 contains the new concepts involved in this work. It includes reports on experimental studies of collisions with a large Piwinski angle at the LHC and on crab-waist collisions at DAΦNE. The concept of the local chromatic correction is also explained. Finally, a new quasi-flat beam optics developed for the present LHC is discussed, including the complete squeeze process.

The concept of a new interaction region (IR) for the two high luminosity experiments is introduced and developed in Chapter 4 using the elements explained in Chapter 3. A conceptual design of this radically new interaction region is presented, including a local chromatic correction scheme in both transverse planes, pointing out its differences with respect to the present LHC interaction region scheme. In this context a new magnetic element is introduced and described, which allows for a vertical focusing of the two transversely displaced beams.

Chapter 5 includes an improved version of the IR optics of Chapter 4, with different IP parameters and with a local chromatic correction in the vertical plane only. The work is complemented by tracking simulations that demonstrate the cancellation of the chromatic aberrations, and by some consideration on the corresponding injection optics.

Chapter 6 summarizes two projects for future colliders to be installed in, or around, the

LHC tunnel. In the particular case of the HE-LHC, the requirements discussed in Chapter 4 are adapted to, and optimized for, the parameters of the new collider, including a discussion on the dynamic evolution of the beam parameters in the presence of crab-waist collisions.

Finally, Chapter 7 describes the layout of the LHeC electron line. Different final-focus designs are presented and compared, two of them involving the local chromatic correction.

Each chapter of the thesis contains some partial conclusions, but the general final conclusions are drawn in Chapter 8.

Original contributions related to this thesis

The main original contributions of this thesis can be summarized as:

- Comparison of different chromatic correction schemes for colliders.
- Study of the LHC optical properties and its chromatic correction.
- Formulation of a set of symmetry relations for the matching of the Twiss functions between the interaction region and the arcs.
- Study of four novel concepts for an LHC luminosity upgrade: local chromatic correction, colliding flat beams, large Piwinski angle, and crab-waist collisions.
- Conceptual design of two interaction regions with different IP parameters and configurations, both of them fully matched to the LHC ring.
- Design of a new magnetic element fulfilling the specific needs of the new IR, in collaboration with an expert from the CERN magnet group.
- Parameter study for a symmetric HE-LHC with large Piwinski angle.
- Design and comparison of several different LHeC final-focus systems for the electrons, two of them involving a local chromatic correction. Study of the synchrotron radiation emitted by the electrons.

With regard to experimental work, this thesis reports crab-waist beam studies performed in the DAFNE collider at INFN-LNF (Frascati, Rome), in November 2012. It also includes a machine development study on the Large Piwinski Angle in the LHC from July 2012, and the full preparation (optics development of a complete squeeze sequence, already verified without beam) for an LHC flat-beam machine study.

Contents

List of Figures

List of Tables

1. Concepts of Beam Dynamics

The basic concepts of beam dynamics are introduced, with a brief description of the different elements used in particle accelerators. The LHC is a particle collider and the concepts related to the collision and interaction between the two beams are also explained in this chapter.

1.1 Motion in Particle Accelerators

Lorentz Force

In a particle accelerator, particles with charge q and velocity $\boldsymbol{v}$ are guided in vacuum pipes under the influence of electric, $\boldsymbol{E}$, and magnetic fields, $\boldsymbol{B}$, through the Lorentz force:

$$\boldsymbol{F}_L = q(\boldsymbol{E} + \boldsymbol{v} \times \boldsymbol{B}). \tag{1.1}$$

Magnetic fields are generally used to deflect or focus, but in the presence of only magnetic fields, the Lorentz force is always perpendicular to the velocity and does not change the energy of the particles. For that, electric fields are used. As most of the particle colliders are ultrarelativistic, i.e., $v = \|\boldsymbol{v}\| \sim c$, the momentum vector, $\boldsymbol{p} = \gamma_r m_0 \boldsymbol{v}$, describes better the dynamic state, where m_0 represents the rest mass and γ_r is the relativistic factor, given as $\gamma_r = \frac{1}{\sqrt{1-\beta_r^2}}$, with $\beta_r = \frac{v}{c}$.

The Reference System

The closed orbit of a circular accelerator is the trajectory of the beam particles averaged over many revolutions. The particle motion is described in a coordinate system that moves with the particle along the reference orbit (Fig. 1.1). The ideal path is defined geometrically only by straight sections and bending magnets. Higher order magnets do not influence this path, if the particle passes through the center of the elements; they only provide focusing or defocusing forces that may help keep the particles close to the reference path. For large machines as the LHC, the dynamics of the longitudinal plane, {z}, can be decoupled from that of the transverse ones, {x,y}. The dynamics in the transverse plane involves the control of the beam size by magnetics fields. The dynamics in the longitudinal plane is basically

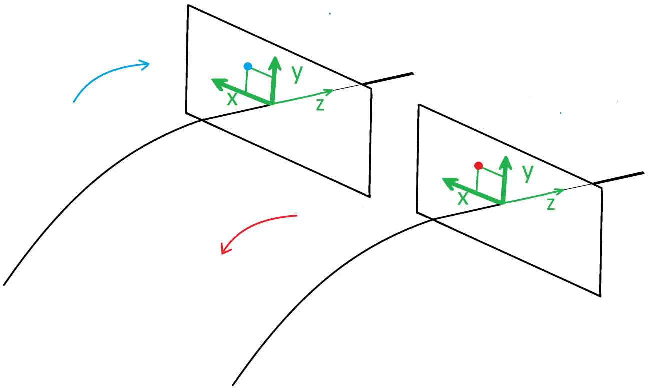

Figure 1.1: Coordinate system used for accelerators. The case shown refers to a double aperture accelerator where each beam has its own reference system (like LHC). The direction is indicated by the arrows. A longitudinal position in the accelerator is expressed by the s coordinate. In this particular case, the longitudinal coordinate has the same value for the two particles, but the transverse coordinates are referred to their respective reference system.

controlled by longitudinal electric fields from radio frequency cavities and also depends on the transverse optics, through the momentum compaction factor. This thesis is focused on transverse dynamics.

Equations of Motion

The magnetic fields are perpendicular to the movement of the particles, assuming the longitudinal component to be zero. In the reference system sketched in Fig. 1.1, the magnetic field can be written as

$$\boldsymbol{B} = (B_x, B_y, 0). \tag{1.2}$$

The transversal components of the velocity are normally much smaller than the longitudinal ones, $v_{x,y} \ll v_s$. Then, the following simplification can be made, when computing the transverse forces,

$$\boldsymbol{v} \approx (0, 0, v). \tag{1.3}$$

Substituting $\boldsymbol{E} = \mathbf{0}$, (1.2) and (1.3) in (1.1), the resultant Lorentz force is obtained

$$\boldsymbol{F}_L = q(-vB_y, vB_x, 0). \tag{1.4}$$

In circular accelerators, the particles encounter the same elements on each turn. To exploit this periodicity, the independent variable t is replaced by the arc length s, $s = vt$ along the design orbit of the ring. The second Newton's law can then be written as

$$F_x = m\frac{d^2x}{dt^2} = mv^2\frac{d^2x}{ds^2}, \qquad F_y = m\frac{d^2y}{dt^2} = mv^2\frac{d^2y}{ds^2}. \tag{1.5}$$

The following notation is used to express derivation with respect to the arc length, equivalent for y with $y \leftrightarrow x$:

$$x' = \frac{dx}{ds}, \qquad x'' = \frac{d^2x}{ds^2}. \tag{1.6}$$

The force acting in the vertical plane is just the magnetic one. In the horizontal plane, a centrifugal term must be added (mv^2/r) to compute the resultant force. In fact, the moving reference system is in general a non-inertial one. Only in the straight sections, when $r \to \infty$, the centrifugal term is zero and the reference system can be considered as inertial. We write the transverse forces as:

$$F_x = \frac{mv^2}{r} + F_{L,x}, \qquad F_y = F_{L,y}. \tag{1.7}$$

Substituting (1.4) and (1.5) in (1.7) and using (1.6), the equations of the transverse motion are obtained:

$$x'' = \frac{1}{r} - \frac{q}{p}B_y, \qquad y'' = \frac{q}{p}B_x. \tag{1.8}$$

These equations must be solved for each magnetic field distribution, $B_x = B_x(x, y, s)$, $B_y = B_y(x, y, s)$; and for each momentum, p. They have the form of a Hill's equation [3]. Usually the momentum of a particle is referred with respect to a reference momentum p_0 (which in an ideal distribution of particles represents the average value of the momentum of the particles), as

$$\delta = \frac{p - p_o}{p_0} = \frac{\Delta p}{p_0}. \tag{1.9}$$

Then, δ represents the relative deviation of the momentum of a particle with respect to the central value of the distribution. It is usually called the relative momentum deviation. From now on, p will represent the reference momentum and the actual momentum of the particle will be represented by $p(1+\delta)$. Particles with $\delta \neq 0$ are called off-momentum particles. The term $\frac{1}{p}$ in (1.8), now redefined as $\frac{1}{p(1+\delta)}$ can be linearly approximated by the first term of its Taylor series expansion

$$\frac{1}{p(1+\delta)} \approx \frac{1}{p}(1-\delta). \tag{1.10}$$

On the other hand, the components of the magnetic field at each longitudinal point can be expanded as (see [1, Sec. 3.1.5]):

$$B_x(x, y) = gy + g_s xy + \frac{1}{3!}g_o(3x^2y - y^3) + \ldots \tag{1.11}$$

$$B_y(x, y) = B_{y,0} + gx + \frac{1}{2}g_s(x^2 - y^2) + \frac{1}{3!}g_o(x^3 - 3xy^2) + \ldots \tag{1.12}$$

where $B_{y,0}$ is the dipolar field and g ,g_s, g_o are the quadrupolar, sextupolar and octupolar components, respectively. In accelerator physics it is usual to normalize the field components by the ratio p/q, called the magnetic rigidity. The normalized quadrupolar, sextupolar and octupolar components are:

$$k = \frac{q}{p} g, \qquad k_s = \frac{q}{p} g_s, \qquad k_o = \frac{q}{p} g_o. \tag{1.13}$$

These coefficients are modified for the off-momentum particles, in linear approximation, as $k_n \approx k_n(1-\delta)$. For a particle which has a certain x coordinate in a curved section, the radius is $r = \rho + x$. Using $\frac{1}{r} = \frac{1}{\rho+x} \approx \frac{1}{\rho}(1 - \frac{x}{\rho})$, substituting the fields (1.11) and (1.12) in (1.8), and replacing $\frac{1}{p} \to \frac{1}{p}(1-\delta)$ (first order expansion), the equation of motion is obtained for a particle with momentum deviation δ. In the presence of only dipolar and quadrupolar fields the linear equations of motion are obtained as:

$$x'' + \left[\frac{1}{\rho^2} + k(1-\delta) \right] x = \frac{1}{\rho} \delta, \tag{1.14}$$

$$y'' - k(1-\delta) y = 0. \tag{1.15}$$

The basic solutions of (1.14) and (1.15) are of the form:

$$\{x(s), y(s)\}_1 = \sqrt{J_{x,y} \cdot \beta_{x,y}(s)} \cdot \sin[\Delta\mu_{x,y}(s)], \tag{1.16}$$

$$\{x(s), y(s)\}_2 = \sqrt{J_{x,y} \cdot \beta_{x,y}(s)} \cdot \cos[\Delta\mu_{x,y}(s)]; \tag{1.17}$$

where the amplitude term $J_{x,y}$ is the action of the particle for each degree of freedom and is a constant of motion. The functions $\beta_{x,y}(s)$ are called the optical beta functions or just betatron functions, and they fulfill the following differential equation,

$$\frac{1}{2} \beta_{x,y}(s) \cdot \beta''_{x,y}(s) - \frac{1}{4} \beta'^2_{x,y}(s) + K_{x,y}(s) \cdot \beta^2_{x,y}(s) = 1, \tag{1.18}$$

where $K_{x,y}(s)$ is given at each point as a function of the local curvature radius and of the quadrupole strength:

$$K_x = \frac{1}{\rho^2} + k, \qquad K_y = -k. \tag{1.19}$$

The function $\Delta\mu(s)$ represents the betatron phase advance between the points s_0 and s of the accelerator,

$$\Delta\mu_{x,y}(s) = \int_{s_0}^{s} \frac{1}{\beta_{x,y}(\tau)} \mathrm{d}\tau. \tag{1.20}$$

The phase advance between two points gives the phase of the oscillation each particle performs between the initial and the final point. Dividing the phase advance by 2π the number of oscillations is obtained. In particular, selecting the initial and the final points as the same point of the ring (i.e., integrating over the whole length L), one obtains what is called the tune of the machine for each plane $\{x, y\}$,

$$Q_{x,y} = \frac{1}{2\pi} \int_{s_0}^{s+L} \frac{1}{\beta_{x,y}(\tau)} \mathrm{d}\tau. \tag{1.21}$$

From the β-function another two optical functions can be defined as

$$\alpha_{x,y}(s) = -\frac{1}{2}\beta'_{x,y}(s), \qquad \gamma_{x,y}(s) = \frac{1+\alpha^2_{x,y}(s)}{\beta_{x,y}(s)}. \tag{1.22}$$

A more detailed description of these functions, called “Twiss functions” can be found in [2]. For the linear motion considered up to now, any solution can be expressed as a linear combination of the basic solutions (1.16) and (1.17). This yields the relative position of the particle with respect to the reference orbit. The transverse momenta are given by

$$p_{x,y} = \gamma_r m_0 \frac{d\{x, y\}}{dt}, \tag{1.23}$$

where m_o is the rest mass of the particle. Usually, instead of the transverse momentum, its value normalized to the total momentum is given

$$\frac{p_{x,y}}{p_0} = \{x', y'\} = \tan\theta_{x,y} \approx \theta_{x,y}. \tag{1.24}$$

As $p_{x,y} << p_z$ the tangent can be approximated by its angle (paraxial approximation). For the purpose of this thesis, the state of a particle can be described by a set of five variables, which are sufficient for the analysis of the transverse motion:

$$(x, x', y, y', \delta). \tag{1.25}$$

1.2 Magnetic Elements and Chromatic Correction

The magnetic elements are responsible for guiding the particles and for keeping them in the vacuum pipe. Usually they are electromagnets, powered at high currents, but some accelerators make use of permanent magnets. In this thesis, an example of the first case are the LHC superconducting magnets, while some DAΦNE magnets are permanent. The basic magnetic elements are described in this section.

The Dipole Magnet. Dispersion Function

Bending magnets are elements that create a magnetic field with only one component, generally the vertical one, in order achieve a horizontal bending. All the terms in (1.11) and (1.12) are zero except the dipolar one, $B_{y,0}$. These are the elements that define the geometry of the ring. A bending magnet is characterized by its length (L_d) and by its curvature radius (ρ). It deflects particles of different momenta according to

$$B\rho = \frac{p(1-\delta)}{q}. \tag{1.26}$$

In a synchrotron, such as the LHC, the magnetic field varies with the momentum of the particles during the acceleration process so as to keep the closed orbit near the center of the pipe of the bending magnet, that is, to keep ρ constant:

$$B(t) = \frac{p(t)}{q\rho}(1-\delta). \tag{1.27}$$

The maximum magnetic field defines the maximum attainable momentum. That means the curvature radius of the beam pipe must be designed taking into account the maximum magnetic field and the maximum momentum. However, the particles in a beam do not all have exactly the same energy, but they exhibit a certain momentum spread. As a consequence, the more energetic particles describe trajectories with a larger curvature radius (Fig. 1.2). Its difference with respect to the radius of the particles with nominal momentum is

$$\Delta\rho(\delta) = \frac{p}{qB}\delta. \tag{1.28}$$

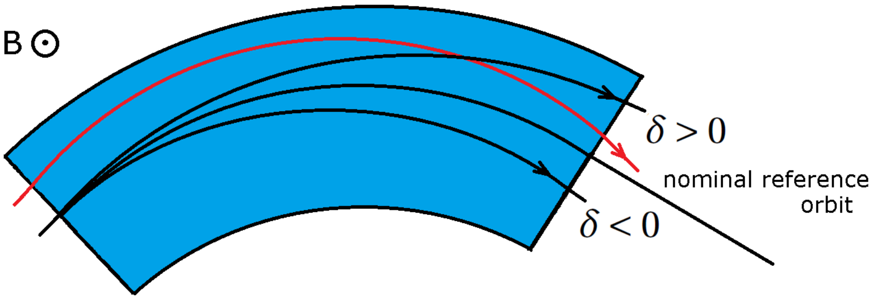

Figure 1.2: Trajectories of particles with different energies in a dipole magnet (in black). A particle with nominal energy and $x > 0$ at the beginning of the dipole (in red) is focused at the end, illustrating the effect of the weak focusing.

At the exit of the bending magnet, the off-momentum particles end up with a different horizontal coordinate. Therefore, particles of different energies have different "closed orbits". Due to the momentum spread, the transverse coordinates $\{x, y\}$ have in general two contributions, one given by (1.16,1.17) and usually represented as $\{x_\beta, y_\beta\}$, and another one due to the effect of the dispersion. The two effects are condensed in the following equation

$$\{x(s,\delta), y(s,\delta)\} = \{x_\beta(s), y_\beta(s)\} + D_{x,y}(s)\cdot\delta + \frac{1}{2}D'_{x,y}(s)\cdot\delta^2 + \frac{1}{3!}D''_{x,y}(s)\cdot\delta^3 + ..., \tag{1.29}$$

where $D_{x,y}(s)$ is the first order dispersion, which plays an essential role in the chromatic correction, as will be explained in Sec. 1.2. $D'(s), D''(s), \ldots$ are higher order dispersion terms.

If a bending magnet is made as a sector magnet, as that of Fig. 1.2, it also has a focusing effect called “weak focusing”. This is represented by the term $1/\rho^2$ in (1.19). The figure shows how the particles with a horizontal transverse coordinate larger than zero experience a a longer path. The integrated effect of the magnetic field is bigger and the particle is focused to the reference orbit. Particles with $x < 0$ experience a weaker integrated effect and are focused as well.

The Magnetic Quadrupole. Chromaticity and Geometric Aberrations

The magnetic field of a pure quadrupole is taken from (1.11) and (1.12) with $B_{y,0} = 0$ $g_s = 0$, $g_o = 0$:

$$B_x = gy, \tag{1.30}$$

$$B_y = gx. \tag{1.31}$$

Figure 1.3 shows the sketch of a quadrupole magnet with positive strength. In the particular case shown it has a focusing effect in the horizontal plane while it defocuses the particles in the vertical one. Integrating the equations of motion for this element we obtain

$$x'' + k(1-\delta)x = 0, \tag{1.32}$$

$$y'' - k(1-\delta)y = 0; \tag{1.33}$$

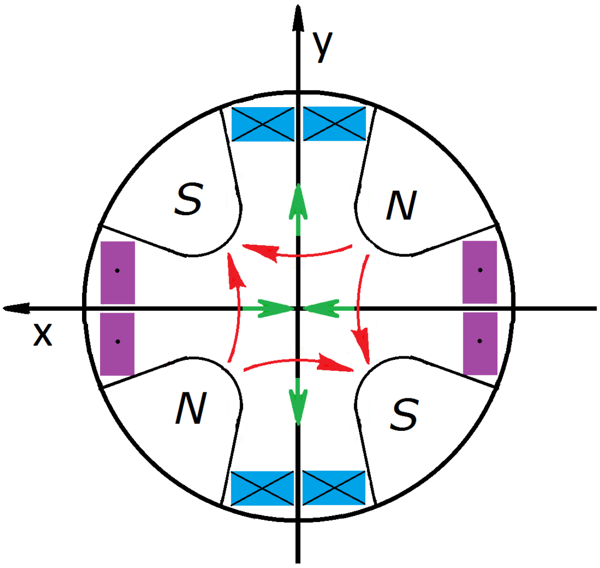

Figure 1.3: Cross section of a quadrupole magnet with $k > 0$. The magnetic field lines are indicated in red and the resultant force is shown in green, for a particle moving into the plane of the cross section with positive charge. The coils with current flowing into the plane are represented with a ‘×’ in blue color, and for current coming out from the plane in purple with a ‘·’.

so that the change in the angle that a particle experiences over a passage through a quadrupole becomes

$$\Delta x' = -\int_{L_q} k(1-\delta)x\,ds, \tag{1.34}$$

$$\Delta y' = \int_{L_q} k(1-\delta)y\,ds, \tag{1.35}$$

where L_q is the magnetic length of the quadrupole.

Henceforth, $\Delta x'$ and $\Delta y'$ represent the so-called horizontal and vertical kicks, respectively. A positive sign in k indicates a focusing effect and a negative a defocusing one. As the two have different signs, a quadrupole focuses in one plane and defocuses in the other. Therefore, quadrupoles of opposite sign must be combined in an accelerator lattice by alternating their sign, in order to provide an overall focusing in the two planes. This was first proposed by E. D. Courant and H. S. Snyder in 1958 [2] and is still the base for present accelerator design. Assuming that the element is thin, we can consider that the kick occurs in an infinitely small length and there is consequently no change in x and y along the element. This is called the thin-lens approximation. Defining the quadrupole integrated strength as $k_l = \int_{L_q} k\,ds \approx kL_q$, the kicks in the horizontal (1.34) and in the vertical plane (1.35) can be written as

$$\Delta x' = -k_l x + k_l \delta x, \tag{1.36}$$

$$\Delta y' = k_l y - k_l \delta y. \tag{1.37}$$

The first term in each equation represents the focusing/defocusing effect, as the kick is proportional to the position. The second term of each equation describes a decrease in the mentioned effect for positive off-momentum particles and is called chromatic aberration. In linear and circular colliders this also leads to an enlargement of the beam size (Sec. 1.4). Chromaticity has another effect on beam stability that will be explained later in Sec. 1.5. Chromaticity is in general corrected by placing sextupoles at specific locations.

The Magnetic Sextupole. Chromatic Correction

Sextupoles are used to correct chromaticity. The magnetic field of a pure sextupole is taken from (1.11) and (1.12) with $B_{y,0} = 0$, $g = 0$, $g_o = 0$, as

$$B_x = g_s xy, \tag{1.38}$$

$$B_y = \frac{1}{2} g_s (x^2 - y^2). \tag{1.39}$$

The magnetic poles and field lines of a sextupole with positive strength are shown in Fig. 1.4. The kick given by a sextupole is

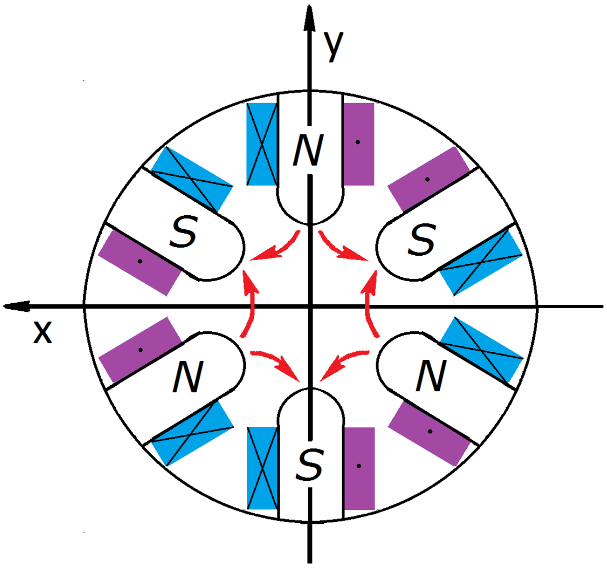

Figure 1.4: Cross section of a sextupole magnet with $k_s > 0$. The magnetic field lines are indicated in red. The color convention for coil currents is the same as used for the quadrupole in Fig. 1.3.

$$\Delta x' = -\int_{L_s} \frac{1}{2} k_s (x^2 - y^2)\, ds, \tag{1.40}$$

$$\Delta y' = \int_{L_s} k_s xy\, ds. \tag{1.41}$$

where L_s is the length of the sextupole. Considering the thin-lens approximation and introducing the integrated sextupole strength, $k_{sl} = \int_{L_s} k_s\, ds \approx k_s L_s$, the kick given by the sextupole can be written as

$$\Delta x' = -\frac{1}{2} k_{sl} (x^2 - y^2), \tag{1.42}$$

$$\Delta y' = k_{sl} xy. \tag{1.43}$$

Here we assume that the vertical chromaticity is zero, and we denote the horizontal one as $D_x \equiv D$. Taking into account the effect of dispersion we substitute $x = x_\beta + D\delta$ (1.29) in (1.42) and (1.43), so that the sextupole kick can be written as:

$$\Delta x_1' = -\left[\frac{1}{2}({x_{\beta,1}}^2 - y_1^2) + \frac{1}{2} D_1^2 \delta^2 + x_{\beta,1} D_1 \delta\right] k_{sl1}, \tag{1.44}$$

$$\Delta y_1' = (x_{\beta,1} y_1 + y_1 D_1 \delta) k_{sl1}. \tag{1.45}$$

In this case we have considered only the presence of linear horizontal dispersion. The terms $-x_{\beta,1} D_1 \delta k_{sl1}$ in (1.44) and $y_1 D_1 \delta k_{sl1}$ in (1.45) have the potential to correct the chromatic aberrations induced by $k_1 \delta x$ in (1.36) and $-k_1 \delta y$ in (1.37). However, the sextupole introduces the additional terms $-\frac{1}{2}({x_{\beta,1}}^2 - y_1^2) k_{sl1}$ and $x_{\beta,1} y_1 k_{sl1}$. Those terms are called geometric aberrations. To cancel them, another sextupole is needed. A standard scheme of chromatic correction in linear colliders consists of two pairs of sextupoles, each of them correcting chromaticity in one plane, and cancelling the geometric aberration mutually. The corresponding kicks introduced by the second sextupole are:

$$\Delta x_2' = -\left[\frac{1}{2}({x_{\beta,2}}^2 - y_2^2) + \frac{1}{2}D_2^2\delta^2 + x_{\beta,2}D_2\delta\right] k_{sl2}, \tag{1.46}$$

$$\Delta y_2' = (x_{\beta,2}y_2 + y_2D_2\delta)k_{sl2}. \tag{1.47}$$

There are different ways to cancel the aberrations by using a second sextupole. The scheme followed here is sketched in Fig. 1.5. Here the quadrupoles and sextupoles are considered as thin lenses and located in two positions: one for the quadrupole and sextupole 1, and the other for quadrupole and sextupole 2. One of the possible ways to arrange the second sextupole is to have a $-I$ transformation (see (A.7)) in both planes with respect to the first sextupole. The sextupoles then must also have the same strength, $k_{sl1} = k_{sl2} = k_{sl}$. The $-I$ separation means $x_{\beta,2} = -x_{\beta,1}$, $x_2' = -x_1'$, $y_2 = -y_1$ and $y_2' = -y_1'$. This transformation between two elements can be made with $\beta_1 = \beta_2$, $\Delta\mu = \mu_2 - \mu_1 = \pi$ and $\alpha_1 = \alpha_2$. The angles just after sextupole 2 are

$$x' = -(x_0' + \Delta x_1') + \Delta x_2' = -x_0' + \left[\frac{1}{2}D_1^2\delta^2 - \frac{1}{2}D_2^2\delta^2 + x_{\beta,1}D_1\delta + x_{\beta,1}D_2\delta\right] k_{sl}, \tag{1.48}$$

$$y' = -(y_0' + \Delta y_1') + \Delta y_2' = -y_0' - y_1(D_1 + D_2)\delta k_{sl}. \tag{1.49}$$

The geometric aberrations, $\frac{1}{2}({x_{\beta,i}}^2 - y_i^2)$ and $x_{\beta,i}y_i$ have been cancelled, leaving only the chromatic terms and the second order dispersion terms of the quadrupoles. For $D_1 = 0$:

$$x' = -x_0' - \frac{1}{2}D_2^2\delta^2 k_{sl} + x_{\beta,1}D_2\delta k_{sl}, \tag{1.50}$$

$$y' = -y_0' - y_1D_2\delta k_{sl}. \tag{1.51}$$

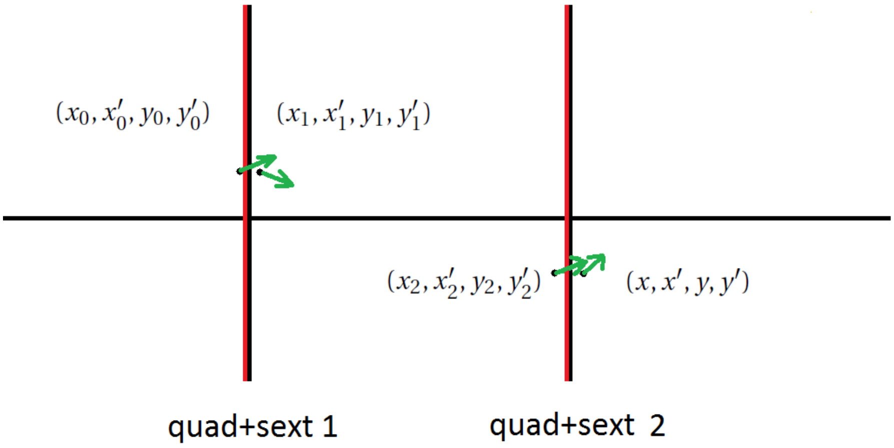

Figure 1.5: Scheme of the kicks for deduction of sextupole compensation. The state of the particle is represented by (x_0, x_0', y_0, y_0') (just before quad+sext 1), (x_1, x_1', y_1, y_1') (just after quad+sext 1), (x_2, x_2', y_2, y_2') (just before quad+sext 2) and (x, x', y, y') (just after quad+sext 2).

If instead of $D_1 = 0$, the dispersion is the same in the two sextupoles, $D_1 = D_2$, also the second order dispersion generated by the sextupoles is cancelled, namely

$$x' = -x'_0 + 2x_{\beta,1} D_2 \delta k_{sl}, \tag{1.52}$$

$$y' = -y'_0 - 2y_1 D_2 \delta k_{sl}. \tag{1.53}$$

In general, for $\Delta\mu_x = \pi, \Delta\mu_y = \{0, \pi\}$, the aberrations are cancelled if

$$\frac{1}{2}(D_1^2 - D_2^2) k_{sl} = k_l (D_1 - D_2), \tag{1.54}$$

$$(D_1 + D_2) k_{sl} = 2k_l. \tag{1.55}$$

so that we get the general relation between the sextupole and quadrupole strengths, for chromatic aberration compensation,

$$k_{sl} = \frac{2k_l}{D_1 + D_2}. \tag{1.56}$$

Another way to cancel geometric aberrations is with a $+I$ transformation in x and $-I$ in y, and using sextupoles of opposite strength, $k_{sl1} = -k_{sl2} = -k_{sl}$:

$$x' = (x'_0 + \Delta x'_1) + \Delta x'_2 = x'_0 + \left(\frac{1}{2} D_1^2 \delta^2 - \frac{1}{2} D_2^2 \delta^2 + x_{\beta,1} D_1 \delta - x_{\beta,1} D_2 \delta\right) k_{sl}, \tag{1.57}$$

$$y' = -(y'_0 + \Delta y'_1) + \Delta y'_2 = -y'_0 + (y_1 D_1 \delta - y_1 D_2 \delta) k_{sl}. \tag{1.58}$$

But now we have to take into account that the quadrupole is in a dispersive region. Then, Eq. (1.36) must be rewritten, substituting $x = x_\beta + D\delta$, as

$$\Delta x' = -k_l x_\beta - k_l D\delta + k_l \delta x_\beta + k_l D\delta^2. \tag{1.59}$$

So that for $\Delta\mu_x = 0$, $\Delta\mu_y = \pi$, the conditions for aberration cancellation are

$$\frac{1}{2}(D_1^2 - D_2^2) k_{sl} = -k_l (D_1 + D_2), \tag{1.60}$$

$$(D_1 - D_2) k_{sl} = -2k_l. \tag{1.61}$$

Relations (1.60) and (1.61) also apply for $\Delta\mu_x = 0$, $\Delta\mu_y = 0$. Then, the relation for aberration compensation in both cases is

$$k_{sl} = -\frac{2k_l}{D_1 - D_2}. \tag{1.62}$$

The four cases are summarized in Table 1.1.

The solution of cases with $\Delta\mu_x = \pi$ gives a minimum k_{sl} for a maximum value of $(D_1 + D_2)$. As the phase advance for the horizontal plane in both cases is $\Delta\mu_x = \pi$, in the presence of only quadrupoles and sextupoles, $D_2 = D_1$ and the required sextupolar strength diverges, $k_{sl} \to \infty$.

The same happens for cases of $\Delta\mu_x = 0$, where $D_2 = -D_1$. Consequently, in all cases bending magnets should be placed between the two sextupoles to modify the value of D_2 and minimize the sextupolar strength.

Table 1.1: Four different sextupole schemes for chromatic correction and aberration compensation, where we have assumed $k_{l1} = k_{l2} = k_l$. Horizontal phase advance, vertical phase advance, transformation matrix between sextupoles, condition for geometric aberration cancellation and condition for chromatic correction are written for each case.

	scheme 1	scheme 2	scheme 3	scheme 4
$(\mu_{x,2} - \mu_{x,1})$ [rad]	π		0	
$(\mu_{y,2} - \mu_{y,1})$ [rad]	π	0	π	0
$M_{1,2}$	$-I_x, -I_y$	$-I_x, I_y$	$I_x, -I_y$	I_x, I_y
geom. canc.	$k_{sl1} = k_{sl2} = k_{sl}$		$k_{sl1} = -k_{sl2} = -k_{sl}$	
chrom. corr.	$k_{sl} = \frac{2k_l}{D_1+D_2}$		$k_{sl} = -\frac{2k_l}{D_1-D_2}$	

For the more general case where the phases advances are $\Delta\mu_x = \pi$, $\Delta\mu_y = \pi$, but $\beta_{x,y;2} \neq \beta_{x,y;1}$, the transformation matrices are not $-I$. From (A.7) they have the more general form

$$M = \begin{pmatrix} -\sqrt{\beta_2/\beta_1} & 0 \\ 0 & -\sqrt{\beta_1/\beta_2} \end{pmatrix}. \tag{1.63}$$

This implies that two sextupoles with the same strength do not cancel the aberrations. Assuming $D_2 = 0$ and using the relations (From (1.63)):

$$x_2' = -\sqrt{\frac{\beta_{x,1}}{\beta_{x,2}}}x_1', \qquad y_2' = -\sqrt{\frac{\beta_{y,1}}{\beta_{y,2}}}y_1'; \tag{1.64}$$

we get the final angle just after sextupole 2 in the horizontal,

$$\begin{aligned} x' &= -\sqrt{\frac{\beta_{x,1}}{\beta_{x,2}}}\left(x_0' + \Delta x_1'\right) + \Delta x_2' \\ &= -\sqrt{\frac{\beta_{x,1}}{\beta_{x,2}}}x_0' - \sqrt{\frac{\beta_{x,1}}{\beta_{x,2}}}\left(\frac{1}{2}k_{sl1}(x_1^2 + D_1^2\delta^2 + 2x_1D_1\delta - y_1^2)\right) + \frac{1}{2}k_{sl2}(x_2^2 - y_2^2); \end{aligned} \tag{1.65}$$

and in the vertical plane,

$$\begin{aligned} y' &= -\sqrt{\frac{\beta_{y,1}}{\beta_{y,2}}}(y_0' + \Delta y_1') + \Delta y_2' \\ &= -\sqrt{\frac{\beta_{y,1}}{\beta_{y,2}}}y_0' - \sqrt{\frac{\beta_{y,1}}{\beta_{y,2}}}\left(k_{sl1}(x_1 + D_1\delta)y_1\right) + k_{sl2}x_2y_2. \end{aligned} \tag{1.66}$$

By substituting the relations

$$x_2 = -\sqrt{\frac{\beta_{x,2}}{\beta_{x,1}}}x_1, \qquad y_2 = -\sqrt{\frac{\beta_{y,2}}{\beta_{y,1}}}y_1; \tag{1.67}$$

we obtain two conditions for the strength of the sextupoles to cancel the geometric aberrations:

$$k_{sl2} = k_{sl1}\left(\frac{\beta_{x,1}}{\beta_{x,2}}\right)^{3/2}, \tag{1.68}$$

$$\frac{\beta_{x,1}}{\beta_{x,2}} = \frac{\beta_{y,1}}{\beta_{y,2}}. \tag{1.69}$$

From these conditions we extract that in addition to a certain relation between the sextupole strengths, the ratio of the betatron functions in the two planes must be the same for the two sextupoles.

Higher Order Aberrations

There are higher order magnetic terms on (1.11) and (1.12) that come either from errors on the magnetic elements or from higher order elements like octupoles (all terms zero except for g_0). They contribute to the geometric aberrations and will have implications for beam stability in circular accelerators.

Properties of the Elements

The elements described have certain properties of symmetry. Their magnetic fields change sign, that is $(B_x, B_y) \to (-B_x, -B_y)$, when the poles are inverted. This implies a sign inversion of the field components (1.13). For electromagnets, the poles are reversed by reversing the powering of the coils, and this is equivalent to the effect of a change in the direction of the beam (or an inversion of the charge of the particle).

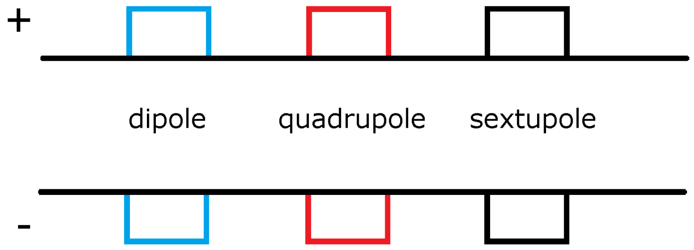

Figure 1.6: Symbols used throughout this thesis to represent the magnetic elements. If the corresponding strength of the element is positive, the element is represented above the line, and for a negative strength below the line.

From (1.4) a change in ($q\boldsymbol{v} \to -q\boldsymbol{v}$) produces the same effect as an inversion of the powering current, that is, an inversion of the Lorentz force. It is also possible to invert the sign of the element by a rotation of $\pi/(n+1)$, with n being the order of the respective element. Therefore, to define the sign of the elements ((1.13) and $B_{y,0}$), the direction and the sign of the charge of the beam particles must be given. In the convention followed here, the elements invert their sign when ($q\boldsymbol{v}$) has the opposite direction to the z-axis (See Fig. 1.1). In this thesis, the elements will be represented as indicated in Fig. 1.6.

1.3 Particle Beams

The particles in a ring follow a specific spatial structure. They are distributed in well defined bunches, as a direct consequence of the RF accelerating system. The beam invariant of the particle ensemble is defined by taking the average of all particle action invariants of the distribution, (1.16, 1.17) $\epsilon_{x,y} = \langle J_{x,y}\rangle_{beam}$. This parameter is called the geometric beam emittance and can also be expressed as

$$\epsilon_x = \sqrt{\langle x^2\rangle\langle x'^2\rangle - \langle xx'\rangle^2}, \qquad \epsilon_y = \sqrt{\langle y^2\rangle\langle y'^2\rangle - \langle yy'\rangle^2}. \tag{1.70}$$

The beam emittance resembles the temperature of the beam. If there is no synchrotron radiation emission (Sec.1.7), the total energy of the particles is constant. If in addition there are no scattering processes present [4], then the emittance is preserved. During particle acceleration, the longitudinal component of the momentum vector, p_z increases while the transverse components remain constant. The angles of the transverse momentum x', y' shrink, and with them the geometric emittance. This process is known as adiabatic damping. A normalized emittance, preserved during the acceleration, is defined as

$$\epsilon_{N;x,y} = \epsilon_{x,y}\gamma_r\beta_r. \tag{1.71}$$

Particle distributions in rings are often approximated by a Gaussian function in all the variables in (1.25). The values of the standard deviation for each of the 5 distributions are denoted as

$$(\sigma_x, \sigma'_x, \sigma_y, \sigma'_y, \sigma_\delta). \tag{1.72}$$

The standard deviation of the $\{x, y\}$ distribution represents the beam size and is given by (see [1, Sec. 8.4.4])

$$\sigma_{x,y}(s) = \sqrt{\epsilon_{x,y}\cdot\beta_{x,y}(s) + D^2_{x,y}(s)\cdot\sigma^2_\delta}. \tag{1.73}$$

In a similar way, the standard deviation in the x', y' is also called beam divergence and is a measure of the spatial growing rate of the beam at longitudinal location s.

$$\sigma'_{x,y}(s) = \sqrt{\epsilon_{x,y}\cdot\gamma_{x,y}(s) + D'^2_{x,y}(s)\cdot\sigma^2_\delta}. \tag{1.74}$$

Both quantities depend on three beam parameters, $\{\epsilon_{x,y},\ \sigma_\delta\}$; and four optical functions, $\{\beta_{x,y}(s),\ D_{x,y}(s)\}$. The distribution in the longitudinal plane can also be considered as Gaussian. The longitudinal beam size is given by the standard deviation in the longitudinal plane, σ_s and depends on the configuration of the RF accelerating system, the ring circumference and the optics.

Aperture

The geometric aperture represents, for a given longitudinal point of the accelerator, the maximum number of σ that the vacuum pipe is able to accommodate. Defined for each plane as $n_{x,y}$, particles with $\sigma_{x,y} \geq n_{x,y}$ will touch the wall.

Intra-Beam Scattering

The Intra-beam scattering (IBS) is a process of momentum transfer between the longitudinal and the two transverse planes, as a consequence of collisions between particles of the same bunch. This leads to a transverse emittance growth causing a beam size increase. This effect depends on different parameters in the beam. In particular, it increases as the number of particles increase and the beam sizes in each phase space dimension decrease: variables in (1.72) and σ_s. More information about this scattering process can be found in [5].

1.4 Particle Colliders

A high center of mass energy (E_{cm}) in the colliding particles is aimed for so as to transform this energy into particles to be studied by high energy physicists. The highest E_{cm} is found with two counter-rotating beams instead of one single beam colliding against a fixed target. The two beams can travel in the same pipe under the influence of the same fields (i.e., for particle-antiparticle colliders), or have separate pipes for each beam.

Collision Scheme

The two beams usually collide with a certain angle in order to avoid parasitic collisions (see 1.6) and restrict the collisions just to the interaction point (IP) (Fig. 1.7). We denote by θ the angle between the two beams. The inner normalized separation is the ratio between the beam separation at a distance Δ_{IP} ($\Delta_{beam,cro}(\Delta_{IP}) = \theta\Delta_{IP}$), and the beam size ($\sigma_{cro}(\Delta_{IP}) \approx \sigma'^{*}_{cro}\Delta_{IP}$). It represents the number of σ in the plane of crossing by which the two beams are separated:

$$\Delta_{in} = \frac{\Delta_{beam,cro}(\Delta_{IP})}{\sigma_{cro}(\Delta_{IP})} = \frac{\theta}{\sigma'^{*}_{cro}} = \Delta_{beam}[\sigma_{cro}]. \tag{1.75}$$

Here the subindex "cro" refers to the plane of crossing. When the two transverse dimensions at the IP of are identical, ($\sigma^*_x = \sigma^*_y$), the beam is said to be round. This is the typical situation for hadron colliders. On the other hand, beams where one dimension is bigger than the other are called flat beams. Usually this is the case for lepton colliders, due to the synchrotron radiation damping that will be addressed in Sec. 1.7.

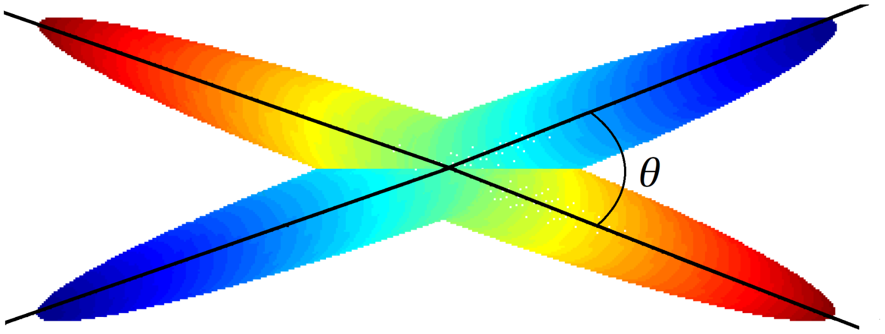

Figure 1.7: Two bunches in collision with a θ crossing angle.

Luminosity

The luminosity is an important parameter to characterize the performance of a particle collider. It is a measure of the ability of the collider to produce a required number of interactions. It represents the density of colliding centers multiplied by the number of particles colliding per unit time. The product of the luminosity L by the cross section of the colliding particle σ_p, gives the event rate as

$$\frac{dR}{dt} = L\sigma_p. \tag{1.76}$$

The units of luminosity are $[\mathrm{T}^{-1}\mathrm{L}^{-2}]$, and are usually expressed in $\mathrm{cm}^{-2}\mathrm{s}^{-1}$ or $\mathrm{b}^{-1}\mathrm{s}^{-1}$. The collision of two Gaussian beams of N_1 and N_2 particles and identical dimensions generates a luminosity of [6]

$$L = \frac{N_1 N_2 f n_b}{4\pi\sigma_x^*\sigma_y^*} S, \tag{1.77}$$

where N_1 and N_2 are the number of particles per bunch in Beam 1 and Beam 2, respectively. n_b is the number of bunches in each beam, f represents the revolution frequency and S is the luminosity reduction factor due to the crossing angle. The variables at the IP are represented with a $\{*\}$ as a superindex, i.e., σ_x^* and σ_y^* represent the beam sizes at the IP. Equation (1.77) is valid for circular colliders, where the same bunches are collided after each turn. In the general case, applicable also to linear colliders, $f n_b$ is substituted by the number of bunches per second. The so-called geometric luminosity reduction factor, S, is given by

$$S = \frac{1}{\sqrt{1+\phi^2}}, \qquad \phi = \frac{\sigma_s}{\sigma_{cro}^*} \cdot \tan\frac{\theta}{2}. \tag{1.78}$$

The variable ϕ is referred as the Piwinski angle. As the crossing angles are usually very small ($\theta \ll 1$ rad), it is approximated as $\phi \approx \theta\sigma_s/(2\sigma_{cro}^*)$.

The expression (1.77) is called instantaneous luminosity. For a linear collider, it depends on the number of particles that are continuously injected. For circular accelerators, the particles are injected once and during collision they are reused. Some particles collide and are lost from the beam (a process called burn-off), so that the luminosity itself decays. Some particle accelerators inject particles at collision energy, to keep the luminosity stable (top-up injection), but the ones that have a different energy and injection and collision do not replace the burnt particles. In that case, considering n_{IP} colliding IPs, the loss rate in the total particle population per beam, $N_T = n_b N_1$, is $\frac{dN_T}{dt} = -n_{IP} L \sigma_p$. Redefining luminosity as $L = AN_T^2$, with $A = fS/(4\pi\sigma_x^*\sigma_y^* n_b)$, the loss rate is expressed as a function of the actual number of particles,

$$\frac{dN_T(t)}{dt} = -n_{IP} A \sigma_p \cdot N_T^2(t), \tag{1.79}$$

whose solution gives the time evolution from the total initial number of particles, $N_{T,0}$; and from that, the luminosity evolution, as follows:

$$N_T(t) = \frac{N_{T,0}}{1+\frac{t}{\tau}} \qquad \text{and} \qquad L(t) = \frac{L_0}{\left(1+\frac{t}{\tau}\right)^2}, \qquad \text{with} \qquad \tau = \frac{N_{T,0}}{L_0 n_{IP} \sigma_p}. \tag{1.80}$$

There may be other processes that lead to a luminosity decay, apart from the burn-off of the colliding particles. In order to study those effects (e.g. IBS, gas scattering), the luminosity in (1.80) can be approximated by an exponential function $L(t) = L_0 e^{-t/\tau_0}$, with a time constant $\tau_0 = (\sqrt{e}-1)\tau$. The total effect of the processes that influence exponentially the luminosity evolution with a time constant τ_i can be studied with the total time constant τ_T, which represents the luminosity lifetime and is given by $\tau_T^{-1} = \tau_0^{-1} + \sum_i \tau_i^{-1}$. The luminosity is then

$$L(t) \approx L_0 e^{-t/\tau_T}. \tag{1.81}$$

By integration of (1.81) over one run $[0, T_r]$, the approximate integrated luminosity is obtained:

$$L_{int}(T_r) = \int_0^{T_r} L(t)\, dt = \tau_T L_0 \left[1 - e^{-T_r/\tau_T}\right]. \tag{1.82}$$

The units of L_{int} are [L^{-2}] and are usually expressed with a power of 1/barn. The integrated luminosity stabilizes after a period. After then, a new beam must be injected to continue with the physics run.

The luminosity gives us the number of events that can be produced, but it should be noted that not all can be detected. During a bunch crossing, there are $L_{SC}\sigma_p$ events, where L_{SC} is the luminosity per single crossing, given by $L_{SC} = L/(f n_b)$. The number of events per bunch crossing is called multiplicity or pile-up. It is limited by the efficiency of the detector to process $L_{SC}\sigma_p$ events that happen almost instantaneously. A too large value of L_{SC} may lead to some events not being detected.

Final-Focus Systems

To get a large number of events, the luminosity must be maximized. Then, according to (1.77) the beam size at the interaction point must be as small as possible. For this purpose, a series of elements is placed in the region close to the IP, in order to reduce β at the IP, denoted as β^*. At the IP usually $D_{x,y} = 0$ and $\alpha_{x,y} = 0$, so that beam size (1.73) and beam divergence (1.74) are written as

$$\sigma^*_{x,y} = \sqrt{\epsilon_{x,y}\beta^*_{x,y}}, \qquad \sigma'^*_{x,y} = \sqrt{\frac{\epsilon_{x,y}}{\beta^*_{x,y}} + (D'^*_{x,y}\sigma_\delta)^2}. \tag{1.83}$$

The smaller the beam size at the IP, the bigger the beam divergence (1.73). In other words, a direct consequence of shrinking $\sigma^*_{x,y}$ is the growth of the beam size in the final-focus elements. The aperture of those elements must be sufficiently large to accommodate the wide beam. The chromatic effects affect the effectiveness of the final-focus systems to reduce the beam size at the IP. If it is not corrected, it causes a relative beam size dilution [7] of

$$\frac{\sigma^*_{x,y}(\sigma_\delta) - \sigma^*_{x,y}(\sigma_\delta = 0)}{\sigma^*_{x,y}(\sigma_\delta = 0)} \sim \frac{L^*\sigma_\delta}{\beta^*_{x,y}}, \tag{1.84}$$

where L^* is the distance between the first quadrupole and the IP, the so-called free length. The relative beam size growth given in (1.84) takes into account the chromatic effect of the final quadrupole only, and not the one of all the other quadrupoles prior to the final element. Thus, it can be used as a rough estimator that gives an indication of the minimum beam size if the chromaticity is not corrected.

Hourglass Effect

It is assumed in (1.77) that the beam sizes are constant over the whole collision region. This is not always a good approximation, particularly for low-β insertions. In fact, the β-function in a drift space varies quadratically with the distance to the minimum. As the β-function has the minimum value at the IP, the relation is

$$\beta_{x,y}(s) = \beta^*_{x,y} + \frac{s^2}{\beta^*_{x,y}}, \tag{1.85}$$

so that the beam size varies too. Substituting (1.85) in (1.83) we obtain how the beam sizes grow near the IP.

$$\sigma_{x,y}(s) = \sigma^*_{x,y}\sqrt{1 + \frac{s^2}{{\beta^*_{x,y}}^2}}. \tag{1.86}$$

Figure 1.7 represents a bunch collision where the beams are simplified by their cross section on the plane of crossing and on the longitudinal one. They are also simplified by the parallelogram that has the 1-σ inscribed.

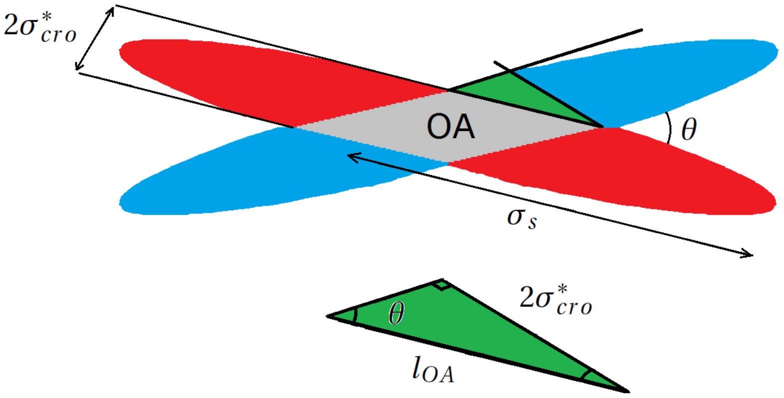

Figure 1.8: Simplified scheme of the bunches in collision, showing the overlapping area as the intersection between the beams represented as a (σ_x, σ_s) ellipse (top). Geometrical deduction of (1.87) (bottom).

The effect of enlargement of the beam size described in (1.86) is larger as β^* gets smaller and becomes important when is equal to or smaller than the length of the overlapping area between the beams, a value that is given by

$$l_{OA} = \frac{2\sigma^*_{cro}}{tg\theta} \approx \frac{2\sigma^*_{cro}}{\theta}. \tag{1.87}$$

This quantity is related to the rms width of the luminous region (defined from the convolution of the two colliding bunches at the IP), which is given by

$$\frac{1}{\sigma_l^2} = \frac{2}{\sigma_s^2} + \frac{\theta^2}{2\sigma^{*2}_{cro}}. \tag{1.88}$$

and their limits for head-on collisions and for long bunch lengths are given, respectively, by

$$\lim_{\theta\to 0} \sigma_l = \frac{\sigma_s}{\sqrt{2}}, \qquad \lim_{\sigma_s\to\infty} \sigma_l = \frac{\sqrt{2}\sigma^*_{cro}}{\theta}. \tag{1.89}$$

The luminous region and the length of the overlapping are related as $l_{OA} = \sqrt{2}\sigma_l$. Figure 1.8 illustrates the geometric relations (1.87, 1.89). This is an important limitation in LHC. As the bunch length is $\sigma_s = 7.5$ cm, the $\beta^*_{x,y}$ must not be smaller than that value to avoid an important luminosity reduction, $\beta^*_{x,y} \geq 7.5$ cm.

The hourglass effect causes a diminution in the luminosity (see [6]), since not all particles collide at the minimum of the β-function,

$$L = \frac{N_1 N_2 f n_b}{4\pi\sigma^*_x\sigma^*_y}\frac{\cos(\frac{\theta}{2})}{\sqrt{\pi}\sigma_s}\int_{-\infty}^{\infty}\frac{\beta^{*2}e^{-s^2C}}{\beta^{*2}+s^2}\,ds, \tag{1.90}$$

with

$$C = \frac{\beta^{*2} \sin^2 \frac{\theta}{2}}{\sigma_x^{*2} \left(\beta^{*2} + s^2\right)} + \frac{\cos^2 \frac{\theta}{2}}{\sigma_s^2}. \tag{1.91}$$

1.5 Circular Accelerators

When this kind of accelerator is used as a particle collider, it reuses the non-colliding particles to have a higher luminosity. The fact that the particles recirculate and pass by the same elements in the order of thousands of times per second introduces some particularities. It should also be noted that circular accelerators may be used to produce radiation (Sec. 1.7).

Resonance Diagram

The imperfections of the machine cause certain values of the tunes to excite resonances. The resonance plot allows exploring the range of tunes available for the machine operation. Figure 1.9 shows an example of a resonance diagram, whose lines are given by the following expression, where a, b and i are integers [1, Sec. 13.1.3]:

$$a\upsilon_x + b\upsilon_y = i. \tag{1.92}$$

The order of the resonance is $|a| + |b|$. υ_x and υ_y represent the fractional part of the particle tunes, Q_x and Q_y, respectively. The tune of the machine must be chosen so that it is located far enough from any resonance.

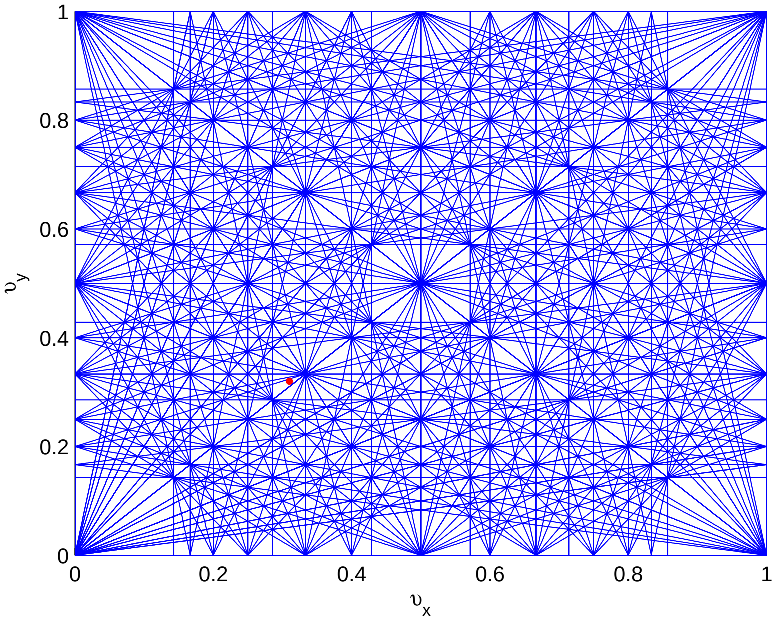

Figure 1.9: Resonance diagram of order 7. The nominal tune of the particles is represented by a point (in red, that of the LHC), and must be sufficiently far from the resonance lines.

Chromaticity

The difference in momentum of the particles in a beam, causes the trajectories to not all follow the design values. This produces a beam size dilution, as it was addressed in Sec. 1.4 (1.84). There is another important effect, namely the difference in the transverse oscillation frequency. Off-momentum particles have different tunes. The point-like working point in the resonance diagram for the ideal case of a monochromatic beam turns into a surface and this makes it more difficult to keep particles between the resonance lines and not to excite any resonances. Second, in the case of bunched beams, a nonzero chromaticity can give rise to a transverse instability called "head-tail effect" (see [9]). The wake field generated by the leading part of a bunch excites an oscillation of the trailing part of the same bunch. In half a synchrotron period the head and the tail of the bunch interchange their positions and the oscillation can be anti-damped and then lead to a beam loss. The growth rate of this instability is much faster for negative than for positive chromaticity values and vanishes for zero chromaticity.

The tune for a particle with momentum deviation δ is modified from the nominal value $Q^0_{x,y}$ as follows:

$$Q_{x,y}(\delta) = Q^0_{x,y} + Q'_{x,y}\delta + \frac{1}{2}Q''_{x,y}\delta^2 + \frac{1}{3!}Q'''_{x,y}\delta^3 + ..., \tag{1.93}$$

The linear chromaticity is the term $Q'_{x,y}$. It can be computed in each plane as:

$$Q'_x = -\frac{1}{4\pi}\oint \beta_x(s)\cdot[k(s) - k_s(s)\cdot D_x(s)]\, ds, \tag{1.94}$$

$$Q'_y = \frac{1}{4\pi}\oint \beta_y(s)\cdot[k(s) - k_s(s)\cdot D_x(s)]\, ds. \tag{1.95}$$

The closed path integral is taken along all the ring and it can be approximated as a sum over the quadrupoles and the sextupoles. It is assumed that there is no vertical dispersion. See [1, Sec. 12.2.1]. $Q''_{x,y}$, $Q'''_{x,y}$,... are called second, third,... order chromaticities. As it is not possible to maintain exactly zero chromaticity, due to some errors, it is usual to adjust to small positive values next to zero. Then, it is assured that the chromaticity will not lead to negative values, where the growth rate of the "head-tail" instability is shorter.

Chromatic Beta Beat

The chromatic tune shift of the off-momentum particles commented in Sec. 1.5 is a global effect. Chromatic effects also affect the β-function along all the ring, by varying their value from $\beta_{x,y}(s)$ to $\beta_{x,y}(s) + \Delta\beta_{x,y}(s,\delta)$. This effect is called chromatic β-beat [1, Sec. 14.2.3]), and is given in first order and in the horizontal plane by

$$\frac{\Delta\beta_x(s,\delta)}{\beta_x(s)} = \frac{\delta}{2\sin(2\pi Q^0_x)}\oint \beta_x(\tau)\cdot[k(\tau) - k_s(\tau)\cdot D_x(\tau)]\cdot\cos\left[2Q^0_x(\mu_x(s) - \mu_x(\tau) + 2\pi)\right] d\tau, \tag{1.96}$$

and in the vertical plane by

$$\frac{\Delta\beta_y(s,\delta)}{\beta_y(s)} = \frac{-\delta}{2\,\sin(2\pi Q_y^0)} \oint \beta_y(\tau)\cdot[k(\tau)-k_s(\tau)\cdot D_x(\tau)]\cdot\cos\left[2Q_y^0(\mu_y(s)-\mu_y(\tau)+2\pi)\right]d\tau. \tag{1.97}$$

This effect must be taken into account because it increases the beam size and limits the aperture.

Dynamic Aperture

In an accelerator there are particles that perform stable motion and others whose behaviour is chaotic and which eventually may be lost. However the distinction between the two cases is not clear and most particles exhibit a pseudochaotic motion. It happens that after a certain number of turns, particles with $\sigma_{x,y} < n_{x,y}$ may be lost from the machine. The dynamic aperture (DA) represents the radius expressed as number of σ within which stable motion is guaranteed for a given number of turns (n_{DA}(turns)). For elliptical beams, the radius is defined as $n = \sqrt{n_x^2 + n_y^2}$.

1.6 Beam-Beam Effects

During a bunch crossing, there is only a small fraction of particles that collide. Most particles do not experience any collision against particles of the other beam, but their dynamics is nevertheless highly distorted by the macroscopic electromagnetic field produced by the opposing beam. That field produces a kick on each passing particle that for round beams is of the form (see [10]).

$$\Delta\{x', y'\} = \pm\frac{2N_1 r_p}{\gamma_r}\frac{\{x,y\}}{r^2}\left[1-\exp\left(-\frac{r^2}{2\sigma^{*2}}\right)\right], \tag{1.98}$$

where $r = \sqrt{x^2+y^2}$, r_p is the classical particle radius, $r_p = \frac{1}{4\pi\epsilon_0}\frac{e^2}{m_0c^2}$, and σ^* the beam size in the two planes, that is assumed to be equal, $\sigma^* \equiv \sigma_x^* = \sigma_y^*$. The sign is positive when the two beams have the same sign charge (case of LHC) and negative if the charge is different, as for example in an electron-positron (e^-e^+) collider or in the LHeC [11]. For small amplitudes the kick is linear and proportional to the amplitude. Its effect is in fact similar to that of a quadrupole and it creates a tune shift, denoted as ΔQ_{ho} ('ho' for head-on, to differentiate it from the long-range tune shift). That focusing (or defocusing, depending on the sign) effect for small amplitude particles is given by the following expression, that is valid for non-round beams,

$$\Delta\{x', y'\} = \frac{4\pi\xi_{x,y}}{\beta_{x,y}^*}\{x,y\}, \tag{1.99}$$

where $\xi_{x,y}$ is the beam-beam strength parameter,

$$\xi_{x,y} = \frac{N r_p \beta^*_{x,y}}{2\pi\gamma_r \sigma^*_{x,y}(\sigma^*_x + \sigma^*_y)}. \tag{1.100}$$

The expressions (1.99) and (1.100) apply for head-on collisions. For small tune shift values and nominal betatron tunes, $\xi_{x,y}$ is roughly equal to the beam-beam tune shift, $\xi_{x,y} \approx \Delta Q_{bb}$. That effect must be carefully taken into account when deciding the bunch intensity. According to (1.77), setting $N = N_1 = N_2$ as the number of particles per bunch, the luminosity scales as $L \propto N^2$. The maximum attainable tune shift limits the number of particles and consequently the peak luminosity. For collisions with a finite crossing angle we substitute $\sigma^*_{cro} \to \sigma^*_{cro}\sqrt{1+\phi^2}$ in (1.100). For unequal beam sizes [12], the tune shifts become

$$\xi_x = \frac{r_p}{2\pi\gamma_r} \frac{N\beta^*_x}{\sigma^*_x\sqrt{1+\phi^2}\left(\sigma^*_y + \sigma^*_x\sqrt{1+\phi^2}\right)}, \tag{1.101}$$

$$\xi_y = \frac{r_p}{2\pi\gamma_r} \frac{N\beta^*_y}{\sigma^*_y(\sigma^*_y + \sigma^*_x\sqrt{1+\phi^2})}. \tag{1.102}$$

For the specific case of $\sigma^*_x \gg \sigma^*_y$ (flat beams), these expressions simplify to

$$\xi_x = \frac{r_p}{2\pi\gamma_r} \frac{N}{\epsilon_x(1+\phi^2)}, \tag{1.103}$$

$$\xi_y = \frac{r_p}{2\pi\gamma_r} \frac{N\beta^*_y}{\sigma^*_x\sigma^*_y\sqrt{1+\phi^2}}. \tag{1.104}$$

The luminosity (1.77) can be expressed as a function of the vertical beam-beam strength for flat beams, namely

$$L = \frac{f n_b \gamma_r N}{2 r_p \beta^*_y} \xi_y. \tag{1.105}$$

For round beams and two IPs contributing to the tune shift and crossing in different planes, the total beam-beam tune shift is the same in the two planes and equal to the sum of the vertical and the horizontal tune shifts:

$$\xi_T = \xi_x + \xi_y = \frac{N r_p}{2\pi\epsilon_N\sqrt{1+\phi^2}}. \tag{1.106}$$

This result is consistent with [13], where other approximations were made. In a similar way as for flat beams, the luminosity for round beams can be expressed as a function of the total beam-beam tune shift. Combining (1.77) and (1.106), we get

$$L = \frac{f n_b \gamma_r N}{2 r_p \beta^*} \xi_T. \tag{1.107}$$

Beam-Beam Limit

For lepton colliders, the beam-beam parameter is linearly proportional to the bunch intensity but above a certain limit, ξ_{limit}, it saturates due to an increase in the vertical beam size proportional to the intensity. As a consequence, above the beam-beam limit the luminosity scales linearly instead of quadratically. This effect comes from coupling between the transverse planes, synchrotron radiation and other effects that the equilibrium between long-range interactions and the damping determines ξ_{limit}. In hadron colliders, the beam-beam limit appears in the form of a poor lifetime, significant emittance growth or coherent beam-beam instabilities. The experience with past hadron collider machines indicated that this limit can be found for total tune shift (sum of all IPs) above 0.015. However, more recent studies have estimated this limit to be in a larger value of $\xi_{x,y}$ [14]. In fact, tune shifts above 0.02 have been achieved during Tevatron run II [15].

Long-Range Interactions

In some particle colliders the beams interact with each other also out of the nominal interaction point. This happens for colliders with a single aperture, as LEP [16]. But even for colliders with separated apertures for each beam in the bending dipoles, the beams pass next to each other at least in the region between the first element and the IP.

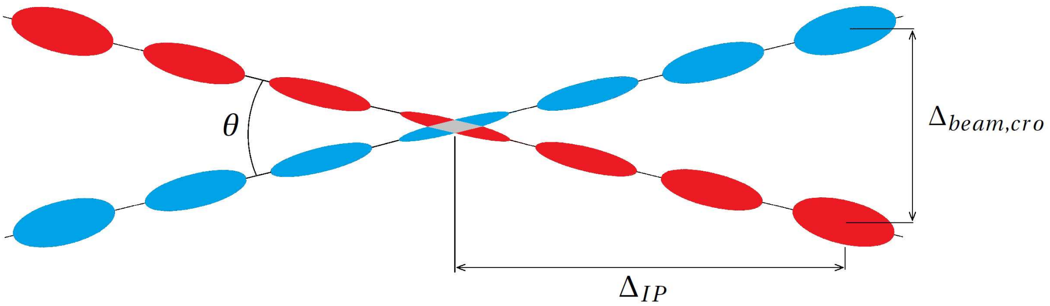

Figure 1.10: Two bunched beams colliding with a crossing angle. Bunches do not experience head-on collisions at a distance Δ_{IP} from the IP. But there is a magnetic interaction with the bunch of the other beam which is separated by a distance $\Delta_{beam,cro}$.

Those interactions between bunches of the two beams at certain distances from the interaction point, Δ_{IP} (See Fig. 1.10), they produce a tune shift, ΔQ_{lr}. This tune shift is inversely proportional to the inner normalized separation (1.75), $\Delta Q_{lr} \propto 1/\Delta_{in}$. In order to control the long-range interactions, the inner normalized separation must be kept. That means increasing θ while decreasing β^* in the plane of crossing as

$$\theta = \Delta_{in}\sqrt{\frac{\epsilon_{cro}}{\beta^*_{cro}}}, \tag{1.108}$$

where (1.74) has been used, with $\alpha^*_{cro} = 0$, $D'^*_{cro} = 0$. Those long-range interactions also depend on the bunch population [17].

1.7 Synchrotron Radiation

When a charged particle is accelerated it emits electromagnetic radiation. This is the base principle of synchrotron light sources which produce radiation with certain properties as high brightness or high coherence, and serve for research in another fields of science. The emission of synchrotron radiation (SR) causes basically two effects:

- Incidence of photons on the vacuum pipe walls.
- Energy loss in the circulating particles due to the recoil when the photon is emitted.

A particle with electric charge e, rest mass m_0 and energy E, following a trajectory with curvature radius ρ emits electromagnetic energy with a power [18]

$$P = \frac{e^2 c}{6\pi\epsilon_0 \rho^2}\left(\frac{E}{m_0 c^2}\right)^4 . \tag{1.109}$$

This means that for two different accelerators with the same bending radius and the same total energy, but one of them carrying electrons and the other protons; the emitted power for the electrons is $(m_p/m_e)^4 (\approx 1.13\cdot 10^{13})$ times that of protons. The large amount of SR emitted for leptons of high energy has led to think of the next e^+e^- either as a linear collider (no bending magnets, no SR radiation), like CLIC [19] and ILC [20]; or as a circular collider with a huge radius, such as LEP3 [21] or TLEP [22]. On the other hand, the light emitted can damage the walls. The photons interact with the atomic nuclei on the wall and may also extract some electrons. The build-up of electron density in the vacuum chamber is called the electron cloud, being a source of scattering. See example [23].

There are two effects that play a significant role in this thesis: the synchrotron radiation damping, that causes a damping in the transverse motion, decreasing the emittance; and the emittance blow up.

Synchrotron Radiation Damping

One of the effects of the synchrotron radiation in circular colliders is the presence of a damping in the transverse momentum. The reason is that the emitted photons cause a loss in energy. This is a loss in the module of the momentum, while the angle remains constant. When the particles pass through the RF cavities, the longitudinal component of the momentum is restored, but the transverse one is not affected, decreasing the angle of the particles. Consequently, emittance shrinks and with it the beam size.

$$\epsilon_x(t) = \epsilon_{0,x} e^{-t/\tau_x}; \qquad \epsilon_y(t) = \epsilon_{0,y} e^{-t/\tau_y}; \qquad \epsilon_s(t) = \epsilon_{0,s} e^{-t/\tau_s}. \tag{1.110}$$

The parameters τ_x, τ_y and τ_s determine this process and are called damping times.

Emittance Blow Up due to Quantum Excitation

This effect has an opposite effect on beam size than the synchrotron radiation damping. Namely it causes an enlargement of the beam size. For a linear collider, the dilution of the horizontal IP beam size due to synchrotron radiation emitted in the bending magnets can be estimated from [24] as

$$\Delta(\sigma_x^{*2})/\beta_x^* \approx \Delta\left(\sigma_x^{*2}/\beta_x^*\right) = \Delta\epsilon_x = 4.13\times 10^{-11}\mathrm{m}^2\mathrm{GeV}^{-5}E^5\mathscr{I}, \tag{1.111}$$

where E represents the total beam energy and $\mathscr{I}$ is given by

$$\mathscr{I} = \int_0^L \frac{\mathscr{H}(s)}{|\rho_x(s)^3|}\cos^2\Phi(s)\;ds, \tag{1.112}$$

and where the variables $\mathscr{H}$ and Φ are defined as

$$\mathscr{H}(s) = \frac{D_x^2(s) + [D_x'(s)\cdot\beta_x(s) + D_x(s)\cdot\alpha_x(s)]^2}{\beta_x(s)}, \tag{1.113}$$

$$\Phi(s) = \Delta\mu_x(L) - \Delta\mu_x(s) + \arctan\left(-\alpha_x(s) - \beta_x(s)\frac{D_x'(s)}{D_x(s)}\right). \tag{1.114}$$

A minimization of $(\mathscr{H}(s)\cdot\cos^2\Phi(s))$ at the location of the bending magnets $(\rho_x(s)\neq\infty)$ must be done in order to reduce the beam size enlargement coming from the synchrotron radiation.

2. LHC Optics and Upgrades

The first years of LHC beam operation at 3.5 TeV (March 2010–April 2012) and 4 TeV (April 2012–December 2012) have been a success. The machine will reach the design value of 7 TeV after the first long shutdown (LS1) and will run at the nominal or higher luminosity from 2015 to the end of 2022, including a second long shutdown (LS2) from 2018 to 2019. Beyond this horizon and to continue with the physics studies, new upgrades will be necessary. Two of the possible upgrades studied in this thesis enhance some parameters of the proton-proton collisions (HL-LHC and HE-LHC) and another one will enable electron-proton collisions (LHeC). This chapter reviews the optics of the LHC high luminosity regions, its chromatic correction, and summarizes the main upgrade plans.

2.1 The Large Hadron Collider

The LHC is a pp (proton-proton) collider. It can also be configured to accelerate and collide $^{208}\mathrm{Pb}^{82+}$ ions, but this mode of operation will not be considered here. Figure 2.1 shows a schematic layout of the ring, made of three kinds of sections: arcs, long straight sections (LSS) and dispersion suppressors (DS). The 8 arc sections occupy most of the ring circumference and their aim is just to close the ring, so that the particles that were not spent in the collisions can be reused. The LSS accommodate the Interaction Regions (IRs). More precisely, there are 8 IRs in total, four of which provide collisions and are devoted to High Energy Physics studies. The other four IR host the longitudinal momentum cleaning (IR3), the radio frequency cavities for beam acceleration (IR4), the beam dump system (IR6) and the betatron momentum cleaning (IR6). Finally, the 16 DSs make the dispersion zero for the LSS, and they are interleaved between the arcs and the LSSs. They have less average curvature radius than the arcs due to the lower density of bending magnets.

The four main physics experiments are installed in IR1, IR2, IR5 and IR8. In these points the reference orbits of the two beams intersect and change side. Big detectors track, record and analyze the fragments of the collisions. In particular, the experiments installed in IR1 (ATLAS [25]) and IR5 (CMS [26]), are called high luminosity experiments since the design luminosity has a much higher value here than in the other two experiments. Both of them have confirmed the discovery of a new particle compatible with a standard model Higgs boson, in July 2012 [27].

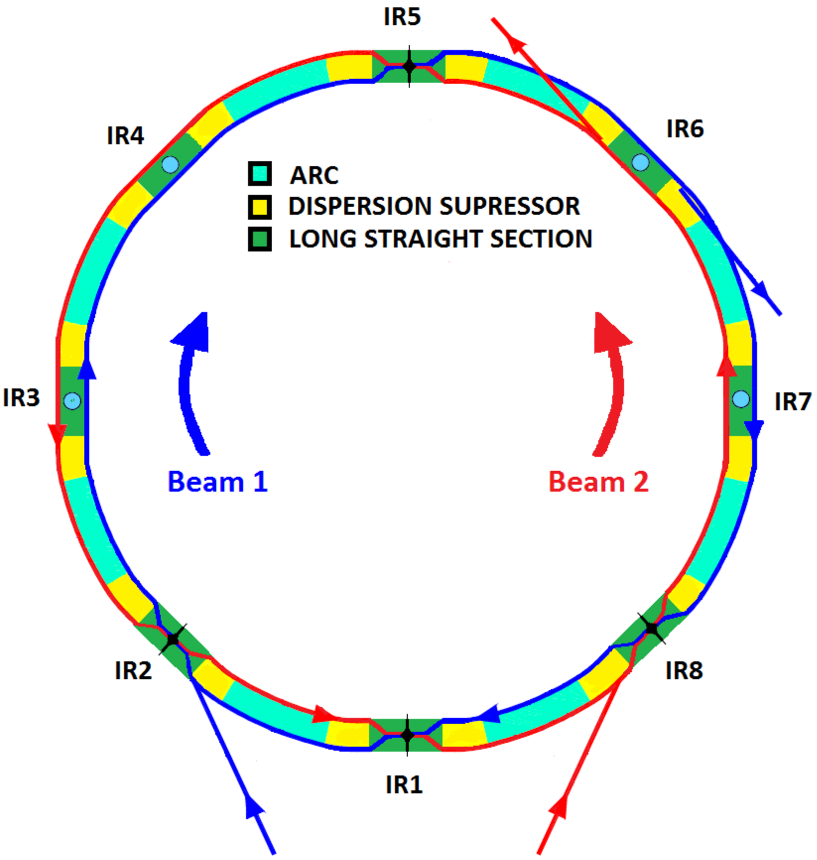

Figure 2.1: LHC schematic layout, showing the LSSs, the DSs and the arcs. The two transfer lines for particle injection are also shown, as well as the beam dump lines, that take each beam out of the ring to safely absorb its energy in case of malfunction. The total length of the machine is 26.7 km.

2.2 High Luminosity Insertions

Table 2.1 shows some parameters of the IR quadrupoles and separation magnets on each side of the IP, with ascending numeration as we proceed from the IP. Each kind of magnet is described in [28, Ch. 8]. Magnets Q1–Q3 have a common aperture for the two beams while the other quadrupole magnets have a separated one. The separation is done by two bending magnets (D1 and D2) per side. They modify the horizontal separation between the beams from 194 mm in the arcs to 0 mm. In IP1 and IP5 high radiation levels from the collision debris are expected that may raise the temperature of the magnet. That is why D1 is a warm (normal conducting) magnet. In IR2 (ALICE) and IR8 (LHCb), with lower design luminosity, D1 has been made as a superconducting magnet. In all cases, the D2 separation dipole is built as a twin-aperture superconducting magnet.

Table 2.1: Parameters of the LHC magnets for the high luminosity insertions. Section, name, type, magnetic length, aperture coil and nominal value of the magnetic field (dipole component for bending magnets and gradient for quadrupoles). The aperture represents the radius of the coil circle except for MBXW (*), that has a rectangular aperture and it represents the gap height.

section	element	type	L [m]	ap [mm]	nominal value
Final Triplet	Q1	MQXA	6.37	35	200–205 T/m
	Q2	MQXBx2	5.5x2		
	Q3	MQXA	6.37		
Matching Section	Q4	MQY	3.4	35	160 T/m
	Q5	MQML	4.8	28	
	Q6	MQML	4.8	28	
	Q7	MQMx2	3.4x2	28	200 T/m
Separation Magnets	D1	MBXWx6	3.4x6	63*	1.28 T
	D2	MBRC	9.45	40	3.8 T
Dispersion Suppressor	Q8	MQML	4.8	28	200 T/m
	Q9	MQM	3.4		
	Q10	MQML	4.8		
Dispersion Suppressor Extension	QT11	MQTL	1.30	28	110 T/m
	QT12	MQT	0.32		
	QT13	MQT	0.32		

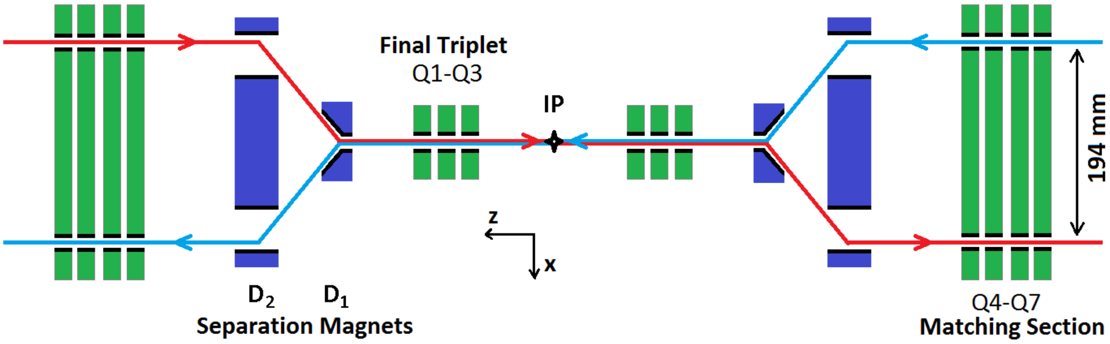

Figure 2.2: LHC separation scheme in the IRs, showing the reference orbits of the two beams (not to scale). They are merged through the dipole separator magnets: D1 and D2. The triplet magnets host the two beams in the same beam pipe, while the matching section (MS) magnets have separate pipes for the two beams.

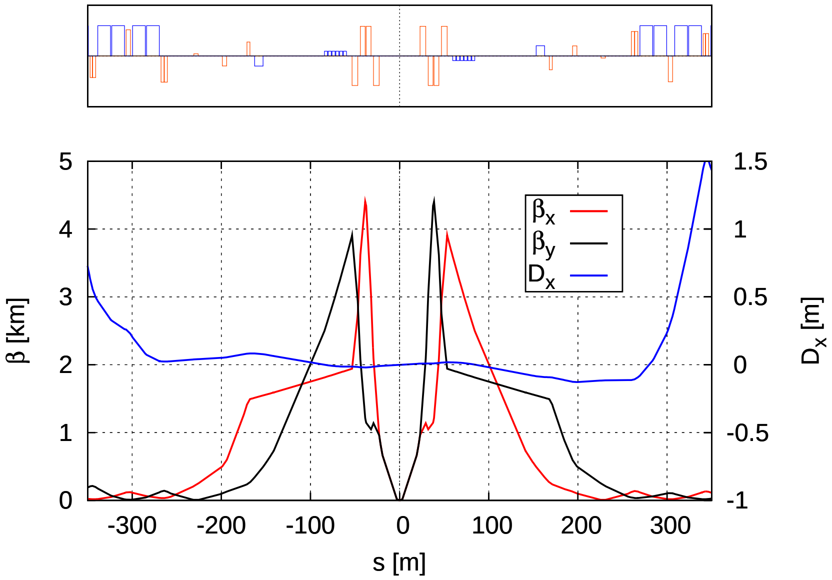

Figure 2.3: LHC IR1 & IR5 optics for Beam 1, with $\beta^*_{x,y} = 0.55$ m. The optics is antisymmetric left-/right, fulfilling (2.8) and (2.9).

Figure 2.2 sketches the separation scheme. The closed reference orbits of the two beams are coincident between D1 and the IP. Orbit bump correctors modify the closed orbits to restrict the collisions just to the IP, by making them collide with an angle.

This beam crossing is in the vertical plane in IP1 and the horizontal one in IP5, in order to cancel the so-called pacman effect [29]. Due to the inhomogeneity of the bunch distribution in a beam, there are some bunches that experience a small number of long-range interactions, and thus different ΔQ_{lr}. This is compensated by the alternating crossing angle.

One of the main studies of this thesis is focused on the IR upgrade of the two high luminosity experiments, in order to provide them with a high event rate. Their actual optics is shown in Fig. 2.3 (Beam 1) and Fig. 2.4 (Beam 2). The optics is represented in two plots. The top one represents the strength of dipoles, quadrupoles and sextupoles, using the symbols in Fig. 1.6. The vertical size is proportional to the relative strength. Consequently, the relative relation between the areas gives the relation between integrated strengths. The bottom plots represents β_x, β_y and D_x. As the convention for directions refers to an observer standing inside the ring and looking out, negative values of s represent the left side of the IR and positive values represent the right side.

2.2.1 An Antisymmetric IR

For the following, we will consider $\beta^{1*}_{x,y} = \beta^{2*}_{x,y}$ and $\alpha^{1*}_{x,y} = \alpha^{2*}_{x,y} = 0$. We have called here “symmetric Beam 1/Beam 2” an optics that fulfills the condition $k^1(s) = k^2(s)$, where $s = 0$

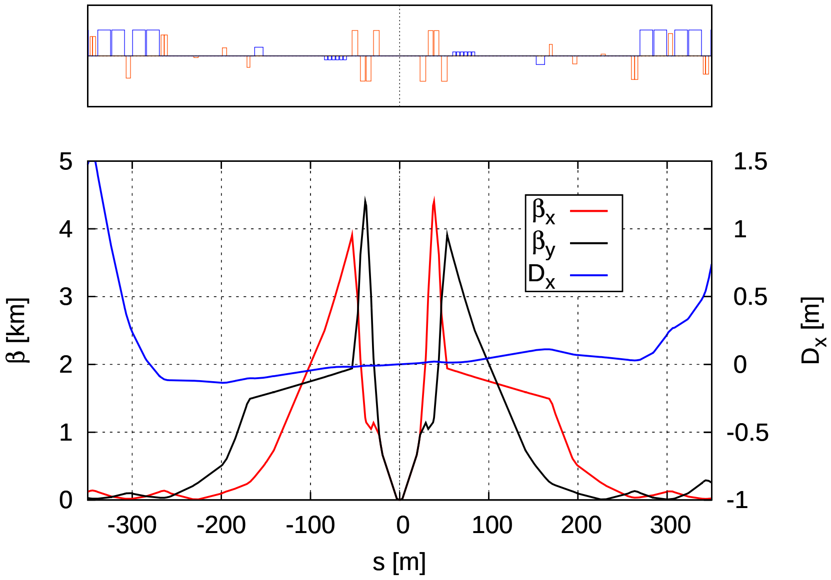

Figure 2.4: LHC IR1 & IR5 optics for Beam 2, with $\beta^*_{x,y} = 0.55$ m. By comparing with Fig. 2.3 we see that the LHC optics is antisymmetric Beam 1/ Beam 2, fulfilling (2.6) and (2.7).

represents the position of the IP and the superindex refers to the beam:

$$\beta^1_x(s) = \beta^2_x(s);\ \alpha^1_x(s) = \alpha^2_x(s), \tag{2.1}$$

$$\beta^1_y(s) = \beta^2_y(s);\ \alpha^1_y(s) = \alpha^2_y(s). \tag{2.2}$$

We denote by "symmetric left/right" to an optics that is characterized by the same parameters of the normalized quadrupole focusing strength, k, at both sides of the IP. This condition is expressed as $k(s) = k(-s)$ for both beams. For the general case $\beta^*_x \neq \beta^*_y$, such optics exhibits the following properties:

$$\beta_x(s) = \beta_x(-s);\ \alpha_x(s) = -\alpha_x(-s), \tag{2.3}$$

$$\beta_y(s) = \beta_y(-s);\ \alpha_y(s) = -\alpha_y(-s). \tag{2.4}$$

In the particular case of round beams, $\beta^*_x = \beta^*_y$, there is an additional relation, to be added to (2.3) and (2.4),

$$\beta_x(s) = \beta_y(s), \alpha_x(s) = \alpha_y(s). \tag{2.5}$$

In the LHC the two beams share the same vacuum pipe in the final-focus system, that consists of three quadrupoles: Q1, Q2 and Q3. This triplet focuses the beam bringing down the β-function at the IP. The two beams are influenced by the same magnetic field distribution, but due to the opposite direction of movement, the focusing effect is the opposite for the two beams. This is represented by magnetic field strengths of opposite sign, $k^1(s) = -k^2(s)$, as

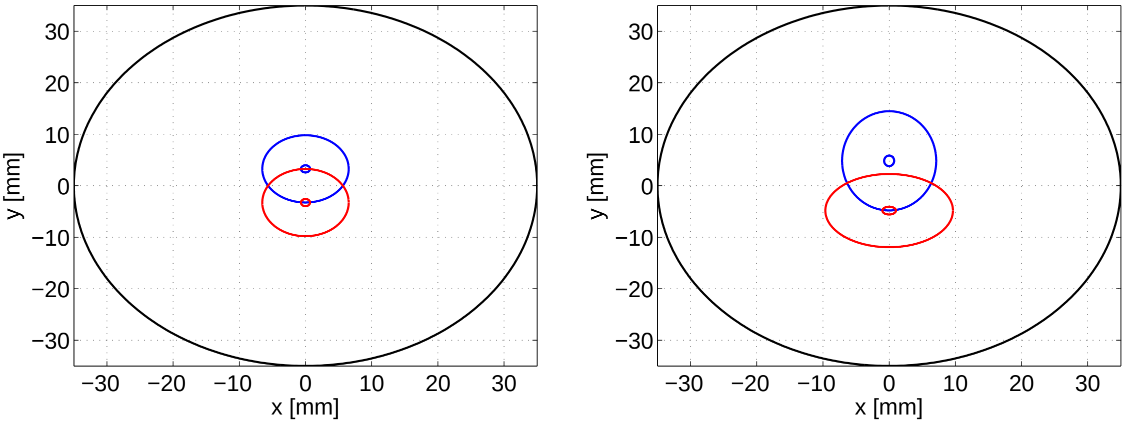

Figure 2.5: Beams at the entrance of Q1, at $s = 23.0$ m (left) and at the exit, at $s = 29.4$ m (right) for IP1 and Beam 1. The black circumference represents the inner coil aperture. Q1 focalizes Beam 1 in the horizontal plane and Beam 2 in the vertical.

explained in Sec. 1.2. We call this “antisymmetric Beam 1/Beam 2” optics. Instead of relations (2.1) and (2.2) and if we assume $\beta_x^* = \beta_y^*$ (round beams) the following conditions apply:

$$\beta_x^1(s) = \beta_y^2(s);\ \alpha_x^1(s) = \alpha_y^2(s), \tag{2.6}$$

$$\beta_y^1(s) = \beta_x^2(s);\ \alpha_y^1(s) = \alpha_x^2(s). \tag{2.7}$$

In order to make the optics of the two beams equivalent, the triplet magnets feature $k(s) = -k(-s)$. This optics is labelled “antisymmetric left/right”. Then, instead of (2.3) and (2.4), the following relations between the two beams hold:

$$\beta_x(s) = \beta_y(-s);\ \alpha_x(s) = -\alpha_y(-s), \tag{2.8}$$

$$\beta_y(s) = \beta_x(-s);\ \alpha_y(s) = -\alpha_x(-s). \tag{2.9}$$

Relations (2.6), (2.7), (2.8) and (2.9) define the LHC optics as “antisymmetric left/right” and “antisymmetric Beam 1/Beam 2”. A study of a “symmetric left/right” IR optics was also done in the past [30]. However an antisymmetric layout was finally preferred [31].

Figure 2.5 shows the beams just before and after the Q1. The colours that represent the beams follow the usual code for the LHC already used in Fig. 2.1. The inner ellipses have a dimension of (σ_x, σ_y) while the outer ones have $(9.5\sigma_x, 9.5\sigma_y)$.

2.2.2 Arc Optics

Each of the 8 arc sections is composed of 32 identical FODO (focusing-defocusing) cells of 106.9 m length. Each FODO cell, features two quadrupoles of opposite sign. The spaces between the quadrupoles are filled with 3 bending magnets each. The equivalent quadrupoles of the two rings are powered at the same field gradient, establishing an antisymmetric optics.

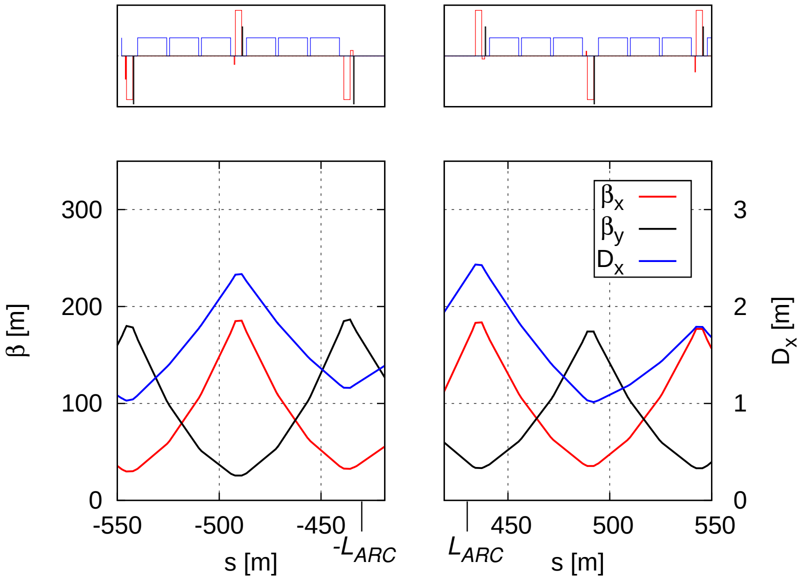

Figure 2.6: First arc cell on either side of IP1 in LHC for Beam 1. L_{ARC} represents the distance between the IP and the beginning of the arc (L_{ARC} = 434 m).

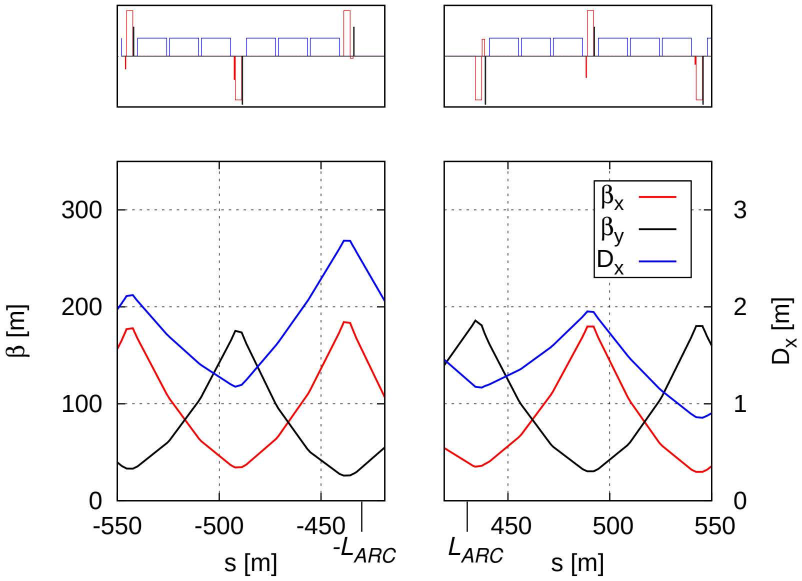

Figure 2.7: First arc cell on either side of IP1 in LHC for Beam 2.

This was designed to match the antisymmetry of the IRs. In general, one should also consider the weak focusing from the bending magnets, that renders the antisymmetric properties only an approximation. In order to be exact, '∼' should replace '=' in (2.6), (2.7), (2.8) and (2.9). However the approximation is good because in the LHC the weak focusing term is negligible compared with the effect of the strong quadrupoles. Figure 2.6 illustrates the antisymmetric properties of the arc optics for Beam 1 and Fig. 2.7 for Beam 2.

A dispersion suppressor is located at both sides of each straight section that aims at a reduction of the machine dispersion in the insertions. Each LHC dispersion suppressor contains four individually powered quadrupole magnets (Q8, Q9, Q10, Q11) which are separated by two dipole magnets. This is equivalent to two FODO cells with two dipole magnets between quadrupoles instead of three (the missing dipole scheme [32]). In order to reduce the dispersion at the IPs to zero, three more quadrupoles must be also individually powered (QT11, QT12, QT13). In terms of the machine optics the dispersion suppressor is made of the two missing dipole cells plus one additional arc cell. Figure 2.8 shows the structure of the LHC dispersion suppressor. As the dispersion is zero between the DS and the IP, the MS quadrupoles have to match a set of 4 variables ($\beta_x, \beta_y, \alpha_x, \alpha_y$) instead of 6. There is small residual value of the dispersion due to the crossing scheme but the optics in the triplet and MS is sufficiently independent for a matching of β, α without changing the dispersion.

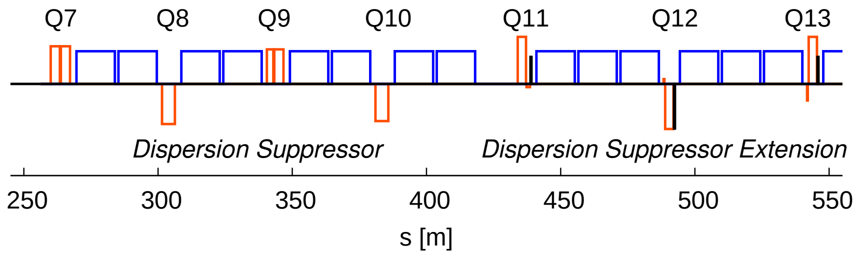

Figure 2.8: Structure of the LHC dispersion suppressor at one side of the IP. It is made of two missing dipole cells and one half arc cell.

2.2.3 Matching and Flexibility for $\beta^*_{x,y}$

The triplets and the matching sections make the transition of the optical function between a large divergence in the IP and a small divergence in the arc. In principle there are enough independent variables to match a large number of configurations, $\{\beta^*_x, \beta^*_y\}$, to the arc optics. The constraints come from:

- **Magnet strength:** The maximum magnetic field at the coil of the magnet imposes a maximum gradient in the quadrupoles.

- **Aperture:** Too large beams in the vacuum pipe can cause some particles to be lost and/or requires very small gaps at the collimators to protect the magnets.

- **Inner normalized separation:** From (1.108) this crossing parameter (Δ_{in}) limits the value of β^* in the crossing plane, β^*_{cro}, for a given emittance and crossing angle.
- **Powering:** Due to the actual cabling/powering scheme as well as a possible interplay between the two apertures, the powering ratio for the equivalent twin aperture magnets, $\kappa_I = I_1/I_2$, for the two beams must fulfill

  $$0.5 < \kappa_I < 2. \tag{2.10}$$

  This constraint arises since each magnet is coupled with the equivalent magnet for the other beam, sharing wires, and the current in one magnet should not exceed twice the value of the other, as the magnet strength is proportional to the magnet current.
- **Chromaticity:** The matching should be as smooth as possible, minimizing the product ($\beta_{x,y}k$) for each quadrupole, in order to contribute as little as possible to the chromaticity, whose correction in the arcs is limited.

The β in the final triplet increases when β^* decreases. In addition, the protons are injected in the LHC at 450 GeV [33], and then accelerated to 7 TeV. In this process, the emittances in the two planes vary considerably due to the adiabatic damping, and so do the beam sizes. The low β^* forces a high β in the final-focus. The latter is designed to optimize luminosity at the collision energy (low emittance). The low energy at injection (compared with collision) implies much bigger emittance than in collision, causing a larger beam size and less aperture in the final triplet. That is why another IR optics is needed at injection, with a large β^*. For the case of the arc optics, as there is enough aperture in the quadrupoles, the optics at injection is the same as in collision.

2.3 The LHC Chromatic Correction

The chromaticity of the LHC is corrected in the arcs, where sextupoles are placed next to the main quadrupoles of the FODO cells. This is the place where the betatron function in one plane is much bigger than in the other, hence the sextupoles are contributing to the chromatic correction in that plane. The geometric aberrations are mutually cancelled in first order between sextupoles on the same sign. As the phase advance per cell is $\sim \pi/2$ rad, each sextupole cancels its aberrations with its equivalent one two cells further. The phase advance over two cells is π rad in the two planes, following the first correction scheme in Table 1.1.

Figure 2.9 shows the contribution of the different sections to the chromaticity for the nominal LHC. It has been computed by integrating (1.94) and (1.95). In the plot, the IR sections comprise the corresponding straight section and the part of the dispersion suppressor corresponding to the two missing dipole cells per side. Consequently, they do not include any chromatic sextupoles. All of the latter are contained in the arc sections. We can see how most chromaticity is generated in the IRs, even though they are much shorter than the arcs (851.5 m versus 2480.4 m). In particular, IP1 and IP5 generate more chromaticity due to the lower values of β^*, which implies a larger β in the quadrupoles and higher quadrupole strengths.

Total natural chromaticity is $Q'_x = -136.36$, $Q'_y = -131.56$. From the analysis of the corrected chromaticity we see that all is corrected in the arcs, approximately 10 units in both planes per arc section. The total corrected chromaticity is $Q'_{x,y} \approx 2$ for both planes.

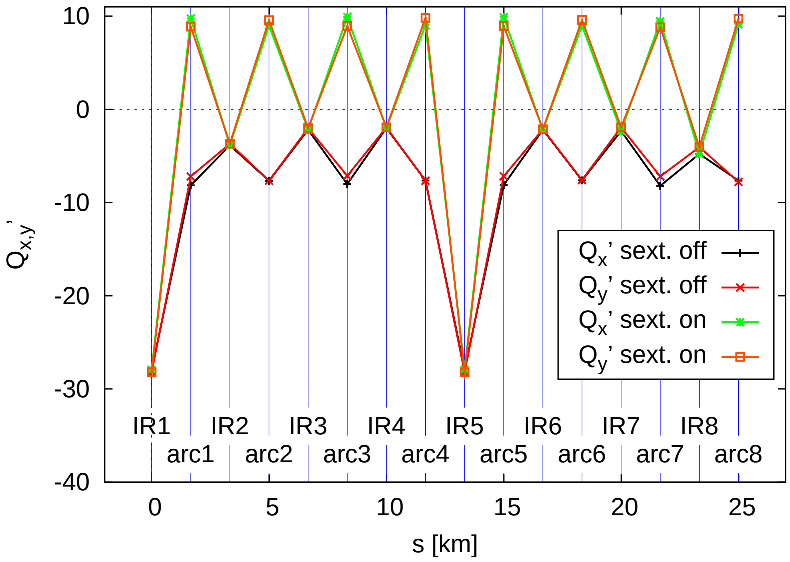

Figure 2.9: Chromatic contributions of the different LHC sections with the sextupoles switched off and on, respectively. The horizontal axis represents the central position of each ring section.

The reason why the chromaticity is not totally corrected to zero, but (∼ 2), is to avoid a fast growth of the head-tail instability, commented on Sec. 1.5. In order to correct the same amount of chromaticity in the two planes, the strength of the positive sextupoles is weaker compared with these of the negative sign. This is because the dispersion is greater at the focusing than at the defocusing quadrupoles (See Fig. 2.6 and Fig. 2.7).

The limit of the chromaticity in the current scheme is $\beta^* = 0.35$ m. If β^* is squeezed more, the negative sextupoles would exceed their maximum strength (See [34]). To solve this problem and to allow for lower values of β^*, there are two solutions. One is to increase β in the arcs (Sec. 3.1.1). The other is correcting part of the chromaticity in the interaction regions by installing sextupoles and introducing non-zero dispersion (Sec. 3.1.3).

2.4 LHC Limitations, Achievements

The LHC was designed assuming a maximum tune shift of 0.015. For the LHC, ignoring the small contribution of the nominal crossing angle, the tune shift per IP (1.100) simplifies to

$$\xi_{x,y} = \frac{N r_p}{4\pi\epsilon_N}. \tag{2.11}$$

This is independent of the β^*. This is the reason why the three head-on experiments (The two high luminosity plus IP8) give the same tune shift, even though the β^* in IP8 is one order of magnitude bigger than IP1 & IP5. Then, the maximum tune shift per IP is 0.005. Regarding the other interaction point, IP2, it features off-center collisions with a negligible contribution to the tune shift.

In 2012 a total tune shift of 0.034 was achieved with bunches colliding at two IPs [35]. However, the beams where made of a single bunch, so that the effect of the long-range interactions at this tune shift is still unknown.

2.5 LHC Future Plans

2.5.1 Luminosity Increase: HL-LHC

To extend the discovery potential of the LHC, a major upgrade will be done around 2020 in order to increase its luminosity by a factor of 5–10 beyond its original design value, for IP1 & IP5. This will enable reaching the goal of $L_{int} = 3000\ \mathrm{fb}^{-1}$ per high luminosity interaction point, over a period of approximately 10 years. Several optics are being developed considering two technologies for the superconductor magnets, NbTi and Nb_3Sn. The first one is the one used for the LHC, where the magnets can reach 8.3 T. The second one will permit building magnets up to 13 T of peak field, so that much higher gradients or larger apertures can be achieved for the quadrupoles.

The luminosity increase is realized by an increment on the number of particles per bunch and from a squeeze of the beam size at the interaction point. In particular, values as low as $\beta^*_{x,y} = 15$ cm are aimed for [36]. A reduction of $\beta^*_{x,y}$ increases the Piwinski angle due to the reduction of the transverse beam size and increase of the crossing angle required to keep a sufficiently large inner normalized separation. Denoting $\beta^* \equiv \beta^*_y = \beta^*_x$ and substituting (1.108) and (1.83) in (1.78),

$$\phi = \frac{\Delta_{in}}{2}\frac{\sigma_s}{\beta^*}. \tag{2.12}$$

For constant Δ_{in} and σ_s, the Piwinski angle increases like $1/\beta^*$ as β^* shrinks. The luminosity reduction factor decreases. As a result, the further luminosity gain due to β^* reduction is small.

Another limitation is imposed by the maximum pile-up. The detectors will be upgraded to be able to process up to 140 events. This implies a maximum peak instantaneous luminosity of about $5 \times 10^{34}\ \mathrm{cm}^{-2}\ \mathrm{s}^{-1}$ for 2808 bunches and $2.5 \times 10^{34}\ \mathrm{cm}^{-2}\ \mathrm{s}^{-1}$ for 1404 bunches. The two options for the number of bunches are those presently considered for the upgrade. They correspond respectively to a bunch separation of 25 and 50 ns.

Other ideas that are being explored for the HL-LHC are the use of crab-cavities to rotate the bunches before and after the collision and so as to avoid the geometric luminosity reduction [37]; and the luminosity levelling, to maximize the integrated luminosity per run with limited pile-up [38].

2.5.2 Energy Upgrade: HE-LHC

A new physics horizon may appear for collisions beyond 7 TeV. After some years of LHC operation at $E_{cm} = 14$ TeV, it will become clear if a new outcome of physics knowledge can be gained at higher energies.

According to (1.26), there are two ways to increase the energy, either by increasing the curvature radius in the arcs, which would mean to build a new tunnel, or by increasing strength of the bending magnets. The second option is called HE-LHC [39]. The two options together can boost the energy even more, up to $E_{cm} = 100$ TeV for the so-called VHE-LHC. Operation at these energies leads to a substantial emission of synchrotron radiation, contrary the proton machines built till this moment. Chapter 6 explains the considerations to be taken into account and proposes an interesting solution for the HE-LHC or VHE-LHC, profiting from the large synchrotron radiation in these future machines.

2.5.3 Electron-Proton Collisions: The LHeC

A promising upgrade for the LHC consists on providing both proton-proton and electron-proton collisions at different interaction points. In the new electron-hadron collider, the LHeC, electrons of 60 to possibly 140 GeV collide with LHC protons at 7 TeV. The two kind of collisions occur simultaneously, as the LHeC is designed to be built and operated while the HL-LHC runs. Chapter 7 includes a discussion of different options for a final-focus system for the LHeC electron line.

2.6 Conclusions

- We have described mathematically the different symmetric configurations in particle accelerators in general. An antisymmetric optics Beam 1/Beam 2 is mandatory for accelerators where the colliding particles have the same sign charge and with a small crossing angle like the LHC.
- We have made an analysis of the chromaticity correction in the LHC, where basically most of the chromaticity is generated in the IRs and then corrected in the arcs.

3. Novel Elements for an LHC Luminosity Increase

In this chapter some novel concepts for luminosity increase are explained. Local chromatic correction and flat beams are proven to be successful for linear colliders. On the other hand, the use of large Piwinski angle (LPA) and crab-waist collisions have been demonstrated as an effective way of increasing luminosity for circular lepton colliders. Also included is an experimental study of the crab-waist collisions which was performed at DAϕNE.

3.1 Chromatic Correction

3.1.1 ATS (Achromatic Telescopic Squeeze)

One of the solutions addressed in Sec. 2.5.1 to allow a lower β^* and correct the generated chromatic aberrations is to raise the β in the sextupoles. The correction each sextupole makes to the total chromaticity is proportional to $(\beta_x k_s D_x)$ (horizontal) and $(-\beta_y k_s D_x)$ (vertical), increasing the potential to correct more chromaticity. This scheme allows $\beta^*_{x,y} = 15$ cm, boosting the LHC luminosity thanks to the beam size reduction at the IP [40].

3.1.2 The Local Chromatic Correction Scheme

The chromatic correction in the LHC (commented in Sec. 2.3) is realized by sextupole magnets located in the arcs. These sextupoles can correct the chromaticity generated over the entire ring, including the interaction regions and for the nominal IP beta functions, thanks to the high value of dispersion in the arc locations. Attempts to increase the luminosity through a reduction in β^* encounters a limit from the chromatic correction scheme. As β^* decreases the β-functions in the quadrupoles of the final focus system grow, increasing the overall chromaticity, until the maximum strength of the correcting sextupoles in the arcs is reached, for a β^* of about 30 cm (without the so-called "ATS" optics). On the other hand, when the chromaticity is not locally corrected, intrinsic limitations restrict the momentum bandwidth of the system due to the fact that the phase relations between sextupoles and the final focus system are broken for off-momentum particles. A scheme to correct chromaticity locally was proposed in 2001 for linear colliders [41, 42]. Here two sextupoles are used to correct chromaticity, one for each plane; and two or more sextupoles to compensate the geometric aberrations generated by the other two.

3.1.3 Local Chromatic Correction for the LHC

Several past studies considered the possibility of performing a local chromatic correction in the LHC ([34], [43], [44]). An LHC with local chromatic correction would allow for a lower β^* decrease and larger off-momentum dynamic aperture. Local chromatic correction requires sextupole magnets to be installed in the IR as well as significant non-zero dispersion at some of these sextupoles. Ideally, the IR sextupoles would be installed at places where the β-function in one plane is much larger than in the other plane. These conditions are not met for the present LHC final focus scheme, which is based on a triplet. It should be noted that the proposed muon collider also makes use of a similar option [45].

3.2 Flat Beams

The LHC IRs are designed for “round beam” collision. For the nominal LHC, β^* has the same value in the two transverse planes. It is difficult to achieve a high ratio β^*_x/β^*_y with the present final-focus scheme involving triplet focusing. For a proton machine the normalized emittances are preserved and at the LHC they have the same value in the two planes. This is not the case for lepton colliders, where usually the horizontal emittance is much bigger than the vertical one, which corresponds to the natural equilibrium in the presence of strong synchrotron radiation. These flat beams facilitate the use of unequal β-functions in the two planes, e.g. by equalizing the beam divergence. It easily yields for the final quadrupoles with negative strength (vertically focusing) the possibility to implement a local chromatic correction.

The unequal β^* also helps in terms of beam separation. The inner normalized separation (1.75), that can be written as $\Delta_{in} = \theta\sqrt{\beta^*_{cro}/\epsilon}$, gets smaller as β^*_{cro} decreases, for a given crossing angle. By keeping the same θ and the same product $\sigma^*_x\sigma^*_y$, increasing β^*_{cro} and reducing β^* in the other plane enlarges Δ_{in}. Conversely, if Δ_{in} and $\sigma^*_x\sigma^*_y$ are held constant while the beam size aspect ratio (σ^*_x/σ^*_y) is modified, the luminosity grows together with the beam size in the crossing plane. Figure 3.1 shows the luminosity for different values of the flat-beam factor $(f = \sigma^*_x/\sigma^*_y)$. The crossing angle has been varied to keep the beam separation at $9.8\sigma_{cro}$ while $\sigma^*_x\sigma^*_y$ varies. Here we see how luminosity rises as the beams become flatter.

On the other hand, $\beta^*_x \neq \beta^*_y$ breaks some symmetries. Relations (2.6), (2.7), (2.8) and (2.9), valid for $\beta^*_x = \beta^*_y$, define only two different β-functions (See Figs. 2.3 and 2.4). For flat beams, these relations are no longer valid, and instead, the following conditions apply, that define four independent β-functions:

$$\beta^1_x(s) = \beta^2_x(-s);\ \alpha^1_x(s) = -\alpha^2_x(-s), \tag{3.1}$$

$$\beta^1_y(s) = \beta^2_y(-s);\ \alpha^1_x(s) = -\alpha^2_x(-s), \tag{3.2}$$

$$\beta^2_x(s) = \beta^1_x(-s);\ \alpha^1_x(s) = -\alpha^2_x(-s), \tag{3.3}$$

$$\beta^2_y(s) = \beta^1_y(-s);\ \alpha^1_x(s) = -\alpha^2_x(-s). \tag{3.4}$$

It should be noted that a proposal for flat beams was already made to increase luminosity

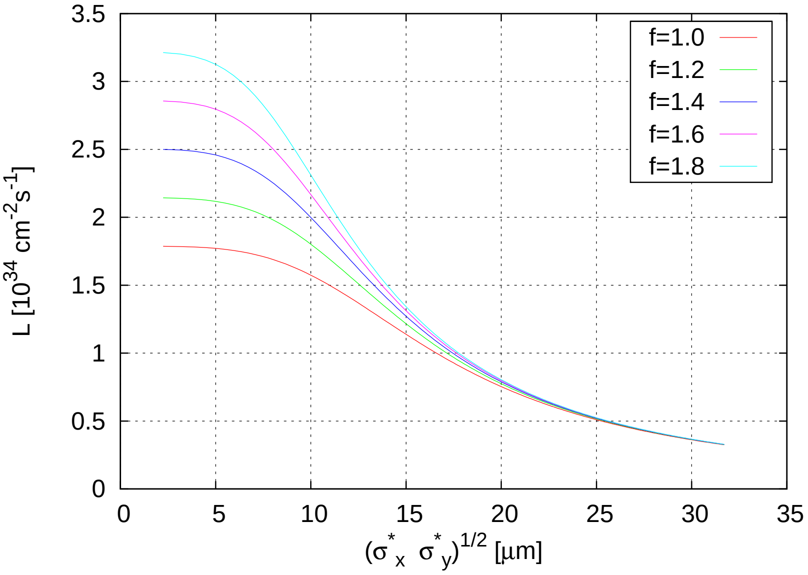

Figure 3.1: Luminosity for different flat-beam factors (f). The crossing angle is varied in each case to have an inner normalized separation of Δ_{in} = 9.8.

using present LHC hardware, with a β-ratio of 2 [46].

3.2.1 A New Flat-Beam Optics for Present LHC

A new optics has been designed for beam tests with moderately flat aspect ratios at the present LHC. The objective is to study “quasi” flat-beam conditions in a Machine Development (MD) session, in order to explore the resulting tune shifts, lifetime, effects of transverse offsets, and especially sensitivity to long-range beam-beam effects.

The new quasi-flat optics developed for the present LHC has been obtained after a squeeze process from a round beam optics with $\beta^*_{x,y} = 1.20$ m. Specifically, the starting point is a present LHC optics shown in Fig. 3.2 for Beam 1 and in Fig. 3.3 for Beam 2. From this optics, a squeeze in the horizontal plane was computed for IP1 till $\beta^*_x = 0.60$ m. The squeeze maintains $\beta^*_y = 1.20$ m, while intermediate new optics with $\beta^*_x = \{1.05$ m, 0.90 m, 0.75 m$\}$ were matched so as to provide a smooth transition from $\beta^*_x = 1.20$ m to 0.60 m. The final optics for IR1 is represented in Figs. 3.4 and 3.5. We can see the four different β-functions which fulfill the relations (3.1), (3.2), (3.3) and (3.4).

For IR5 the role of the two planes is changed, in order to have the squeeze in the non-crossing plane, and here β^*_y is decreased to 0.60 m (see Figs. 3.6 and 3.7). Two sets of four new optics have been computed for either IR. The possibility of obtaining a considerably smaller value for $\sigma^*_x\sigma^*_y$ is limited by the triplet FF system. Also, a high beam size aspect ratio (σ^*_x/σ^*_y) is not achievable with conventional single-aperture quadrupole magnets in the triplet.

The magnets whose strength is modified during this squeeze are Q4 to Q10 together

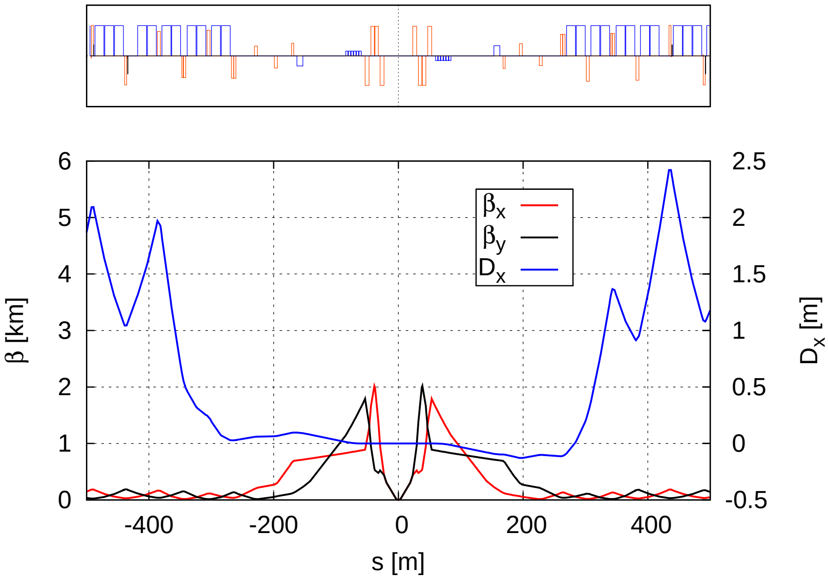

Figure 3.2: Beam 1 IR optics for β_x^*/β_y^* = 1.20 m/1.20 m, used in IR1 & IR5.

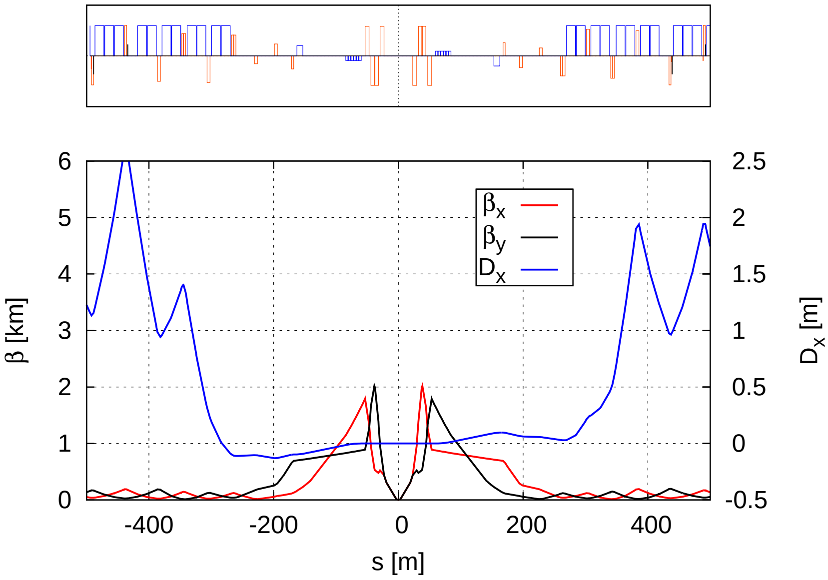

Figure 3.3: Beam 2 IR optics for β_x^*/β_y^* = 1.20 m/1.20 m, used in IR1 & IR5.

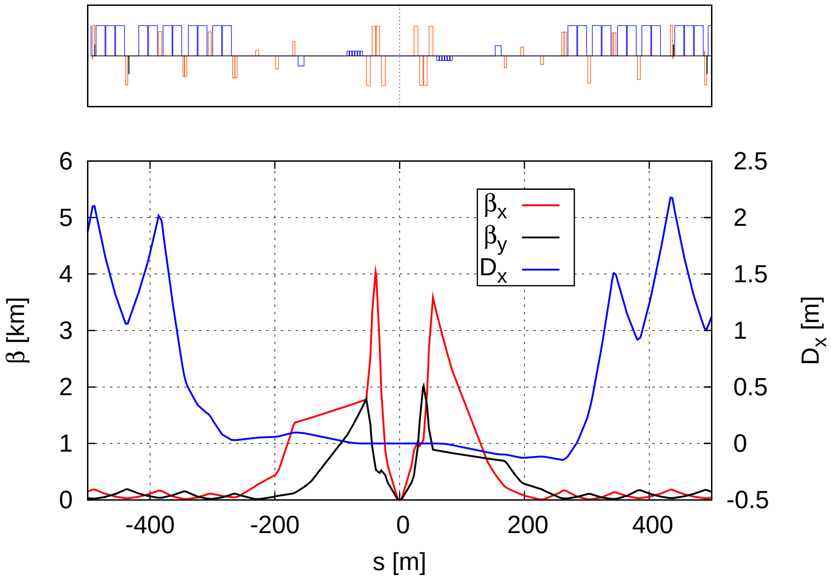

Figure 3.4: Beam 1 IR optics for $\beta^*_x/\beta^*_y = 0.60$ m/1.20 m, used in IR1.

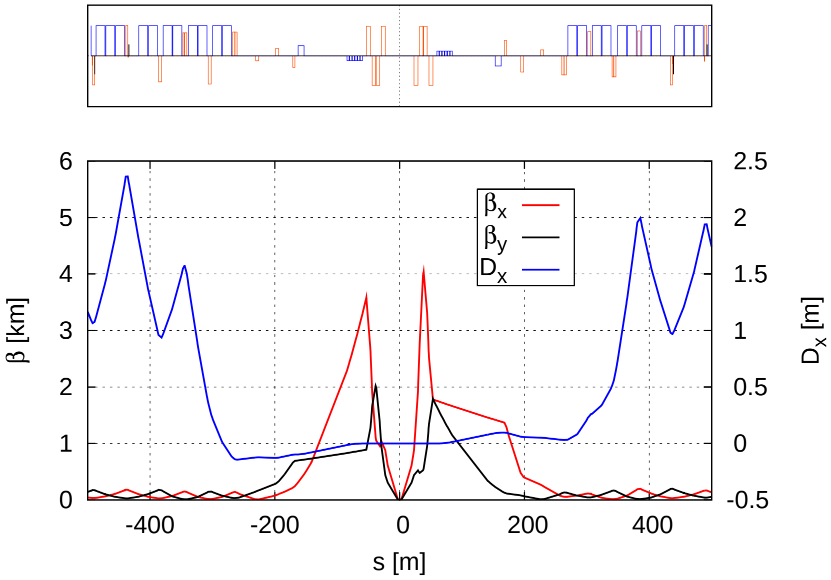

Figure 3.5: Beam 2 IR optics for $\beta^*_x/\beta^*_y = 0.60$ m/1.20 m, used in IR1.

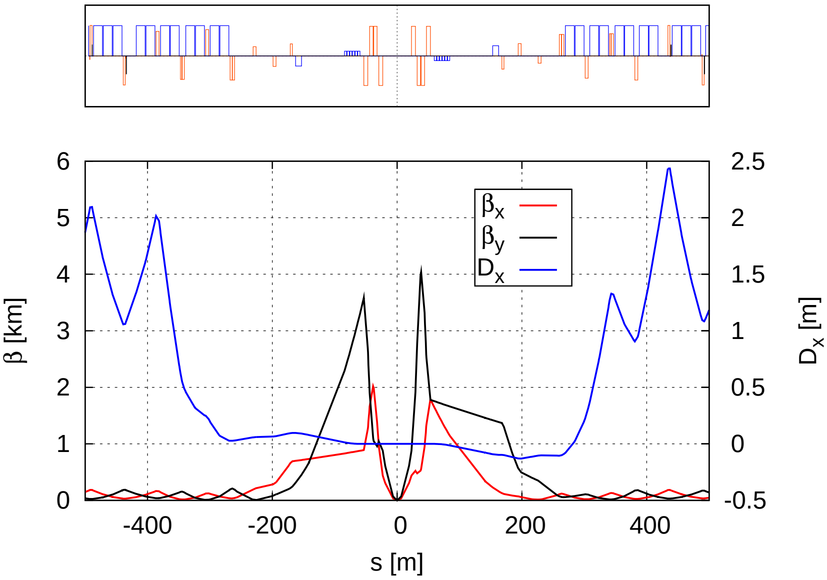

Figure 3.6: Beam 1 IR optics for $\beta_x^*/\beta_y^* = 1.20$ m/0.60 m, used in IR5.

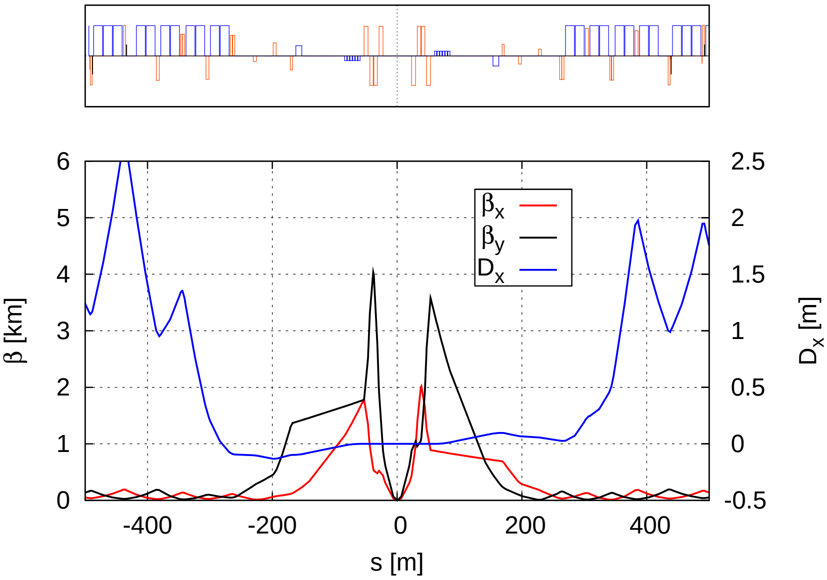

Figure 3.7: Beam 2 IR optics for $\beta_x^*/\beta_y^* = 1.20$ m/0.60 m, used in IR5.

with the trim quadrupoles QTLI.11, QT12 and QT13. Magnets Q1, Q2 and Q3 have not been modified in order to do an independent matching in the two beams. A matching involving modifications in the triplet magnets would have implied performing a combined matching for the two beams, since these magnets affect both Beam 1 and Beam 2 optics.

Figures 3.8 and 3.9 show the strength of the main quadrupoles for the horizontal and for the vertical squeeze, respectively. In each plot there are four curves for each Qi: two per IP side and two per beam. We can see that all the powering curves for each individual magnet are monotonic. This monotonicity prevents the magnets from switching between different hysteresis branches, that would produce unexpected response of the magnet strength for a given current. This constraint implied doing several iterations so that every single curve does not enter in hysteresis, this process being more complicated as the number of matched optics increases. It was also verified that for each pair of implicated two-in-one magnets, their powering ratio fulfills the condition given by the powering scheme (2.10).

Another constraint that was considered when designing the new set of optics is the β-beat between the different computed points. Between two matched optics, the magnet currents are obtained by linearly interpolating the magnet current from the two adjacent end values. However, due to the non-linearity of the system, when all the magnets use interpolated current values, the result is a non-perfectly matched optics and, as a result, there is a small beat of the β-function over the entire ring. Unlike the other constraint, this effect is inversely proportional to the number of matched optics. Figure 3.10 shows, for Beam 1 and Beam 2, the maximum of the β-beat over all beam position monitors (BPMs) with simultaneous squeeze in IP1 and IP5 of the corresponding β^* in the non-crossing plane, making the transition of β_{sq} from 1.2 m to 0.6 m. This value is always below 0.6 %, and hence negligible.

The process can be summarized as follows:

1. Define the final optics ($\beta^*_{x,y}$). Compute the optics.
2. Establish a starting optics.
3. Define a number of points for the intermediate optics.
4. Compute the optics for each intermediate set of $\beta^*_{x,y}$.
5. Check monotony of the curves in the magnets.
6. Interpolate the optics and check β-beating.

If the beat of the β-function is too large, the process should start again at point 3 and the number of intermediate optics increased. All of this process was repeated for a thin-lens version, a model of the LHC where all the elements have zero length. This was done in order to perform beam-beam simulations prior to the MD, with the advantage of much shorter computation times. A verification process was done to check that the optics parameters do not vary much from the thick-lens model. For both cases (thick and thin models), the orbit bumps were calculated for appropriate crossing angle and to perform beam separation.

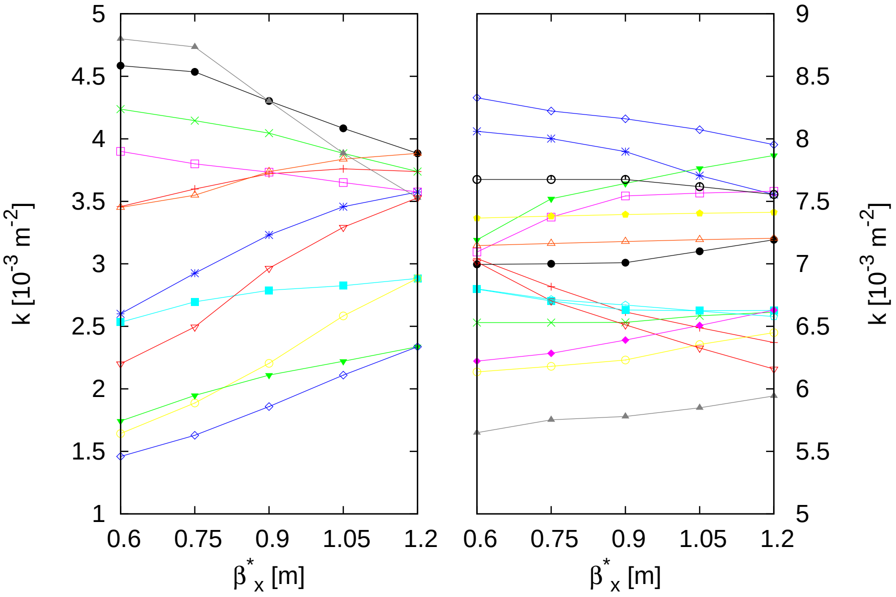

Figure 3.8: Magnet strength for the horizontal squeeze in IP1. Magnets Q4–Q6 are plotted in the left and magnets Q7–Q10 in the right.

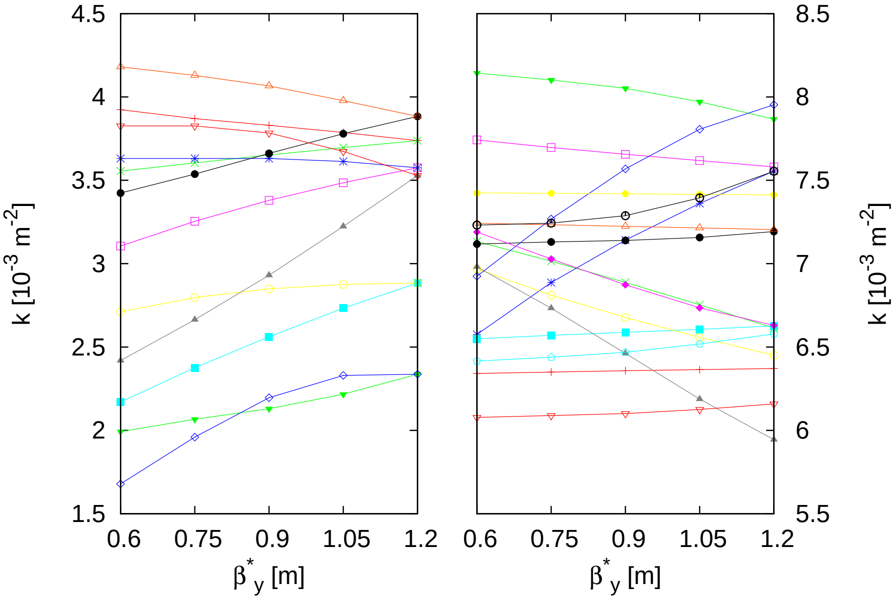

Figure 3.9: Magnet strength for the vertical squeeze in IP5. Magnets Q4–Q6 are plotted in the left and magnets Q7–Q10 in the right.

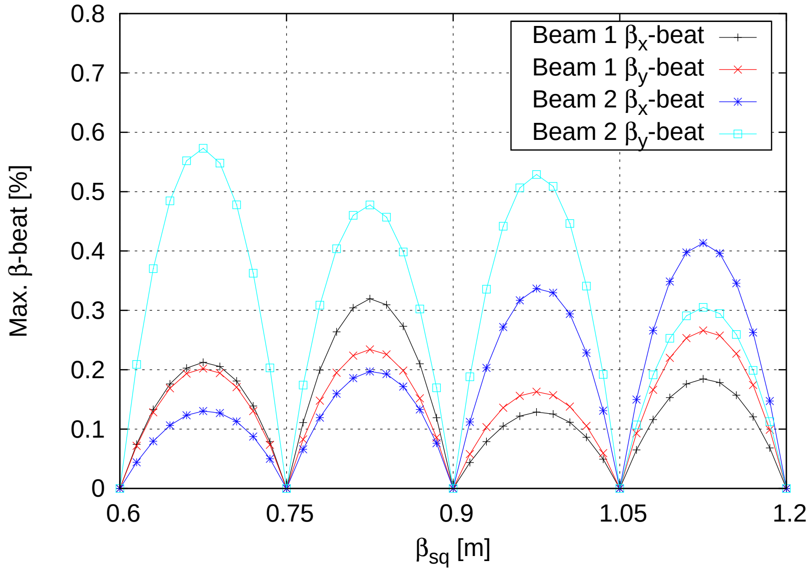

Figure 3.10: Maximum β-beat over BPMs for Beam 1 and Beam 2 with $\beta_x^* = \beta_{sq}$, β_y^*= 1.2 m in IP1 and β_x^*= 1.2 m, $\beta_y^* = \beta_{sq}$ in IP5.

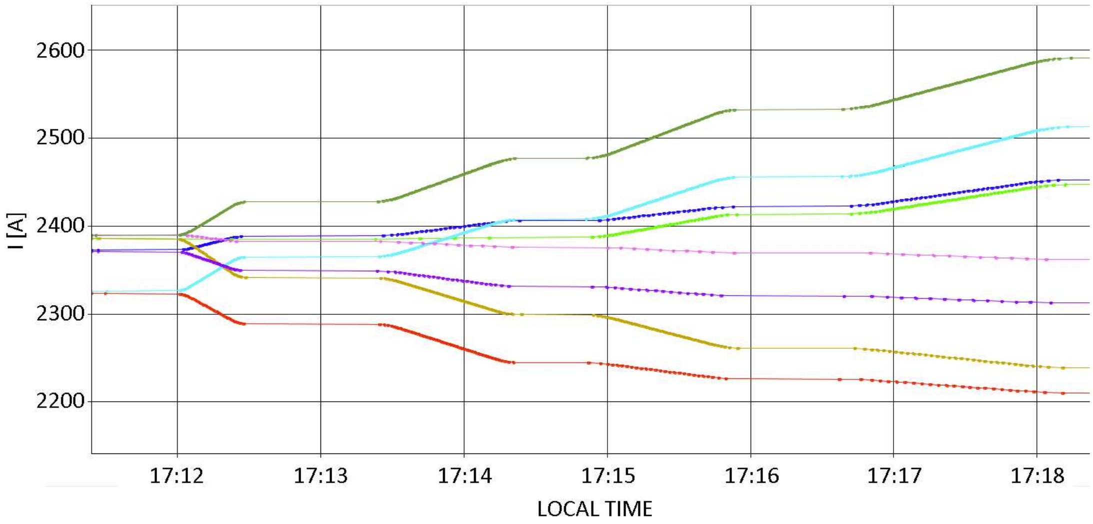

Figure 3.11: Evolution of the measured current of the Q9 magnets during the dry run. Each flat region corresponds to a matched optics.

Finally, the computed squeeze was implemented in the LHC control system and the magnet cycle was executed successfully without beam [47]. It was confirmed that no switching between magnet hysteresis branches was present. Figure 3.11 shows an example for the 6 magnets Q9. Each of the plots represents the measured current for this magnet at both sides of the IP, for both beams and for both IRs, during the squeeze process. It shows a smooth transition of the magnet coil current, revealing the ability of the power converters to perform the complete squeeze, which was done in 375 seconds.

Due to lack of time in the LHC schedule, the MD finally did not take place in 2012, but it will probably be performed in the LHC run at 7 TeV per beam in 2015.

3.2.2 Limitation of the Antisymmetric Optics for Flat Beams

For the round optics of the present LHC the β–functions for each beam are antisymmetric, as illustrated in Figs. 3.2 and 3.3, that is, the optics for one plane on one side of the IP is identical to the optics of the other beam in the other plane or of the same beam on the other side of the IP in the orthogonal plane. When flat beams are introduced, in Figs. 3.4 and 3.6, four different optics emerge, and for each of them, in case of a local chromatic correction, two pairs of sextupoles must be added with a spacing of π rad in phase advance. This greatly complicates the implementation of a local chromatic correction based on the present LHC optics.

3.3 Large Piwinski Angle

Collisions with a large Piwinski angle ($\phi > 1$) are considered for future LHC upgrades [48]. They also naturally occur in scenarios for 7 TeV operation with 50 ns bunch spacing after the Long Shutdown 1 (2013/14). The Piwinski angle is increased by reducing the beam size in the plane of crossing. This is the case for future LHC upgrades where a luminosity increase is targeted through a significant reduction in the β-function, like the so-called ATS optics. The Piwinski angle can also be enhanced by a corresponding increase in the crossing angle, such as for the crab-waist collision scheme proposed in this thesis. Though an increase in the Piwinski angle reduces the geometric luminosity as $L \propto 1/\sqrt{1+\phi^2}$, it also has several advantages: Firstly, it mitigates the hourglass effect thanks to the reduction in the length of the bunch overlapping area, supporting a significant reduction of the β^*. Secondly, it decreases the beam-beam tune shift by about the same reduction factor as for the luminosity, so that operation at the same tune shift becomes possible while storing much brighter beams [13], that is, beams with large N/ϵ_N. On the other hand, with a transverse offset in the plane of crossing we can move the longitudinal collision point (CP), given by the encounter with the axis of the opposite beam, with respect to the ideal IP. This excites betatron and synchro-betatron resonances by the coupling of transverse and longitudinal motion. Also, the large Piwinski angle breaks the collision symmetry, which may be essential for operation with a high beam-beam parameter [49], [50].

3.3.1 Large Piwinski Angle for the LHC

In 2012, an MD was performed at the LHC to study beam-beam effects in the presence of a large Piwinski Angle [51], larger than in earlier studies [52]. Strong-strong simulations for the LHC MD configuration were performed by K. Ohmi (KEK, Tsukuba. Japan), who also did some previous studies on the large Piwinski angle for the LHC [53]. The results are shown in Fig. 3.12, where the simulated luminosity and the luminosity lifetime are plotted as a function of the crossing angle.

There are two competing effects of the Piwinski angle on the luminosity lifetime, each of them dominating in a certain range of the crossing angle.

1. The beam losses increase as a consequence of the excitation of nonlinear betatron and synchro-betatron resonances. In fact, collisions with a large Piwinski angle induce resonances [54].

2. The beam-beam tune shift gets reduced through a decrease in the geometric reduction factor.

As can be seen in Fig. 3.12, the first effect is dominant for crossing angles smaller than about 1 mrad, and it roughly compensates the effect of the second between 1.0–2.0 mrad. Finally, for crossing angles bigger than 2.0 mrad the second factor dominates and the luminosity lifetime increases significantly, while the value of the luminosity and the beam-beam tune shift decrease.

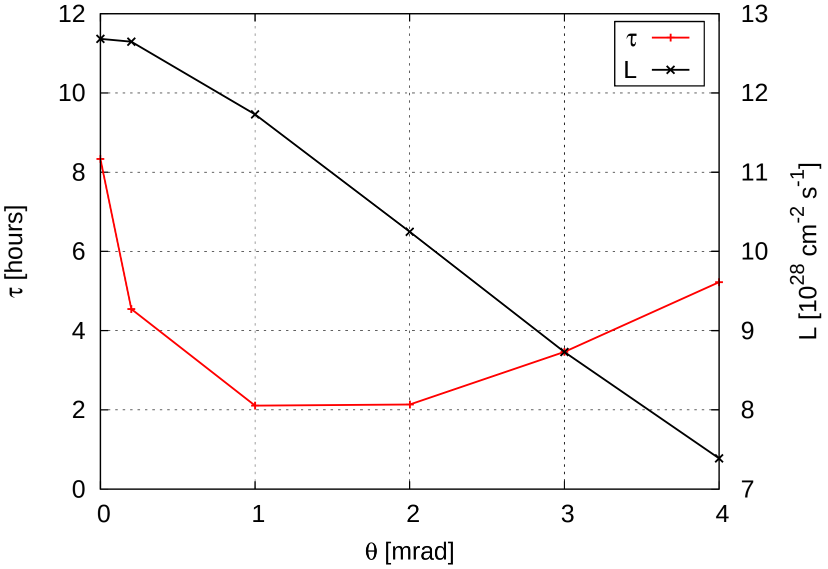

Figure 3.12: Large Piwinski angle simulation, showing the influence of the crossing angle θ over luminosity lifetime and luminosity. Courtesy of Dr. Kazuhito Ohmi.

The corresponding MD was performed with beam to study the effect of the LPA on LHC luminosity and to benchmark the simulation. Two high brightness bunches per beam were collided at 450 GeV (LHC injection energy) with varying spectrometer strength in IP8 so that the corresponding Piwinski angle was changed in the range 0.2–1.2, achieving the highest Piwinski angle ever reached in a hadron collider. Table 3.1 shows the bunch lifetimes for different conditions of the spectrometer. We have to take into account that there are some transient effects due to the orbit correction and the stationary state may not have been achieved. That is why a second hit has been performed over a longer time window, in Table 3.1 referred to as the '50 % ext. int.' For each beam, the bunch denoted as 'A' collided in IP8 while 'bunch B' experienced collisions in IP1, IP5 and IP8, increasing its tune spread.

The experiment was not fully conclusive due to unrelated technical problems and missing data from two of the LHC experiments, and should be repeated with more intermediate points. However, the results obtained appeared to be roughly consistent with the simulated behaviour of Fig. 3.12. Beam 1 better resembles the results of the simulations. For bunches A and B the lifetime first decreases and then increases with the Piwinski angle.

Table 3.1: Piwinski angle and bunch lifetimes for different strengths of the spectrometer during the LPA MD.

	Beam 1			Beam 2		
spectrometer str.	ϕ	$\tau_{bunch\ A}$ [h]	$\tau_{bunch\ B}$ [h]	ϕ	$\tau_{bunch\ A}$ [h]	$\tau_{bunch\ B}$ [h]
100 %	1.16	4.8	1.44	1.34	7.6	1.25
50 %(30-s. int.)	0.52	3.0	2.0	0.60	5.8	1.6
50 % (ext. int.)	0.52	2.7	1.7	0.60	5.2	1.44
minimum	0.19	3.0	3.5	0.21	5.0	1.9

In any case, the strong-strong beam-beam simulations suggest that LPA operation overcomes one of the main limitations for hadron collider luminosity, namely the upper bound on beam brightness.

The use of a large crossing angle has another significant effect: the reduction of the area where most of the collisions are produced, the overlapping area. This is limited by the detection capability of the experiment, which must analyze the particles coming from a reduced space.

3.4 The Crab-Waist Collision Scheme

The resonances introduced by the LPA can be removed by means of a novel technique first introduced in DAΦNE [55], which consists in restoring, for particles with different x-coordinate at the IP (for horizontal crossing), the ideal longitudinal IP. This is done by the installation of two sextupoles with opposite sign on each side of the IP and for the two beams, at appropriate, but unusual betatron phase advance in the two planes. These sextupoles can increase luminosity by further mitigating the hourglass effect, but their main purpose is to suppress resonances, thereby allowing for higher tune shifts and LPA operation.

3.4.1 Crab-Waist Transformation

The crab-waist sextupole must be placed in a location where the phase advances from the IP are [55]:

$$\Delta\mu_x = \pi m, \qquad \Delta\mu_y = \frac{\pi}{2}(2n+1); \tag{3.5}$$

where m and n denote integer numbers. The total phase advance between the crab-waist sextupoles at both sides of the IP are $\Delta\mu_x = 0$, $\Delta\mu_x = \pi$. With those phase advances and using (A.7), the horizontal position of the particle at the IP, x_{IP}, is expressed as a function of the position just prior to the crab-waist sextupole, x_{cs}. The positive sign represents the case with $\Delta\mu_x = 0$ and the negative one, with $\Delta\mu_x = \pi$:

$$x_{IP} = \pm\sqrt{\frac{\beta_x^*}{\beta_{x,cs}}}\,x_{cs}. \tag{3.6}$$

Figure 3.13 shows the collision scheme with and without crab sextupoles. In the last case, each particle meets the center of the opposing bunch at the waist of the vertical β-function.

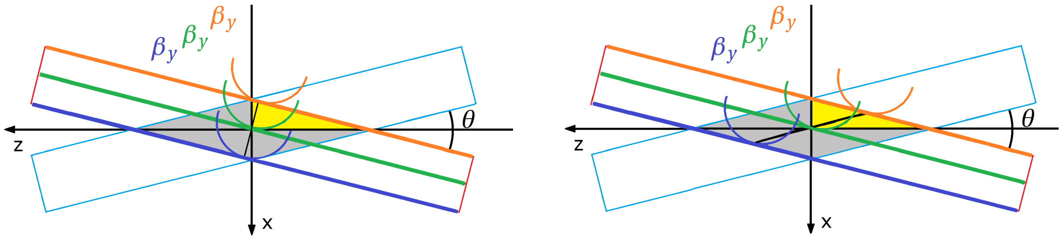

Figure 3.13: Collision scheme with LPA without the crab-waist modification (left) and with the crab-waist one (right). It is very clear how the crab-waist transformation moves the waists in β_y to the axis of the opposite bunch. The reference system has the same orientation as for LHC IP1 in Fig. 2.1.

The detail of the geometric difference between the CP and the IP is described in Fig. 3.14.

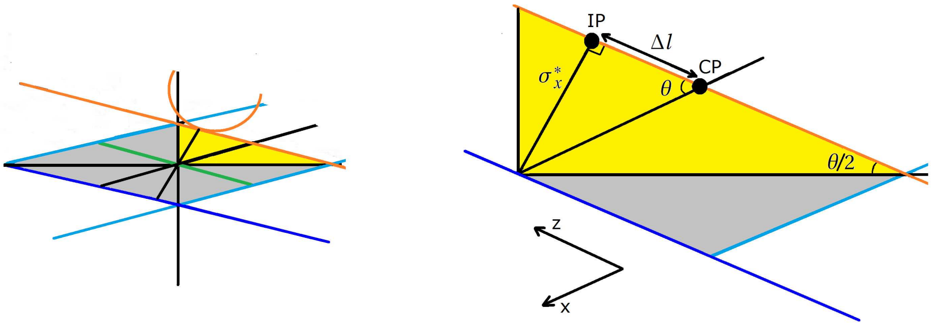

Figure 3.14: Detail of the difference between the CP and the IP. Particles with $x_\beta = -\sigma_x$ (red line) see the CP before the IP.

Consequently, the crab-waist sextupoles must move the IP (in this case, the minimum of β_y) to the CP. For $x_\beta < 0$ a focalizing effect is needed at the side of the IR prior to the IP. At the other side, the sextupole must be defocalizing for $x_\beta < 0$ to remove the aberration. The distance between the IP and the CP is given by

$$\Delta l = \frac{x_{IP}}{\theta}. \tag{3.7}$$

From Fig. 3.15 the vertical transport matrix from the sextupole to the CP is (3.8), where the upper signs represent $\Delta\mu_y = \pi/2$ and the lower ones, $\Delta\mu_y = -\pi/2$.

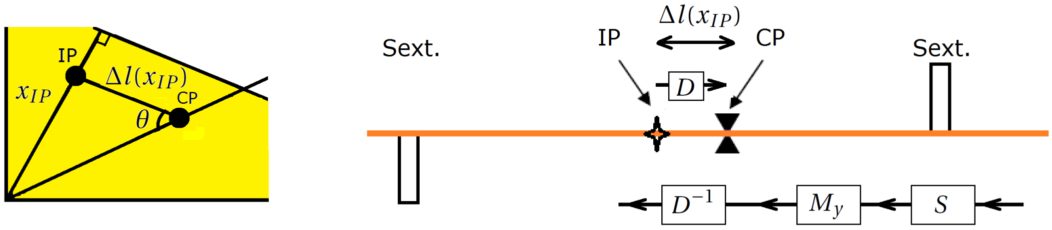

Figure 3.15: Crab-waist optical scheme for particles with $x_\beta < 0$ at the IP. The crab sextupole acts as a focusing element to bring the IP to the CP.

$$\hat{M}_y = D^{-1} M_y S = \begin{pmatrix} 1 & -\Delta l \\ 0 & 1 \end{pmatrix} \begin{pmatrix} \pm\alpha_{cs}\sqrt{\frac{\beta_y^*}{\beta_{y,cs}}} & \pm\sqrt{\beta_{y,cs}\beta_y^*} \\ \mp\frac{1}{\sqrt{\beta_{y,cs}\beta_y^*}} & 0 \end{pmatrix} \begin{pmatrix} 1 & 0 \\ -1/f & 1 \end{pmatrix}. \tag{3.8}$$

D represents the transfer matrix of a drift, M_y is the corresponding for a phase advance of $\Delta\mu_y = \frac{\pi}{2}(2n+1)$ using (A.7) with $\alpha_{CP} = 0$. The matrix S represents the focusing part of the crab sextupole. The sextupole acts as a quadrupole of integrated strength $k_l = k_{sl} x_{cs}$, i.e. it focuses the particles in the vertical plane as a function of the horizontal coordinate in the sextupole, x_{cs}:

$$f = \frac{1}{k_{sl} x_{cs}}. \tag{3.9}$$

The matrix M_y must be the same as $\hat{M}_y$. Elements $M_{y,12}, M_{y,21} M_{y,22}$ are already equivalent to the corresponding ones in $\hat{M}_y$. By setting equal $\hat{M}_{y,11} = M_{y,11}$ one obtains the relation $\Delta l f = \beta_{y,cs}\beta_y^*$, for both $\Delta\mu_y = \pi/2$ and $\Delta\mu_y = -\pi/2$. Combining this result with (3.6), (3.7) and (3.9) the integrated strength of the crab-waist sextupole is

$$k_{sl} = \pm\frac{\sqrt{\beta_x^*/\beta_{x,cs}}}{\theta\beta_y^*\beta_{y,cs}}. \tag{3.10}$$

The positive sign corresponds to horizontal phase advance from the crab-waist sextupole to the IP of $\Delta\mu_x = 0$, and the negative one, of $\Delta\mu_x = \pi$. Another sextupole with opposite strength will cancel the geometric aberrations at the other side of the IP, so that the Twiss functions will not be modified except at the region between the two sextupoles. In all the cases, the phase advances between the two sextupoles are equivalent to $2\Delta\mu_x = 0$, $2\Delta\mu_y = 2\pi$, following the third correction scheme in Table 1.1. Table 3.2 justifies the sign of the sextupoles for both beams and $s < 0$. The corresponding sextupoles at the right side of the IP ($s > 0$) have opposite sign. The case shown in Fig. 3.15 corresponds to Beam 2.

Table 3.2: Signs for the crab-waist sextupoles, for $\Delta\mu_x = 0$, $\Delta\mu_y = \pi/2$, and longitudinal positions at the left side of the IP ($s < 0$). The "focalizing properties" quoted refer to the vertical plane.

	$x_\beta < 0$	$x_\beta > 0$	sign(k_{sl})
Beam 1	defocalizing	focalizing	−
Beam 2	focalizing	defocalizing	+

The crab-waist sextupole must be placed in a peak of the vertical β-function so that its strength can be minimized. There are two contributions determining the integrated strength of the crab-waist sextupole, namely the IP parameters, and the optics location. In order to quantify the contribution from each factor, equation (3.10) can be expressed as

$$k_{sl} = \pm k_{sl,IP} \frac{1}{\beta_{y,cs}\sqrt{\beta_{x,cs}}}, \tag{3.11}$$

where the "crab-waist IP factor" is defined as

$$k_{sl,IP} = \frac{\sqrt{\beta_x^*}}{\theta \beta_y^*}. \tag{3.12}$$

The so-called "crab-waist IP factor" quantifies the contribution of the IP parameters that determine the luminosity: betatron functions at the IP and crossing angle, θ. It can be expressed as a function of the β-ratio at the IP, as

$$k_{sl,IP} = \frac{\beta_x^*}{\beta_y^*} \frac{1}{\theta\sqrt{\beta_x^*}}. \tag{3.13}$$

Consequently, the bigger the β^*-ratio is, the more difficult is to make a crab-waist transformation. The crab-waist sextupole strength is inversely proportional to the crossing angle. As the crossing angle increases, the less focusing effort is needed to bring the IP to the CP.

This collision scheme has been successfully implemented at the DAΦNE e^-e^+ collider [56]. Some experiences have been gained by exploring the effect of the crab-waist collision scheme, whose results are shown in the next section.

Crab-waist collisions were also proposed for the future electron-positron collider Super-B [57], where the use of crab-waists allows for a lower β_y^* decrease. For comparison: crab cavities allow the use of larger crossing angles due to the cancellation of the geometric luminosity reduction factor while crab-waist sextupoles cancel the hourglass effect.

3.4.2 Crab-Waist Collisions at DAΦNE

DAϕNE is an electron-positron collider working at an energy of 0.51 GeV per beam, in order to have a E_{cm} corresponding to the ϕ resonance and provide a high rate of K mesons. The collider, sketched in Fig. 3.16, consists of two independent rings and it has one interaction region (IR1) [58], which is shown in Fig. 3.17. Table 3.3 lists the IP parameters, the crab-waist IP factor $k_{sl,IP}$ (3.12), the value of β-functions in the crab-waist sextupoles and their nominal integrated sextupole strength k_{sl} (3.10) for a full crab-waist transformation. Also, the phase advances from the IP are presented.

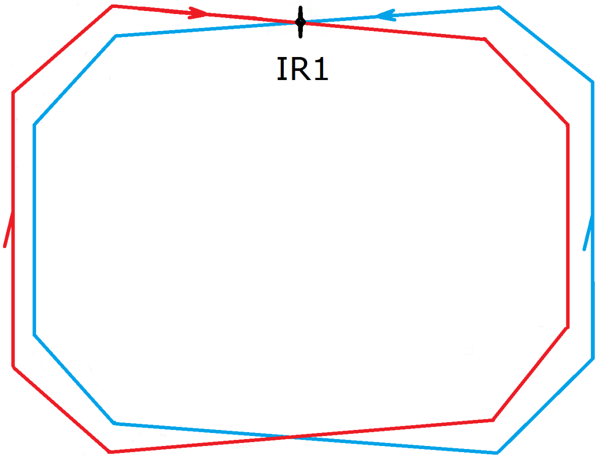

Figure 3.16: DAϕNE schematic layout. The separated lines for electrons (blue) and positrons (red) are displayed. IR1 is the only region with a interaction point. The beams are vertically separated in the diametrically opposed point.

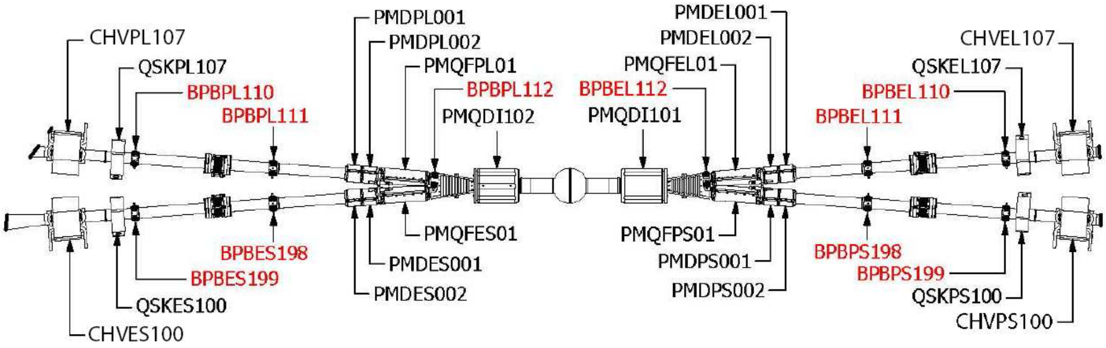

Figure 3.17: Detail of DAϕNE interaction region, showing the separated lines for each beam. Courtesy of INFN-LNF.

Table 3.3: DAΦNE parameters relevant for the crab-waist experience, for the electron and for the positron line. The blocks on the left side correspond to the IP parameters, the crab-waist sextupole on the left side ($s < 0$) and on the right side ($s > 0$).

	parameter	electron line	positron line
IP	β_x^* [cm]	28.92	29.60
	β_y^* [cm]	0.86	0.89
	θ [mrad]	85.68	
	$k_{sl,IP}$ [m$^{-1/2}$]	729.83	713.47
s<0	$\beta_{x,cs}$ [m]	3.29	3.36
	$\beta_{y,cs}$ [m]	14.78	14.20
	$\Delta\mu_x$ [π rad]	0.99	0.99
	$\Delta\mu_y$ [π rad]	1.50	1.49
	k_{sl} [m^{-2}]	−6.6	6.6
s>0	$\beta_{x,cs}$ [m]	3.53	3.62
	$\beta_{y,cs}$ [m]	14.76	14.17
	$\Delta\mu_x$ [π rad]	0.99	0.99
	$\Delta\mu_y$ [π rad]	1.50	1.40
	k_{sl} [m^{-2}]	6.6	−6.6

Optics studies were carried out at DAΦNE at the end of 2012. Figures 3.18 and 3.19 show the measurements performed in the electron and in the positron ring, respectively, and their comparison with the model. The measured values of the β-function correspond to each quadrupole. They are obtained by modifying the magnetic strength of the quadrupole and observing the change in tune produced. It is known that a quadrupole field error produces a tune shift proportional to the value of the β-function in the quadrupole [1, 9.1.1]. Then, the values of the β-function in quadrupole 'i' are obtained by measuring the change in tune ($\Delta Q_{x,y,i}$) due to a change in the quadrupole strength (Δk_i), as

$$\beta_{x,i} = \frac{4\pi\Delta Q_{x,i}}{\Delta k_i}, \qquad \beta_{y,i} = -\frac{4\pi\Delta Q_{y,i}}{\Delta k_i}. \tag{3.14}$$

The dispersion values are obtained by varying the central momentum of the beam, p by Δp. This causes a variation of horizontal coordinate of the closed orbit along all the ring, $\Delta x(s)$, that is directly measured. Substituting (1.10) in (1.29) and taking until first order, we get the linear dispersion,

$$D_x(s) = \frac{\Delta x(s)}{\Delta p} p. \tag{3.15}$$

The experimental values obtained show a very good agreement with the model. In particular, the adjustment of the betatron functions is better for high than for low values. For the dispersion, it is the opposite case and the matching is better for high values.

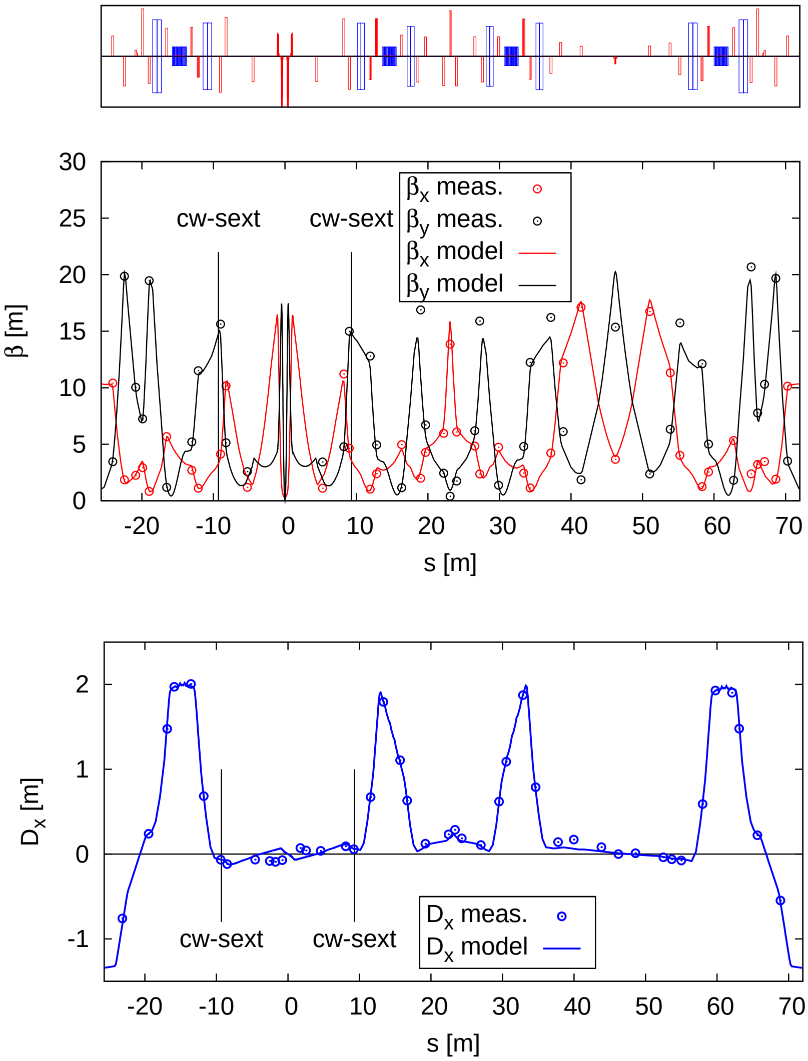

Figure 3.18: Optics measurements for the whole DAΦNE electron ring compared with the values given by the model. Dipoles and quadrupoles are represented in the upper plot.

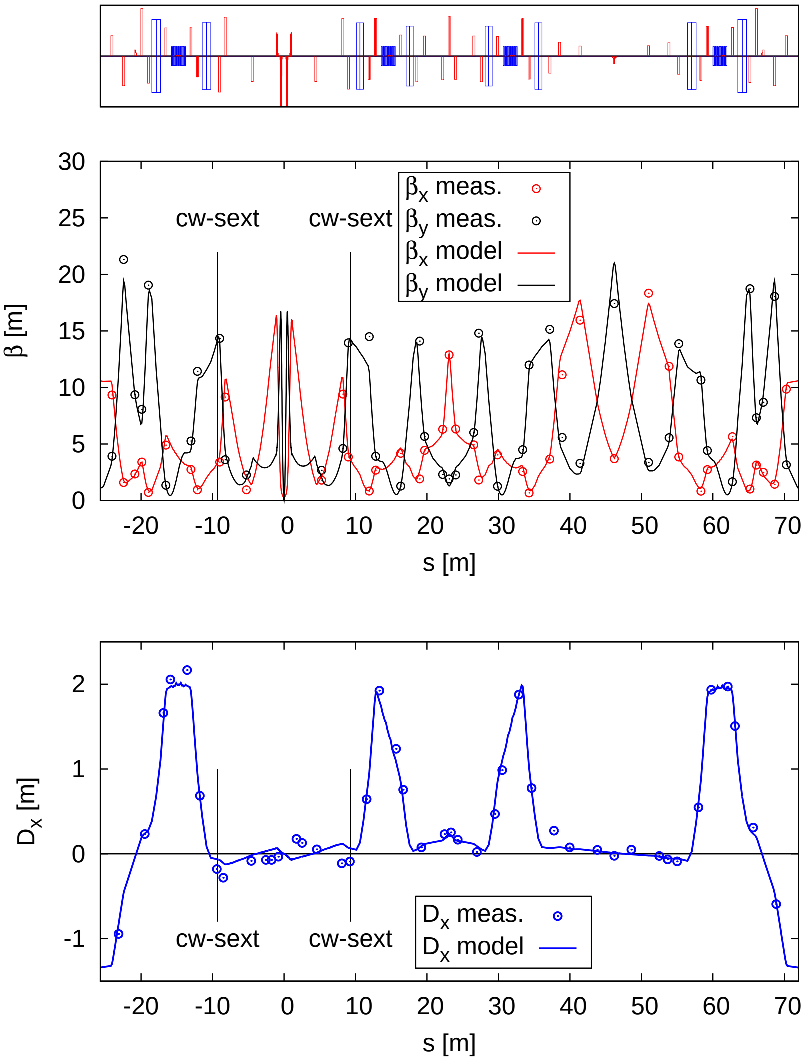

Figure 3.19: Optics measurements for the whole DAΦNE positron ring compared with the values given by the model. Dipoles and quadrupoles are represented in the upper plot.

The plots shows that the optics is “symmetric Beam 1/Beam 2” for all the ring. As the two counter-rotating beams have opposite charge sign, the field distribution is identical at each point for the two lines, even though they are independent. The optics is also “symmetric left/right” in the IR only. However, in the arcs this symmetry is broken.

Figures 3.20 and 3.21 present the energy dependence of the tune for the electron and for the positron line, respectively. In both cases the experimental results are compared with the MAD-X [59] model. These experimental points are obtained by varying central momentum in a similar way as for the dispersion measurements. As a reference, the electron tunes for on momentum particles are $Q_x = 5.07$, $Q_y = 5.17$, while for protons the tunes have the value $Q_x = 5.08$, $Q_y = 5.12$. These figures include the effect of the crab-waist sextupoles on the chromaticity. They have some influence on the chromaticity as they are located in a place with non-zero dispersion.

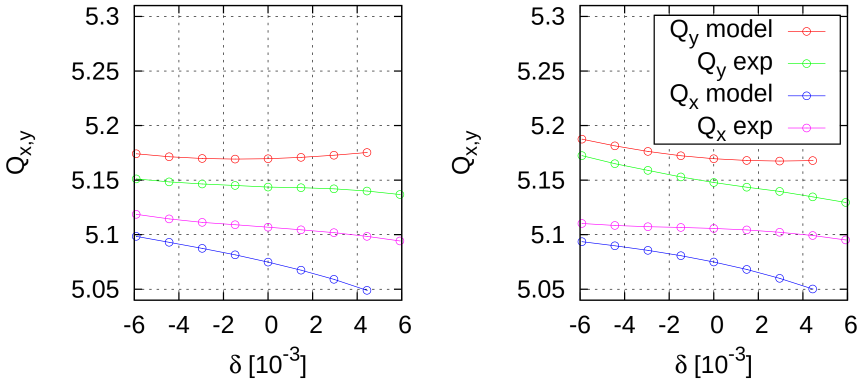

Figure 3.20: Chromatic dependence of the tune for the DAΦNE electron line with the crab-waist sextupoles off (left) and on (right).

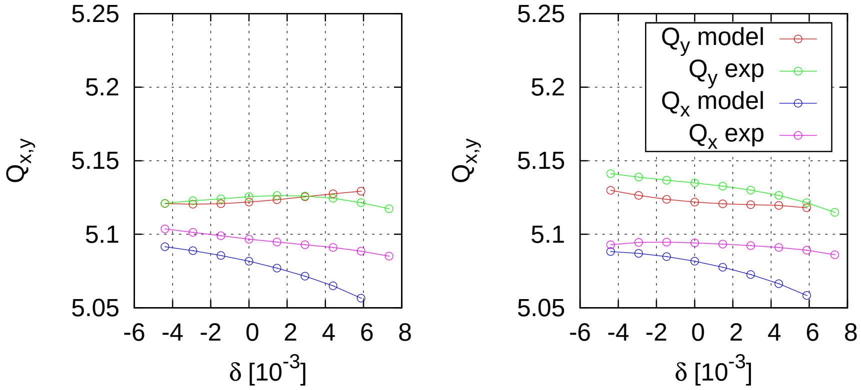

Figure 3.21: Chromatic dependence of the tune for the DAΦNE positron line with the crab-waist sextupoles off (left) and on (right).

Following the optics measurements discussed above, two experiments were performed to assess the influence of the crab-waist sextupoles on the IP beam sizes and on the luminosity.

For the first experiment performed, the powering current of the crab-waist sextupoles of the electron ring was modified from 200 A to 150 A, while the current of the positron ring was kept constant. The resulting evolution of the beam size for both lines is shown in Fig. 3.22, where we see an increase of the vertical beam size for the electrons. This is a consequence of the resonances which get stronger as the strength of the crab-waist sextupoles gets weaker. This enlargement has a side effect on the other beam (positrons), that grows due to the reduction of the beam-beam kick.

In the second study the crab-waist sextupoles of both rings were totally switched off from 200 a to 0 A. The resulting evolution of the beams sizes is shown in Fig. 3.23. In this case we can see the simultaneous resonance suppression in both lines.

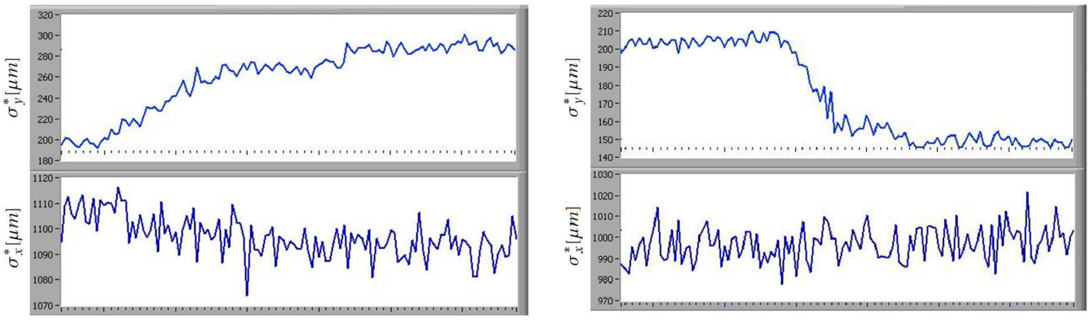

Figure 3.22: Beam size evolution in the first crab-waist experiment for electrons (left) and positrons (right). The vertical beam size increases for the line where the crab-waist sextupole strength is reduced, and decreases for the other one.

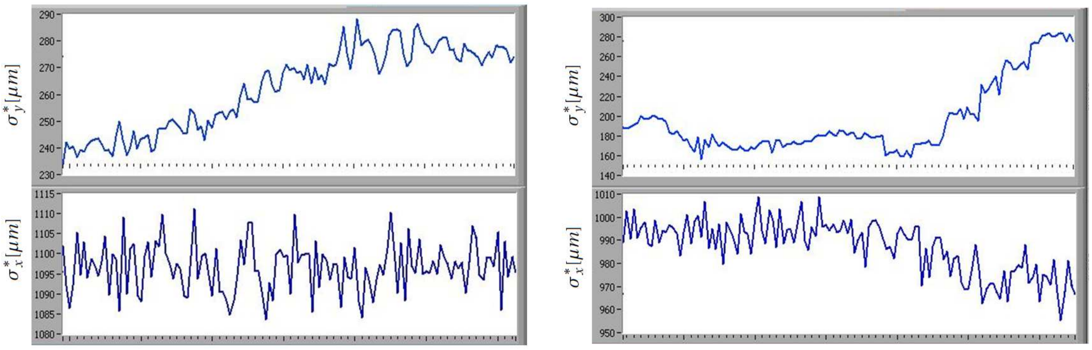

Figure 3.23: Beam size evolution in the second crab-waist experiment for for electrons (left) and positrons (right). The vertical beam size increases for both lines.

Figure 3.24 shows a readout of the DAΦNE experiment, KLOE-2 [60], during the second study. The monitors count the number of events detected except the lower on the right, that represents the luminosity. The three on the left are γ-monitors, and all of them show a reduction on the production of γ-particles, indicating less number of collision events.

The luminosity is lower when the crab-waist sextupoles are switched off and this period also corresponds to a maximum in the background.

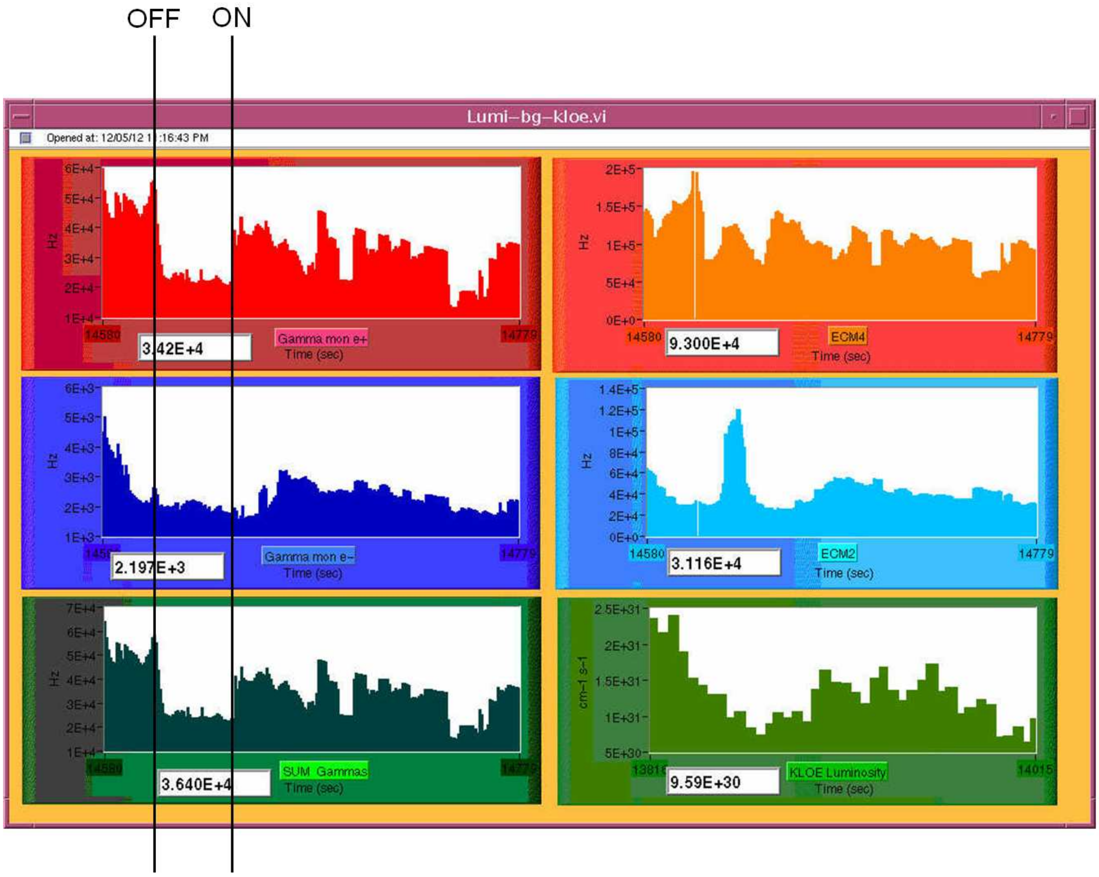

Figure 3.24: KLOE-2 luminosity readings during the second crab-waist experiment. During the time interval when the crab-waist sextupoles are switched off, the luminosity decreases and the background increases.

3.4.3 Crab-Waist Collisions in the LHC

The first proposal of having crab-waist collisions in the LHC was made by P. Raimondi in 2007 [61] and later then K. Ohmi looked more carefully into the possibility of a crab-waist scheme for the LHC [62].

A detailed study over the effectiveness of crab-waist collision scheme applied to LHC was performed in simulations [63]. In this work, frequency map analysis (FMA) [64] – a method that is widely used for exploring the dynamics of Hamiltonian systems – , was applied to study beam-beam effects in the crab-waist collision scheme. As expected, under the right conditions, the crab-waist focusing of colliding beams can result in a significant suppression of betatron coupling resonances induced by the beam-beam interaction. The FMA provides graphical information about all relevant resonances, their widths, and locations in the planes of betatron tunes and betatron amplitudes, so that resonance suppression due to the beam crabbing is clearly revealed. Figure 3.25 shows an example footprint with crab-waist sextupoles off and on, where the resonances are shown in red. As we can see, switching on the crab-waist sextupoles has two beneficial consequences: a smaller footprint area and a considerable reduction of the beam-beam resonance strength. The simulations also showed that the following condition

$$\sigma_x^*/\sigma_y^* > 10, \tag{3.16}$$

is needed so that the crab-waist would fully work.

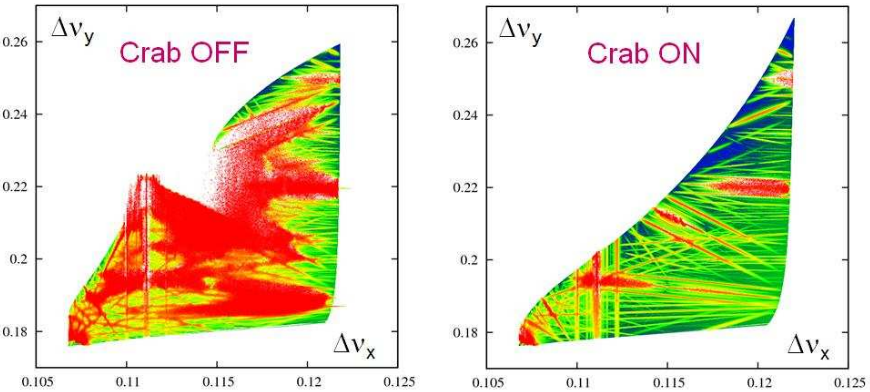

Figure 3.25: Resonance plot of the tunes, showing the resonance suppression (in red) by the effect of the crab-waist sextupoles. Courtesy of D. Shatilov *et al.* [63].

3.5 Conclusions

- Flat beams have the advantage of offering larger beam separations, that is, larger values of Δ_{in}, for the same crossing angle.
- A collision with large Piwinski angle reduces tune shifts (allowing higher bunch brightness) and the collision area (allowing lower β decrease in the non-crossing plane).
- In present LHC, an antisymmetric optics, $\beta_x^* \neq \beta_y^*$ implies four different optics functions, not allowing for the appropriate phase advances to install crab-waist sextupoles.
- Simulations show that for the LHC the beam lifetime increases but only for large values of the Piwinski angle. In an intermediate region the lifetime shrinks due to the effect of the excited resonances. In order to fully benchmark the results of the simulations, additional experimental studies must be conducted.

4. Towards a Very Flat Beam Optics with Large Crossing Angle for the LHC

This chapter approaches the problem of a new IR for the LHC, which would be able to perform crab-waist collisions with a large Piwinski angle. As we saw in the last chapter, a β^*-ratio of 100 is needed at least (flat beams), that implies the use of a symmetric IR optics and of a local chromatic correction scheme. Preliminary choices for the values of $\beta^*_{x,y}$, crossing angle and maximum β in the final elements are also included in the chapter, as well as a first concrete design with $\beta^*_x = 1.5$ m, $\beta^*_y = 1.5$ cm and a crossing angle of 4 mrad.

4.1 An LHC with Crab-Waist Collisions

The aim is to design a new symmetric interaction region with flat-beams, large crossing angle and to implement a local (or quasi-local) chromatic correction. The scheme will provide collisions in the large Piwinski angle regime. All the previous points allow for the implementation of crab-waist collisions. It is likely that the local chromatic correction and crab-waist sextupoles can be made to conspire, removing one of the main performance limitations of the LHC. From (1.77), the luminosity increases when the number of particles per bunch increases and when the emittance decreases, but the number of particles in the present LHC is limited by the beam-beam tune shift (1.106), which is proportional to the beam brightness.

The idea of the large Piwinski angle is to use large values of N/ϵ_N that would lead to tune shifts above the beam-beam limit under a normal Piwinski angle. Limitations for the number of particles per bunch are given by the electron cloud and by the transverse mode coupling. The minimum emittance is limited by the IBS growth rate. Table 4.1 presents the design parameters for the HL-LHC, which we take as a basis for further considerations [65].

Table 4.1: Limit parameters of the HL-LHC: Maximum particles per bunch, minimum emittance at injection energy and minimum emittance at collision energy, for two scenarios with bunch separation of 25 and 50 ns, respectively.

	N	$\epsilon_{N,inj}$	$\epsilon_{N,col}$
25 ns	2.2×10^{11}	2.0 μm	2.4 μm
50 ns	3.5×10^{11}	2.5 μm	3.0 μm

4.1.1 Beam-Beam Simulations with Frequency Map Analysis

The frequency map analysis was used to explore beam dynamics in the LHC. Figures 4.1 and 4.2 show the result of a tracking simulation for $\theta = 1.5$ mrad with LIFETRAC [66, 67]. Here tune-diffusion values are plotted in two different planes: in the plane of the betatron tunes, i.e. the so-called tune foot prints (Fig. 4.1) and the plane of normalized betatron amplitudes (Fig. 4.2). The color legend in the right side of the two figures represents the diffusion index, defined as $Log_{10}(\sigma_\nu)$, where σ_ν is the rms spread of the tunes. The two extremes correspond to stable motion (blue color) and stochasticity (red). Some resonances are visible in green color for the plots without the crab-waist sextupoles.

Both figures compare a situation where the crab-waist sextupoles are switched off with a situation where the sextupolar strength is at 50 % of their nominal value. The comparison between the two figures reveals two beneficial consequences of the use of the crab-waist collisions. One is the reduction of the beam-beam resonance strength, the other a smaller footprint area. By exploiting the crab sextupoles not only higher brightness beams are possible, but also one can expect a better beam-beam performance in terms of luminosity and beam lifetime.

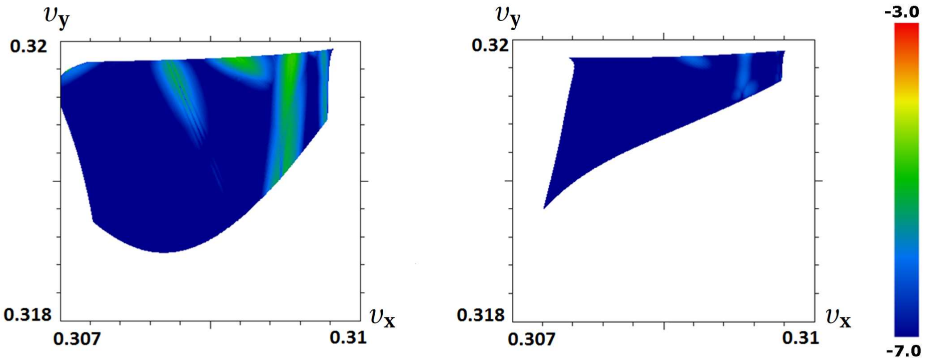

Figure 4.1: Resonance plot with $\beta_x^* = 1.5$ m, $\beta_y^* = 1.5$ cm and $\theta = 1.5$ mrad, showing the diffusion index in the betatron tune plane. Simulation with the crab-waist sextupoles switched off (left) and at 50 % of their nominal strength (right). Courtesy of Dr. Mikhail Zobov.

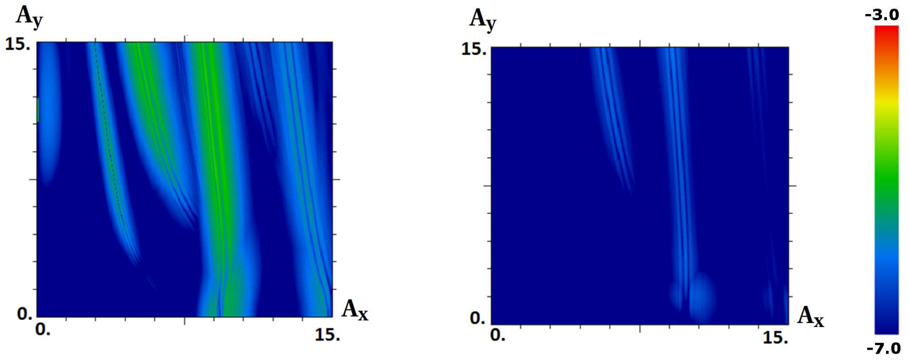

Figure 4.2: Resonance plot with $\beta_x^* = 1.5$ m, $\beta_y^* = 1.5$ cm and $\theta = 1.5$ mrad, showing the diffusion index in the plane of the normalized betatron amplitudes. Simulation with the crab-waist sextupoles switched off (left) and at 50 % of their nominal strength (right). Courtesy of Dr. Mikhail Zobov.

4.1.2 Design Considerations

There are several facts that hinder the implementation of crab-waist collisions in the LHC and make it more difficult, compared with DAΦNE:

- **Same charge of colliding particles:** in order to have an IR that is "symmetric Beam 1/ Beam 2" the focusing elements must have opposite sign for the two beams, including the first quadrupole where the two beams should be in a common aperture. The reason is that ($q\boldsymbol{v}$) has the opposite sign for the two beams.
- **Large L^*:** this generates high values of the β-functions in the final-focus, limiting the aperture and generating a large chromaticity.
- **Large energy:** in order to have the required large quadrupole strength, the gradients and the magnetic fields must also be very high. Superconducting technology is required.
- **Negligible radiation damping:** due to the long emittance damping times (longer than the machine run time), the beam distribution does not attain the equilibrium and the emittances remain round, that is, $\epsilon_x = \epsilon_y$. This makes it more difficult to have sufficiently flat beams at the interaction point. In addition, the emittance is not small enough. In order to obtain a high luminosity, the crossing angle cannot be as large as in DAΦNE.
- **Larger value of the crab-waist IP factor (3.12):** For DAΦNE, $k_{sl,IP} \approx 0.7{\cdot}10^3\ \mathrm{m}^{-1/2}\mathrm{rad}^{-1}$, while for the proposed IR $k_{sl,IP} \approx 20 \cdot 10^3\ \mathrm{m}^{-1/2}\mathrm{rad}^{-1}$, as we will see in Sec. 4.3.1.
- **Need for acceleration:** DAΦNE injects the particles in the main ring at the maximum energy (top up injection) and only one optics is needed. However, the LHC must have an additional optics compatible with the injection conditions, where the geometric emittance is larger, as pointed out in Sec. 2.2.3. Moreover a set of optics has to be designed for reducing the β-functions from the injection optics to the optimum value for collision, once the particles have reached the top energy. The sextupoles installed at the IP must be well placed to compensate the geometric aberrations and provide stability for all the squeeze process on the order of several minutes.

In response to these challenges, a new IR has been envisioned with the following components:

- **Large crossing angle:** This would reduce the long-range beam-beam effects, one of the main limitations of LHC operation.
- **Large Piwinski angle (LPA):** To allow higher brightness beams. The LPA also allows a significant β_y^* decrease by reducing the length of the overlapping area.
- **Flat beams:** To separate the horizontal and vertical β-functions allowing for a local chromatic correction. They also provide a better normalized separation.
- **Symmetric optics:** The small values of β_y^* considered for extremely flat beam collisions (a few cm) cannot be reached using a standard quadrupole magnet with the same field

gradient for both beams in a common aperture, as for the nominal LHC, since in that case β_y of one of the two beams (or on one side of the IP) would become so large as to render chromatic correction impossible using the available sextupole strengths.

- **Chromatic correction in the IR:** To allow for low values of β_y^* and to increase the dynamic aperture.
- **Crab-waist collisions:** To suppress the X-Y resonances excited by the beam-beam interaction, potentially allowing for higher tune shifts and increased dynamic aperture.

4.1.3 Advantages of a Large Piwinski Angle

The large Piwinski angle allows for a large number of particles due to the lower value of the tune shift. It is clear, from (1.77), that an increase in N yields more instantaneous luminosity. But there is another contribution from a larger number of particles than that over the initial luminosity, L_0. In fact, from (1.80), more particles per bunch corresponds to a longer burn-off lifetime for the same initial luminosity and consequently to a longer total luminosity lifetime: τ_T. In order to evaluate the potential benefit for the integrated luminosity, we have considered two scenarios. Both of them have the same value for L_0, but one has $N_{T,A,0}$ particles per beam and the other, $N_{T,B,0}$, assuming $N_{T,A,0} < N_{T,B,0}$. The time constant in the first case is $\tau_{T,A}$ and in the second, $\tau_{T,B}$, leading to two different evolutions for the integrated luminosity (See 1.82), $L_{int,A}$ and $L_{int,B}$, being $L_{int,A} < L_{int,B}$ during all the machine run.

This shows that the increase on the number of particles is an essential element to have a high integrated luminosity. But the most important thing is that the large Piwinski angle reduces the length of the overlapping area, and this makes profitable an additional reduction on β_y^* for values below σ_s without incurring an excessive hourglass effect. In fact, combining (1.78) and (1.87) we get: $l_{OA} = \sigma_s/\phi$.

4.1.4 Approach to the Problem

A preliminary LHC IR with the elements listed in Sec. 4.1.2 is considered. First of all, the final triplet with common aperture for the two beams are replaced by a set of four lenses, three of which are normal quadrupoles with separate aperture, in order to provide the optical symmetry between the two beams. That means that their gradients must have opposite sign for the two beams, unlike for the present LHC magnets in IRs and arcs, where the focusing gradients have the same sign for both beams.

According to the beam-beam simulations, a beam size aspect ratio of 10 is needed for the crab-waist collisions to be effective (3.16). A factor of 5 might also work, but we have decided to keep the factor of 10. From (1.83) it translates into a ratio β_x^*/β_y^* =100, assuming $\epsilon_x = \epsilon_y$. Sec. 4.5.4 will address how considering unequal emittances in the two planes ($\epsilon_x \neq \epsilon_y$) can make the design more feasible.

Figure 4.3 shows the new IR. The crossing angle is made by the reference orbit while for the nominal LHC (Fig. 2.2) the crossing of the two reference orbits is under a zero angle, the

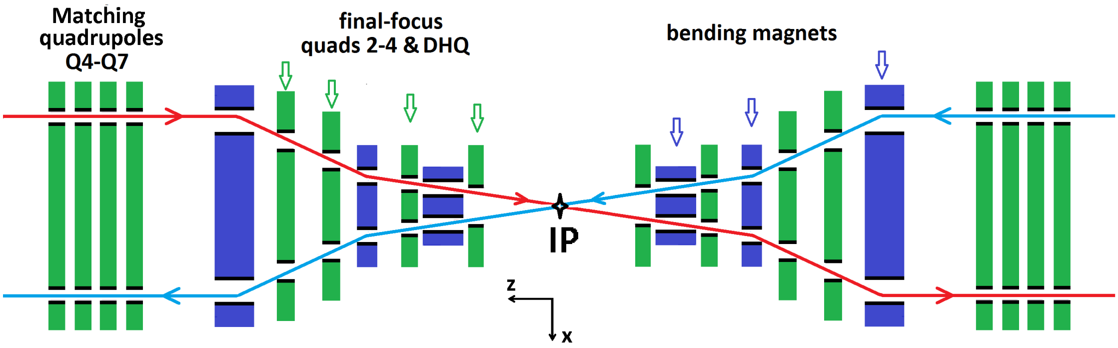

Figure 4.3: Separation scheme for the proposed IR. The bending magnets are interleaved with the quadrupoles.

crossing angle being introduced by superimposed orbit bumps.

A new element, the double-half quadrupole (DHQ) is proposed in order to:

- **Provide focusing for both beams:** Keeping the free length from the IP to the entrance face of the first quadrupole, L^*, equal to its present value of about 23 m, the beam separation at this location is not large enough for installing two regular superconducting quadrupoles of opposite polarity.

- **Ensure sufficient aperture for flat beams:** When fully separating the beams (by means of a dipole first or with a larger crossing angle) the radius of the circular aperture to host the beam ellipses would be enormous, thus demanding a very high magnetic field. A DHQ of squared aperture is the most elegant geometrical solution to host two identical elliptical beams with $\sigma_y >> \sigma_x$ and with horizontal separation, as we will see.

With this configuration, the crossing is established in the horizontal plane for IP1 & IP5, instead of the alternating crossing scheme in the present LHC. As a result, there is no compensation for the pacman effect. However, the increased beam separation should make this effect negligible.

The following choices have been made:

- **Keep the emittance ratio:** As for present LHC, we considered that we have the same emittance in the two planes, $\epsilon_x/\epsilon_y = 1$.

- **Keep the free length, L^*:** A smaller distance between IP and the first element could help, as much smaller values of β could then be possible in the final-focus, reducing aperture requirements, decreasing chromaticity and easing matching. If a DHQ first option is preferred, a smaller L^* would require a bigger crossing angle to get the required gradient in the DHQ. If a dipole first option were chosen, we could have the same separation or even more with a smaller crossing angle.

- **Keep the longitudinal beam size:** as for nominal HL-LHC, $\sigma_s = 7.5$ cm.

- **Keep the hardware changes to the minimum:** therefore, the use of crab cavities is discarded.

It was also decided, in principle, to choose $\beta_x^* \beta_y^* = (15\ \text{cm})^2$, as for ATS optics without crab-cavities. This product together with the β-ratio of 100 yields the optical functions at the IP, $\beta_x^* = 1.5$ m and $\beta_y^* = 1.5$ cm.

4.2 The Double-Half Quadrupole Design

The reason for the name is that it consists of two half quadrupoles of different sign. Figure 4.4 shows the first design of the DHQ. This was inspired by the LHeC “half quadrupole” design [68]. In that case, the half quadrupole serves as a lens for one of the beams, while the other is passing by a field-free region. This first design shows the viability of producing opposite gradient field in the common aperture. However, the circular shape is not the most appropriate for flat beams, since the gradients and aperture radius are very limited with this geometry.

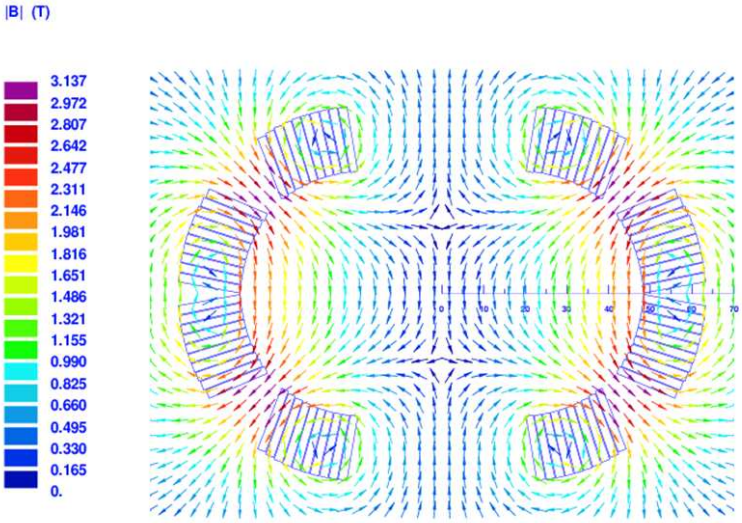

Figure 4.4: Preliminary design of the double-half quadrupole, showing the magnetic field lines. It is made of two halves of 28 mm radius with a separation of 40 mm. Courtesy of Dr. Stephan Russenschuck.

Choosing a rectangular aperture (which would not be possible with a pure sextupole geometry), allows accommodating two side-by side beam pipes of elliptic dimensions. For small gradients and apertures, a half-quadrupole can be constructed with a mirror-plate from soft-magnetic steel. This type of magnet was installed in the IRs of the HERA *ep* (electron-proton) collider [69] and of the KEK B-factory [70]. However, the required gradient in the double-half quadrupole makes it necessary to apply superconductor technology for the coils, and would also result in a complete saturation of the mirror-plate. Therefore, we have developed a combined function magnet consisting of eight racetrack coils that produce a combined dipole and sextupole field in the common aperture; see Fig. 4.5.

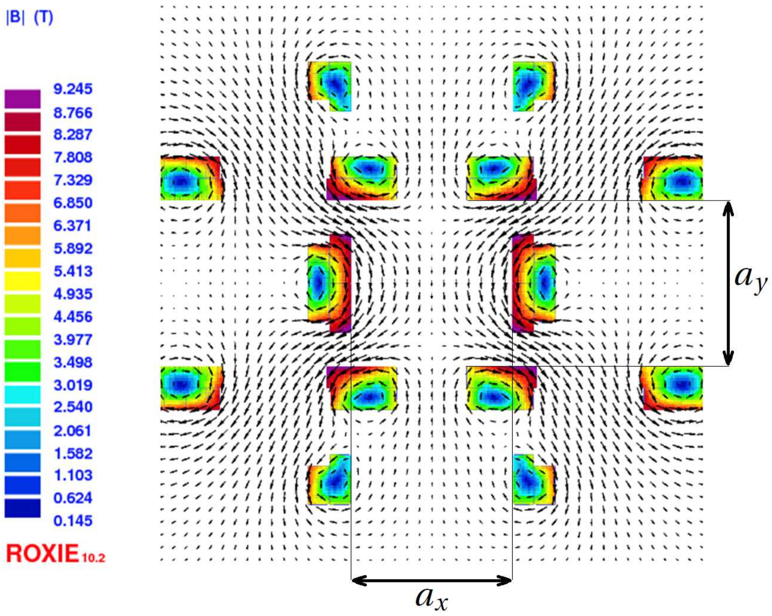

Figure 4.5: Cross section of the DHQ, showing the magnetic field lines. The color legend is indicated on the left side and represents the magnetic field in the coil. The dimensions of the central window are $a_x = a_y = 120$ mm.

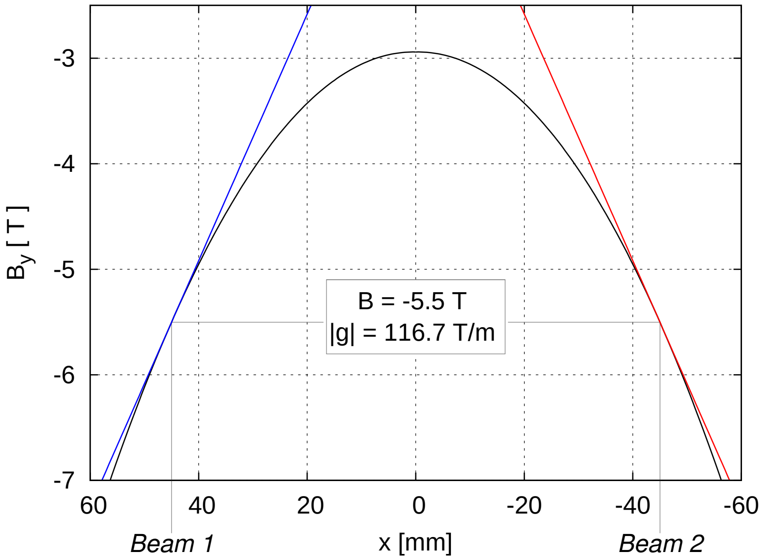

Figure 4.6: Vertical magnetic field distribution along the horizontal axis for the DHQ at the right side of the IP ($s > 0$), computed by ROXIE. The red and blue lines represent the tangent lines in the center of the beams ($x = \pm 45$ mm), whose slope gives the quadrupolar strength for each beam.

The use of LHC inner and outer layer Nb-Ti cable has been assumed, operated at 80 % on the load-line. The peak field in the coil is 8.14 T for an aperture square of 160 mm, and the gradient at the center of either beam (45 mm from the origin) is 116.7 T/m, with an additional dipole field component of 5.5 T. Analytical solutions are available for producing field configurations with two beams of minimum separation by the optimized placement of individual superconducting wires [71]. The simple (non-optimum) racetrack shape chosen for the coils of Fig. 4.5 will facilitate the use of Nb_3Sn technology if required. The field distribution of the DHQ is shown in Fig. 4.6. Since the design orbits of the two beams are separated by 90 mm, the feed-down from the strong sextupole produces the desired strong quadrupole component. The design of this magnet has been realized with ROXIE software [72]. The gradient has different signs for the two beams, but due to the opposite sign of $(q\boldsymbol{v})$ for Beam 2, the beam is vertically focusing ($k > 0$) for the two beams. For the same reason, the sextupolar component, which is negative for Beam 1, changes its sign for Beam 2.

When the DHQ is reversely powered, the sign of all the field components is changed. A DHQ at the other side of the IP should have opposite polarity in order to be also vertical focalizing, as the beams interchange horizontal positions in the DHQ before and after the IP. All the other components are thus inverted. The element is vertically focusing for the two beams, while the dipole field inverts its sign. With regard to the sextupolar component, it is now positive for Beam 1 and negative for Beam 2. The corresponding field distribution for the DHQ installed on the left side of the IP is shown in Fig. 4.7.

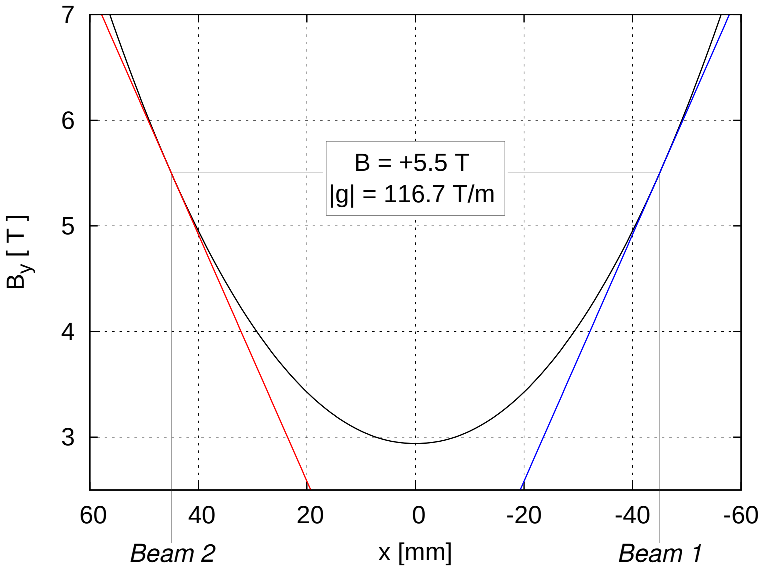

Figure 4.7: Vertical magnetic field distribution along the horizontal axis for the DHQ at the left side of the IP ($s < 0$), computed by ROXIE.

4.2.1 Beams in the DHQ

It is very important to define the operating point, i.e., the location on the magnet where the beams will pass. This is related with the crossing angle as

$$\theta = \frac{\Delta_{beam}}{L^*}. \tag{4.1}$$

Figure 4.8 shows a sketch of the cross section of the beams in the DHQ, represented as ellipses of dimensions $(11\sigma_x, 11\sigma_y)$ = (8.4 mm, 43.6 mm). The relative position of the beams in the aperture corresponds to the entrance of the DHQ ($s = L^* = 23$ m), while the beam sizes σ_x and σ_y correspond to the maximum values attained in the DHQ, here with a normalized emittance of $\epsilon_N = 2.4$ μm. A beam with $\epsilon_N = 2.4$ μm would show less aperture, but would still fit in the aperture as the dimensions would be $(11\sigma_x, 11\sigma_y)$ = (10.5 mm, 54.5 mm). A crossing angle of 4 mrad separates the beams in the optimum way so as to fit into the square window. The right picture illustrates Eq. (4.1).

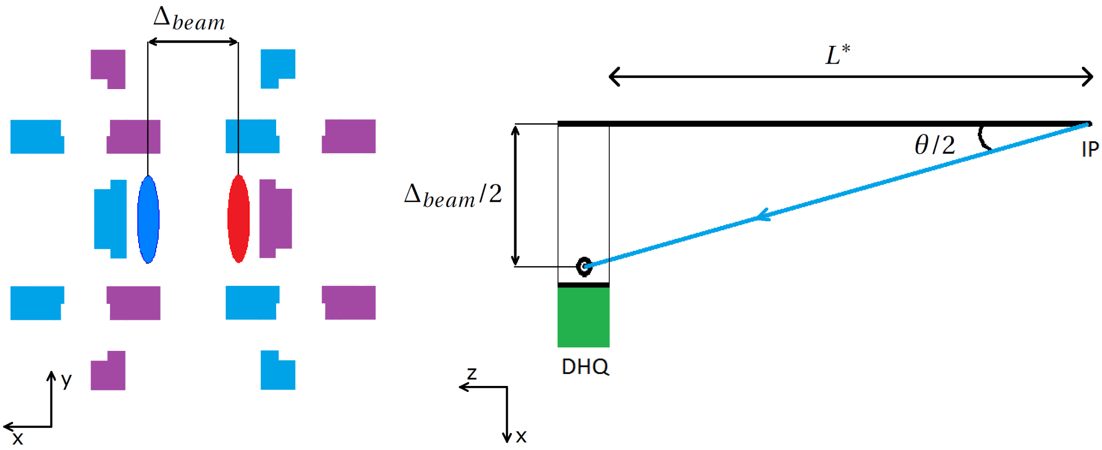

Figure 4.8: Cross section of the two beams in the DHQ represented as a 11-σ ellipse for Beam 1 and Beam 2 (left). The color of the blocks represents the direction of the current, following the same color code as in Fig. 1.3. Geometric relation between the beam separation at the beginning of the DHQ and the crossing angle (right).

4.2.2 Multipolar Analysis

The components of the magnetic field can be expanded as

$$B_y(x,y) + iB_x(x,y) = \sum_{n=0} (B_{n+1} + iA_{n+1}) \left(\frac{x+iy}{r_0}\right)^n. \tag{4.2}$$

For the upright components, those considered in this thesis work, $A_{n+1} = 0$, while the multipolar components are defined as [72, Sec. 6.1.1.1]

$$B_{n+1} = \frac{r_0^n}{n!}\frac{\partial^n B_y}{\partial x^n}, \tag{4.3}$$

where r_0 is a reference radius. For the LHC magnets, $r_0 = 17$ mm. The first four multipolar components are related with the normalized field components (See 1.13) as

$$B_1 = B_y, \qquad B_2 = g r_0, \qquad B_3 = g_s \frac{r_0^2}{2}, \qquad B_4 = g_0 \frac{r_0^3}{3!}. \tag{4.4}$$

Figure 4.9 presents the absolute value of multipolar components normalized to B_2 (which represents quadrupole field at the position of the design orbit in the DHQ), and for a reference radius $r_0 = 17$ mm. Component B_1 gives the dipolar term, $|B| = 5.5$ T. It is a considerable value, taking into account that the LHC superconducting bending dipoles have a nominal field of 8.3 T. The component B_3 is also very high, it translates into a $|k_s| \approx 0.12\ \mathrm{m}^{-3}$. For a comparison, the LHC sextupole magnets that correct chromaticity in the arcs have $|k_s| \approx 0.17\ \mathrm{m}^{-3}$. This sextupolar component of the DHQ can be used to correct the chromatic aberrations in the IR by setting the dispersion to an appropriate value.

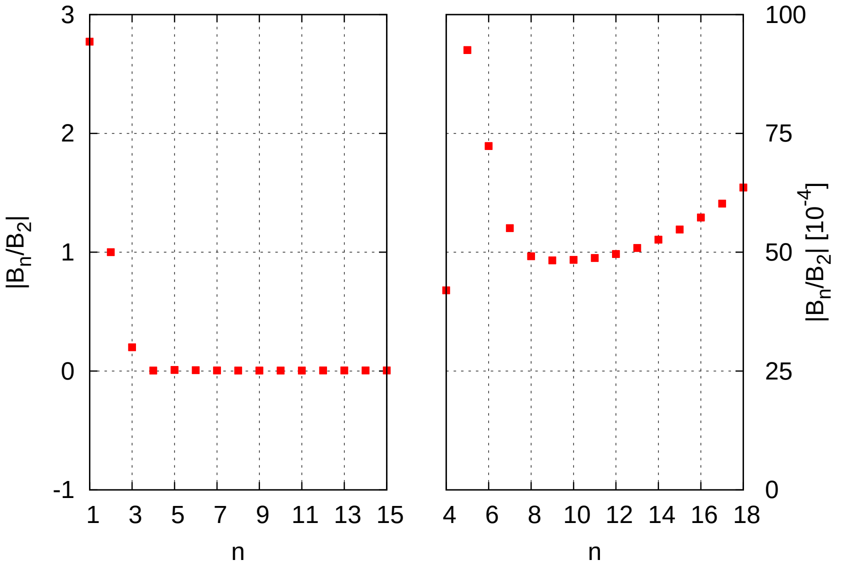

Figure 4.9: Absolute value of the DHQ multipolar components normalized to B_2 for n=[0,15] (left) and for n=[4,18] (right), for a reference radius $r_0 = 17$ mm.

4.2.3 Segmentation of the DHQ

The beams enter the DHQ at a certain angle with respect to the central axis, and this angle is equal to half of the crossing angle, that in this case is $\theta/2 = 2$ mrad. For a long element (in the proposed design it has a length of 14 m), the separation of the beams would intolerably increase. Each beam would move ~ $(2 \cdot 14\ \text{m})\cdot(2\ \text{mrad}) = 56$ mm, out of the central axis, only by the effect of the initial angle. The effect of the dipolar field term will also further increase the beam separation, but a large change in the separation may result in the beams no longer fitting inside the available aperture window or reduce the effective gradient. For these reasons the DHQ element should ideally be built in segments, as illustrated in Fig. 4.10, all of them powered with the same current.

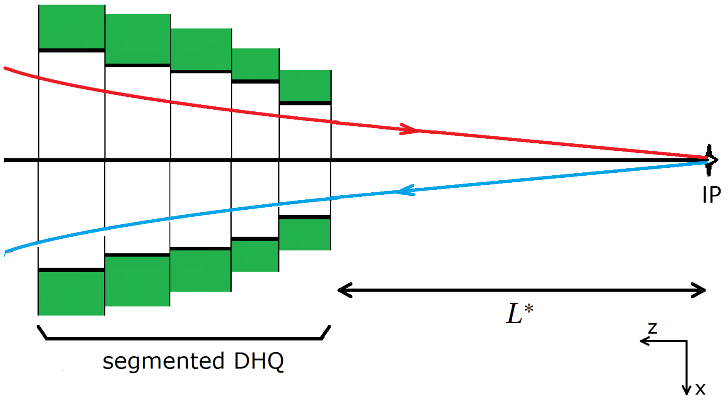

Figure 4.10: Reference orbit of the two beams in a segmented DHQ. The horizontal aperture (a_x) of the successive sections increases as the beam trajectories separate.

4.2.4 Magnetic Properties

The properties of the quadrupole and sextupole fields are very well known. Their analytical characterization is easy. Considering a circular aperture with radius r_0, from (1.30) and (1.31) we can deduce that the peak magnetic field of a quadrupole $B_p = g r_0$ grows by the same factor as the radius. For a sextupole, from (1.38) and (1.39), the peak field $B_p = \frac{1}{2} g_s r_0^2$ grows with the second power of the radius. Using this information, we can see how the gradient changes by varying the aperture and keeping the maximum peak field constant. But as we do not have a simple analytical formulation of the DHQ, we can only determine its properties by modelling different DHQs with different apertures. As we saw in Sec. 4.2.3, the DHQ should be built in the form of segments, and we should know how the quadrupole strength varies when the aperture is modified but the current is the same.

In a related study the beam offset, i.e., the distance from the center of the DHQ to the center of the beam, $\Delta_{beam}/2$, was shifted by Δx_B together with the horizontal dimension of the aperture of the DHQ ($a_x \to a_x + 2\Delta x_B$), keeping the vertical aperture constant (Fig. 4.11).

On the one hand, an offset variation like Δx_B should produce an absolute value gradient increase, as we can see intuitively in Fig. 4.6, but on the other hand the aperture increase causes

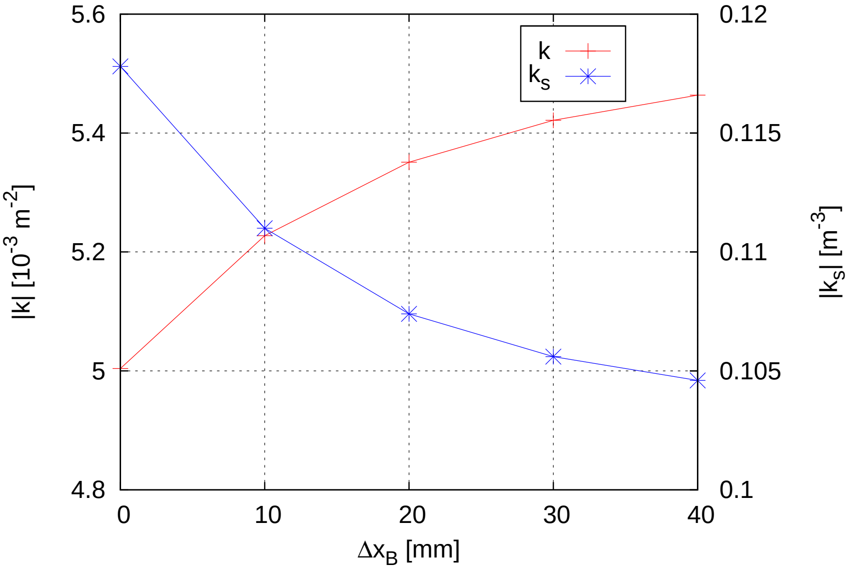

Figure 4.11: DHQ quadrupolar and sextupolar components with a beam offset of $\Delta_{beam}/2+\Delta x_B$ and a horizontal aperture of $a_x + 2\Delta x_B$.

a field reduction. The overall effect is that the absolute value of the quadrupolar component slightly increases. On the other hand the sextupolar component decreases.

4.2.5 Comparison with a Sextupole

The field shown in Fig. 4.6 resembles the field of a sextupole with an additional dipolar component. As the dipolar component is in principle not necessary (but it helps for the beam separation), we study in this section if the same performance could be achieved by a pure sextupole. In order to have at least the same aperture as in the DHQ, we consider the radius of the sextupole a factor $\sqrt{2}$ larger than the half aperture of the magnet, that corresponds to the circumscribed circle (r_s = 85 mm). This would have an important advantage, since all the multipole terms of order higher than 2 in the first quadrupole (Fig. 4.9) would be zero (with the exception of errors), as the sextupole is a pure element. A similar shape of the field is achieved with $g_s = -2.2\ \text{kT/m}^2$. At $x = \pm 45$ mm, the gradient is $|g| = -100$ T/m. As no dipolar component is considered, the maximum field is $B_p = \frac{1}{2} g_s r_s^2 = 8$ T.

Figure 4.12 shows a quadrant of the DHQ. A sextupole as an inscribed circle would cause an aperture reduction. The same aperture is guaranteed for the circumscribed sextupole.

In order to get the same gradient at the same position, g_s should be $-2.6\ \text{kT/m}^2$, and this implies a maximum magnetic field of 9.4 T. For this magnetic field, NbTi technology would not be possible, and the sextupole should be built in Nb_3Sn. Instead of choosing the aperture of the magnet as the circumscribed circle of the DHQ, it could be 72 mm, reducing the aperture in terms of σ but more drastically reducing B_p due to its quadratic dependence. In that case we would have 5.8 T and 6.7 T for $|g| = 100$ T/m and $|g| = 117$ T/m, respectively.

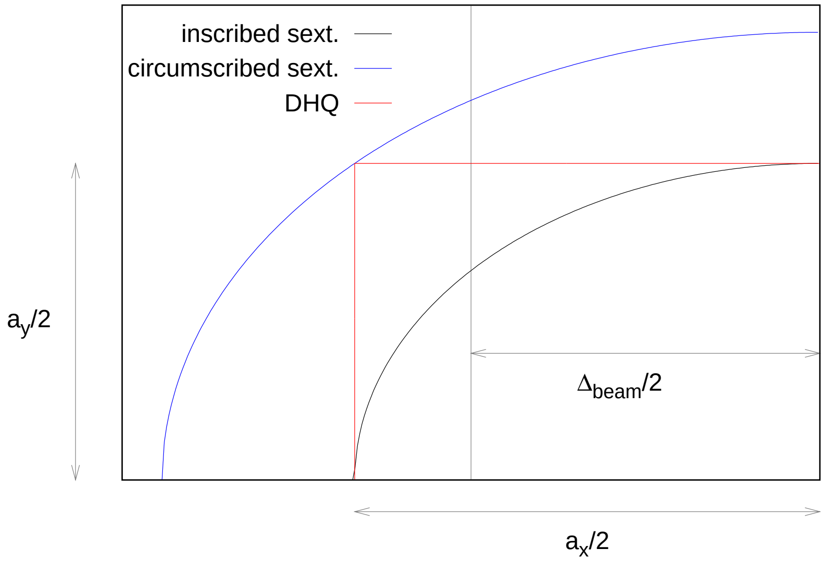

Figure 4.12: Comparison of the apertures given by the DHQ, a sextupole as an inscribed circle and as a circumscribed. For $a_x = a_y$, the same aperture is guaranteed with a sextupole of aperture radius $r_s = a_x/\sqrt{2}$.

4.3 First Interaction Region Design

4.3.1 Optics

The proposed optics is presented in Fig. 4.13 for Beam 1. It is a symmetric left/right optics in the range [−260 m, 260 m], as it fulfills relations (2.3) and (2.4). The DHQ studied in the previous section appears as the first element from the IP. The different β^* in the two planes induce a difference in divergence, that separates the functions in the two planes. The IR optics has been fully matched to the LHC ring optics in terms of β-functions and dispersion. There are 5 peaks of the betatron functions: three of β_y and two of β_x. They make it possible to install sextupoles to locally correct the chromaticity (the first four) and to allow for crab-waist collisions (cw-sext). Figure 4.14 shows the optics for Beam 2. A comparison with the optics of Beam 1, reveals the optics as symmetric Beam 1/Beam 2, fulfilling Eqs. (2.1) and (2.2). The DHQ is represented in the upper plot of Figs. 4.13 and 4.14 as a filled red box. Its height represents the quadrupolar strength relative to the other quadrupoles. In this model, the DHQ is represented as an element of homogeneous strength, ignoring for the moment the scheme of Fig. 4.10. Anyway, the changes arising from considering the DHQ as a succession of elements of different strength would be small, as far as the effects on the global optics are concerned.

Unlike the usual IR optics, as for present LHC, the slope of the dispersion at the IP is non-zero, $D_x'^* \neq 0$. The reason for that is the need for dispersion in the IR so that the sextupoles can correct the chromaticity, a requisite of the local chromatic correction scheme. Henceforth a dispersion suppressor is no longer necessary, even though it could help in the dispersion matching, as we will see in Sec. 4.4. However, the magnets of the matching section are not

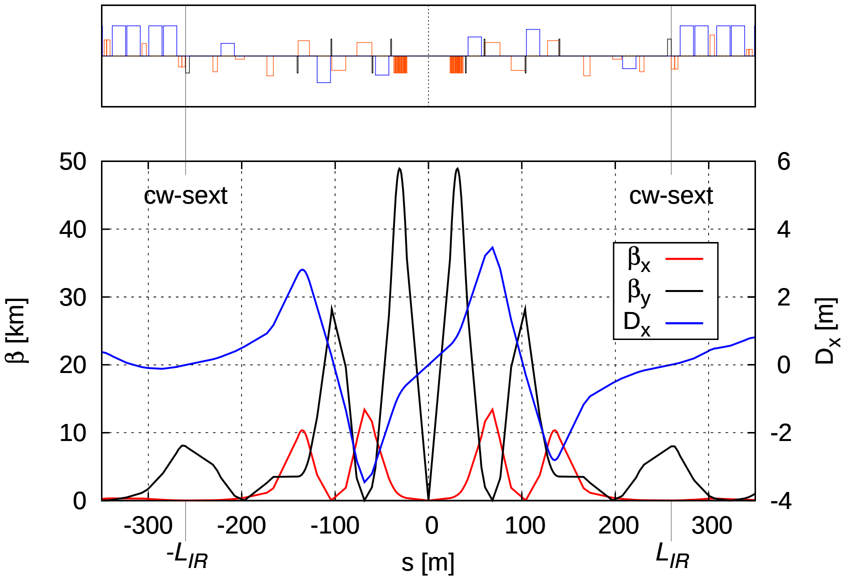

Figure 4.13: New LHC IR1 & IR5 optics for Beam 1, with $\beta_x^*/\beta_y^* = 1.5$ m/1.5 cm, with the sextupoles at their potential locations and with their respective sign. The DHQ is represented as a filled red box. The optics is symmetric left/right.

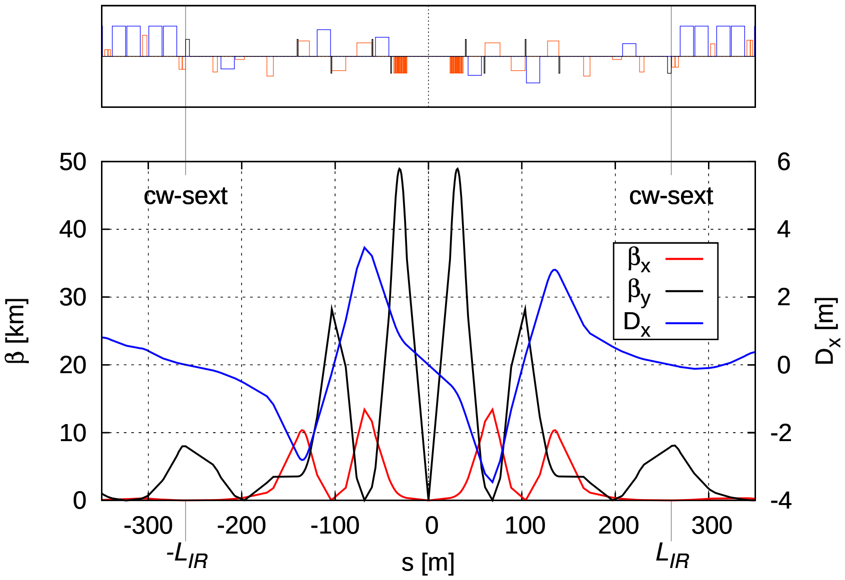

Figure 4.14: New LHC IR1 & IR5 optics for Beam 2, with $\beta_x^*/\beta_y^* = 1.5$ m/1.5 cm. The DHQ is represented as a filled red box. The optics is symmetric Beam 1/Beam 2.

sufficient for the betatron matching and the dispersion suppressor magnets are used for this purpose. Then, the matching is done with the 6 variables together, $(\beta_x, \beta_y, \alpha_x, \alpha_y, D_x, D'_x)$, instead of modularly.

The sextupolar component of the DHQ can help correcting the chromaticity if the dispersion is properly adjusted, and the contribution would have the same sign in the four cases: for both beams and on both sides of the IP. This is done by selecting $D'^*_x > 0$ for Beam 1 and $D'^*_x < 0$ for Beam 2. Then, either the chromatic correction relies on the DHQ or an additional sextupole is added, but with the two contributions acting in parallel instead of one fighting against the other.

Table 4.2 summarizes the parameters of this new optics. The value for β^*_y is particularly small, the lowest ever proposed for the LHC, but still above the length of the overlapping area, l_{OA}. Remarkable as well is the crab-waist IP factor, $k_{sl,IP}$. Compared to that of DAΦNE (Table 3.3), it is one order of magnitude larger, which makes it essential to reduce the other factors that influence on the integrated sextupolar strength, so that it can be feasible. From (3.11), k_{sl} can be minimized by maximizing $\beta_{x,cs}$ and $\beta_{y,cs}$. Due to the phase advance conditions, it is not possible to get a high value of $\beta_{x,cs}$. This is why cw-sext is located in a peak of the vertical β-function.

Table 4.2: Parameters for the proposed LHC optics.

$\beta^*_{x,y}$	1.5 m, 1.5 cm
$\beta_{MAX;x,y}$	14 km, 49 km
θ	4.0 mrad
D'^*_x	± 0.025
ϵ_N	2.4–3.75 μm
σ^*_x	22.0–27.5 μm
σ^*_y	2.2–2.7 μm
σ_s	7.5 cm
ϕ	5.4–6.8 rad
l_{OA}	1.1–1.4 cm
Δ_{beam}	90 mm
Δ_{in}	268–216 σ_x
$k_{sl,IP}$	20.4×10^3 m$^{-1/2}$ rad^{-1}

Table 4.3 presents the parameters of the new quadrupoles that would be introduced, between the DHQ and Q4. Following the focalizing elements, DHQ and the quadrupoles quad.2, quad.3 and quad.4 substitute the present LHC triplet (Q1, Q2, Q3). They are built as long magnets, but have the advantage that due to their low maximum magnetic field in the coil, they can be built as normal conducting twin quadrupoles. This was a design constraint in order to obtain some further advantage in this design. The focusing elements, unlike present LHC quadrupole magnets, must have a distribution of the magnetic field of opposite sign for

both beams, i.e.,

$$(B_x^1(x,y), B_y^1(x,y)) = (-B_x^2(x,y), -B_y^2(x,y)), \tag{4.5}$$

in order to provide the required symmetry Beam 1/ Beam 2.

Table 4.3: Parameters of the final-focus double aperture quadrupoles: gradient, magnetic length, aperture radius, maximum magnetic field in the coil and integrated quadrupole strength. The radius is computed as 11max(σ_x, σ_y)+5 mm, with $\epsilon_N = 2.4\ \mu m$, and the maximum magnetic field in the coil as $|B_p| = gr$.

	g [T/m]	L_q [m]	r [mm]	$\lvert B_p \rvert$ [T]	$k_l[10^{-3}\mathrm{m}^{-1}]$
quad.2	93.4	16	28	2.6	64.0
quad.3	−98.9	15	38	2.8	−63.5
quad.4	105.8	12	25	3.0	54.4

4.3.2 Beam Separation and Geometry

Figure 4.15 shows the reference orbit of both beams in the IR. The bending magnets were matched to bring the orbits from $|X| = 97$ mm, $|X'| = 0$ in the arc to $|X| = 0$, $|X'| = 2$ mrad at the IP. The DHQ is represented as a filled blue box in the upper plot, with its height representing the dipolar strength relative to that of the separator magnets. The dipolar strength is the dipolar component of the field divided by the rigidity, $k_0 = qB_y/p$. In the four cases (for both beams and at both sides of the IP), the dipolar component of the DHQ tends to bend the trajectories from the IP out. The relation between angles is then given by the relation between the areas. The signs of the dipole strength refer to Beam 1; for Beam 2 the signs are reversed. The total angle bent by the DHQ is approximately 3.4 mrad, of the same order as but smaller than that of an arc dipole, 5.1 mrad. The length of the other three separator magnets (sepd.1, sepd.2, sepd.3) has been made equal to the length of the arc dipoles: 14.3 m. The respective values for the magnetic field in the three separator magnets are $|B(\text{sepd.1})| = 5.3$ T, $|B(\text{sepd.3})| = 7.4$ T and $|B(\text{sepd.3})| = 3.5$ T. Those values can be achieved by superconducting magnets only, and in principle the use of NbTi technology seems to be sufficient. This implies having the same field in the two apertures, that is the opposite situation to that of the arc bending magnets. Regarding the present LHC IR, the separation magnets D1 and D2 also present for both beams an identical field distribution. D1 is built as a series of 6 magnets, all of them presenting a common aperture for both beams, while D2 is a twin-aperture magnet. The reference orbit of the two beams in this separation dipole (and, by extension, in all the IR from D2 left to D2 right) follows:

$$(X^1(s), Y^1(s), Z^1(s)) = (-X^2(s), Y^2(s), Z^2(s)). \tag{4.6}$$

From the point of view of the mechanical design it is very complicated to build parallel magnets with the geometry defined by (4.6), and for this reason a straight magnet is always preferred. In order to evaluate the need for the type of geometry, we denote the maximum shift of the orbit within the magnet, as

$$\Delta X_{MAX} = |X_{MAX} - X_{MIN}|, \tag{4.7}$$

where X_{MAX} and X_{MIN} represent the maximum and minimum values, respectively, of the horizontal coordinate of the reference orbit. In the case of D2, ΔX_{MAX} is only 10 mm. This is a small deviation compared with its aperture radius, which has a value of 40 mm, thus being possible building this bending magnet straight, with the two apertures in parallel. In principle, sepd.2, with ΔX_{MAX} = 9 mm, can be straight but sepd1.1 should be fabricated either as a segmented straight or with a sagitta, with the central axis of the pipes following Eq. (4.6). This is because its maximum orbit shift is 57 mm. The case for sepd.3 seems to be possible as straight, as it has ΔX_{MAX} = 15 mm, but this should be explored carefully.

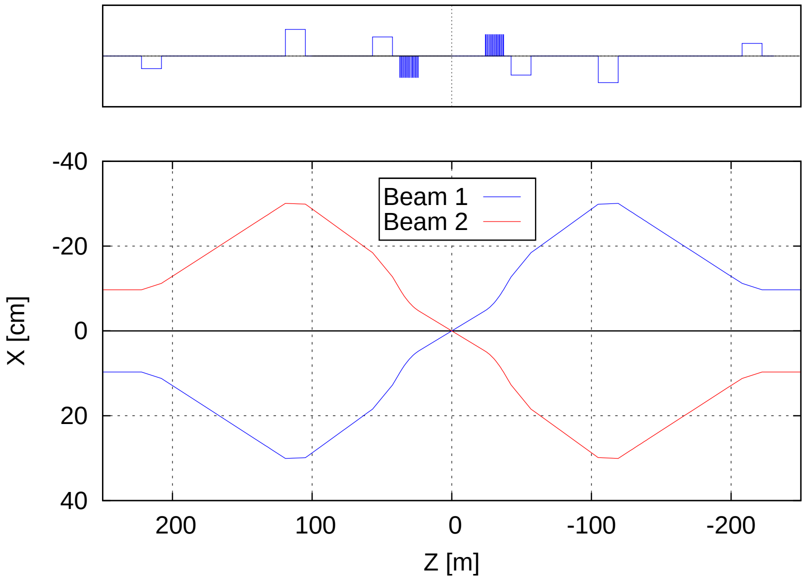

Figure 4.15: Interaction region crossing scheme, showing the reference orbits of the two beams. The upper plot represents for Beam 1 the dipolar strength of the dipoles and of the DHQ. This element is represented as a filled blue box.

4.3.3 Sextupole Arrangement

The phase advances from the IP of all the sextupoles are presented in Table 4.4. Their position allows that sextupoles sext.1 and sext.3 correct chromaticity in the vertical plane while sext.2 and sext.4 do so in the horizontal. The last one, cw-sext, is the crab-waist sextupole and it complies with the requirements for the phase advance (3.5). The values of the β-functions in this sextupole are $\beta_x \approx 20$ m and $\beta_y \approx 8$ km. The large β_y helps to reduce the integrated sextupole strength (3.10), but its absolute value is considerably high: $|k_{sl5}| \approx 0.6$ m^{-2}. For a length of 1 m, the sextupole strength would be 3.5 times that of the LHC arc sextupoles, corresponding to a maximum magnetic field $B_p = 11.2$ T for an aperture of 40 mm. In order

Table 4.4: Approximate phase advances from the IP to each of the sextupoles, β-functions and dispersion in the sextupoles. The dispersion values represent the case for Beam 1 right and Beam 2 left; for the other two sextupoles, the signs of dispersion are inverted.

	$\Delta\mu_x$ [rad]	$\Delta\mu_y$ [rad]	β_x [m]	β_y [m]	D_x [m]
sext.1	$\pi/2$	$\pi/2$	2.68×10^3	31.6×10^3	1.54
sext.2	$\pi/2$	$\pi/2$	11.6×10^3	2.00×10^3	3.21
sext.3	$3\pi/2$	$3\pi/2$	165	27.0×10^3	-0.32
sext.4	$3\pi/2$	$3\pi/2$	9.05×10^3	3.54×10^3	-2.62
cw-sext	2π	$5\pi/2$	19.0	8.00×10^3	3.31×10^{-3}

to be able to build the crab-waist sextupole with a reasonable k_s, the length should be large. However, a large element has the drawback that the phase advances vary along its length, introduces aberrations and may have an impact on the performance of the crab-waist collision scheme. A compromise was found and the phase advance between the entrance and the exit of cw-sext was chosen to be 0.07 π rad, for a length of 4 m. Then, the maximum magnetic field would be 2.8 T for a radius of 40 mm, and this can be built as a normal-conducting element.

A total of four crab-waist sextupoles should be installed in the IR to implement the crab-waist collisions, a pair of sextupoles per beam. The required signs for each of the sextupoles are shown in Table 4.5.

If the dispersion in the crab-waist sextupole is not zero, some chromaticity is generated. The contribution of the crab-waist sextupoles to the chromaticities in the two planes is obtained as (1.94) and (1.95), limiting the integrating path to the length of the sextupoles. The contributions for each IP side are:

$$Q'_x \approx \frac{1}{4\pi}\beta_{x,cs}k_{sl5}D_{x,cs} = \frac{1}{4\pi}D_{x,cs}\frac{\sqrt{\beta_{x,cs}}}{\beta_{y,cs}}k_{sl,IP}, \tag{4.8}$$

$$Q'_y \approx -\frac{1}{4\pi}\beta_{y,cs}k_{sl5}D_{x,cs} = -\frac{1}{4\pi}D_{x,cs}\frac{1}{\sqrt{\beta_{x,cs}}}k_{sl,IP}. \tag{4.9}$$

Here the crab-waist IP factor, $k_{sl,IP}$, has been introduced as (3.11). The contribution to the horizontal chromaticity is negligible, due to the low values of $\beta_{x,cs}$ resulting from the phase advance condition. However, the contribution of the vertical chromaticity may be very high. This is why it is so important to define the sign of the dispersion suitably, in order not to fight with, but to enhance the chromatic correction. In case we want cw-sext to assist in correcting chromaticity, the requirement for its dispersion, $D_{x,cs}$ is that it must have opposite sign to k_{sl5}. Table 4.5 shows the requirements on dispersion at the crab-waist sextupoles to have a positive contribution to chromaticity. Both the right side of the IP for Beam 1 and the left side for Beam 2 require a positive sign of the crab sextupole strength, while Beam 1 left and Beam 2 right require a negative sign. Then, the horizontal chromaticity will be negative but negligible while the vertical one will be positive and will help to correct the total chromaticity in the vertical plane. The chromaticities induced by the crab-waist sextupole in the dispersion range

$[-0.1\text{ m}, 0]$ are presented in Fig. 4.16.

It should be noted that in this design, it has not been possible to create a negative dispersion in cw-sext that could be matched to the arc (for Beam 1 and $s > 0$). From Table 4.4, $D_{x,cs} > 0$ its value is positive and contributes to the total vertical chromaticity, but due to its low value, $D_x = 3.3$ mm, this contribution is small, only $\Delta Q'_y = -1.23$.

Table 4.5: Signs of the crab-waist sextupole strengths and required sign of dispersion at their location, for a positive contribution to the chromatic correction.

	$\text{sign}(k_{sl5})$	$\text{sign}(D_{x,cs})$
Beam 1 ($s < 0$)	$-$	$+$
Beam 1 ($s > 0$)	$+$	$-$
Beam 2 ($s < 0$)	$+$	$-$
Beam 2 ($s > 0$)	$-$	$+$

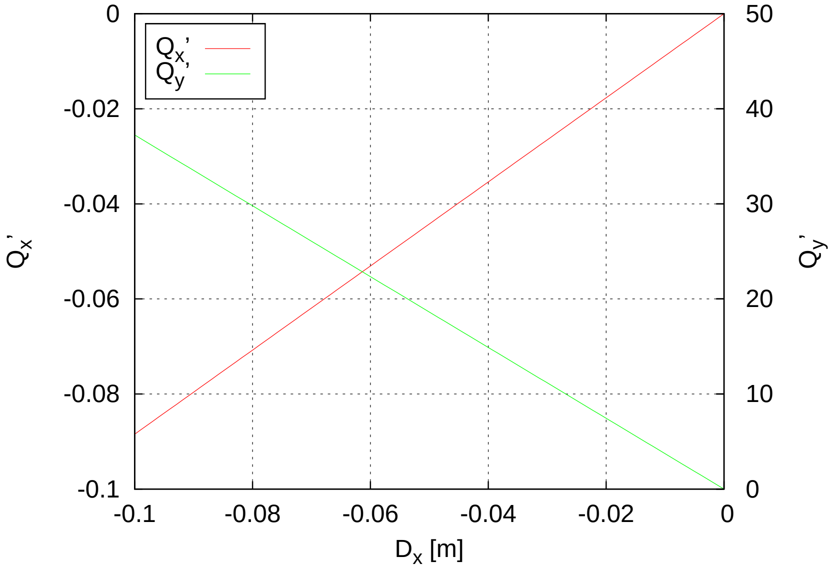

Figure 4.16: Chromaticities induced by a single crab-waist sextupole, taking for k_{sl5} the nominal value of integrated strength of the crab-waist sextupoles.

4.3.4 Chromatic Correction

The large values of the betatron functions create much more chromaticity than for the present LHC IR. Without taking into account the sextupolar component of the DHQ as potential corrector, the chromaticity induced by one side of the interaction region (in the range $[0, 260\text{ m}]$) is $Q'_x = -86$, $Q'_y = -417$, that brings $Q'_x = -172$, $Q'_y = -834$ for the whole IR (without considering the effect of the sextupolar component of the DHQ). In case of installing this IR for the two high luminosity experiments, the numbers would again be doubled, and the total much higher than the chromaticity generated by the arcs and the other 6 IRs: -80.4 units in the horizontal and -75.2 in the vertical plane. Therefore, the performance of a local chromatic correction is essential for the total chromaticity of the ring.

First, of all, from Table 4.4 we see that for sext.1 and sext.3, $\beta_y \gg \beta_x$ and while for sext.2 and sext.4 $\beta_x \gg \beta_y$. These conditions are a requisite for an efficient chromatic correction, together with the corresponding phase advances.

The criteria for the matching in Figs. 4.13 and 4.14 was to match the dispersion to its present value in the arcs and to close the geometry of the trajectories, as in Fig. 4.15. The objective was to check if it was possible to match with realistic elements, particularly with the new separator bending magnets. An optimization of the dispersion values at the sextupoles has not been done.

First, we analyze if the present dispersion values are useful for the chromatic correction. From the values in Table 4.4, we see that $D_x(\text{sext.3})$ should be ideally zero, but as $D_x(\text{sext.3})/D_x(\text{sext.1}) \approx 0.2$ the 'fight' is not severe. On the other hand, we find that $D_x(\text{sext.2}) \sim -D_x(\text{sext.4})$. In that case, as the strength of the sextupoles are comparable (for their geometric aberration compensation), and the dispersions are of the same order and of different sign, the chromatic contributions would have different signs, making it practically impossible, with this dispersion function, to accomplish the chromatic correction.

For the success of the chromatic correction, further conditions must be met. The β-ratio condition (1.69) should be improved. β_x/β_y has the values 84.8×10^{-3} for sext.1, 6.1×10^{-3} for sext.3, 5.8 for sext,2 , 2.6 for sext.4. In addition, the accuracy on the phase advances between sextupoles, as shown in Table 4.6 is not enough for an appropriate aberration cancellation.

Table 4.6: Errors in the phase advance between sextupoles in a pair.

$1-\lvert\mu_{x,1}-\mu_{x,3}\rvert$	$836.7 \times 10^{-5}\ \pi$ rad
$1-\lvert\mu_{y,1}-\mu_{y,3}\rvert$	$92.49 \times 10^{-5}\ \pi$ rad
$1-\lvert\mu_{x,2}-\mu_{x,4}\rvert$	$266.6 \times 10^{-5}\ \pi$ rad
$1-\lvert\mu_{y,2}-\mu_{y,4}\rvert$	$19.13 \times 10^{-5}\ \pi$ rad

4.3.5 Luminosity and Beam-Beam Estimation

The values $\beta^*_{x,y}$ were chosen so as to have the same beam cross section area at the IP as in the ATS optics. However, the large crossing angle required to have an opposite sign gradient for the two beams yields a small geometric luminosity reduction factor (1.78) of $S = 0.15, 0.17$, for each of the respective two scenarios in Table 4.1. The horizontal tune shift is larger than the vertical one, thus becoming the limiting factor. In the worst case, corresponding to a 50-ns bunch separation, the total tune shift is $\xi_{T;x} = 2\xi_x = 1.54 \times 10^{-3}$, far below present LHC tune shifts.

If the limits on beam parameters presented in Table 4.1 were evaluated to the present nominal LHC optics ($\beta^*_{x,y} = 0.55$ m, $\theta = 285$ μrad), the total beam-beam tune shift due to the two high luminosity interaction points would be $\xi_T = 0.0174$ for 25-ns bunch separation and $\xi_T = 0.0231$ for 50 ns. For the last case, it should be noted that such a large value has never been obtained for the LHC in the presence of long-range interactions. The new optics shows a considerable reduction of the tune shifts, coupled with a sensible reduction in luminosity (Table 4.7). Thanks to the much lower beam-beam tune shift, there is a considerable potential for the luminosity rise if the beam brightness, N/ϵ_N, can be increased.

Table 4.7: Luminosity and beam-beam tune shift per IP.

	L [cm^{-2}s^{-1}]	ξ_x [10^{-3}]	ξ_y [10^{-3}]
25 ns	3.7×10^{34}	0.49	0.33
50 ns	4.2×10^{34}	0.77	0.46

4.3.6 Influence on Luminous Region

The main topic here is the size of the overlapping of the colliding bunches. The value for β^*_y is much lower than the bunch length, but due to the large crossing angle, this is no longer an estimator for the length of the overlapping area, which has been computed as (1.87). This area is considerably reduced from that of nominal LHC. Then, due to its lower value with respect to β^*_y, the reduction in the vertical beam size is profitable for the luminosity, as the hourglass effect is negligible. The effect of reduction of the collision area then becomes visible.

The new IR determines a new collision scheme that must be evaluated, in order to assess if the experiments are able to deal with an event distribution that comes from a smaller overlapping area.

4.4 Matching a Symmetric IR Optics to the LHC Arcs

The LHC matching section is not flexible enough to match the highly perturbed β-functions to their values at the beginning of the dispersion suppressor. The dispersion suppressor has, therefore, been used as well to match the IR β-functions and the dispersion, that is not zero here, to their values in the arc.

As it was explained in Sec. 2.2.1, the arc optics of the LHC approximately follows the properties defined by the relations (2.6), (2.7), (2.8), (2.9), while the proposed IR fulfills relations (2.1), (2.2), (2.3), (2.4). We denote by L_{IR} and L_{ARC} the distances from the interaction point to the end of the interaction region and to the beginning of the arc, respectively. In particular, $L_{IR} = 260$ m, and $L_{ARC} = 434$ m. As a result of the antisymmetry of the LHC arcs, different matching sections are needed on the two sides of the IP for two reasons:

- The matching is performed from a symmetric optics around the IP, that is, over $s = \pm L_{IR}$, to an antisymmetric optics at location $s = \pm L_{ARC}$, which introduces different (asymmetric) conditions on the two sides of the IP.

- The dispersion has a non-zero slope at the IP, implying dispersion across the IR.

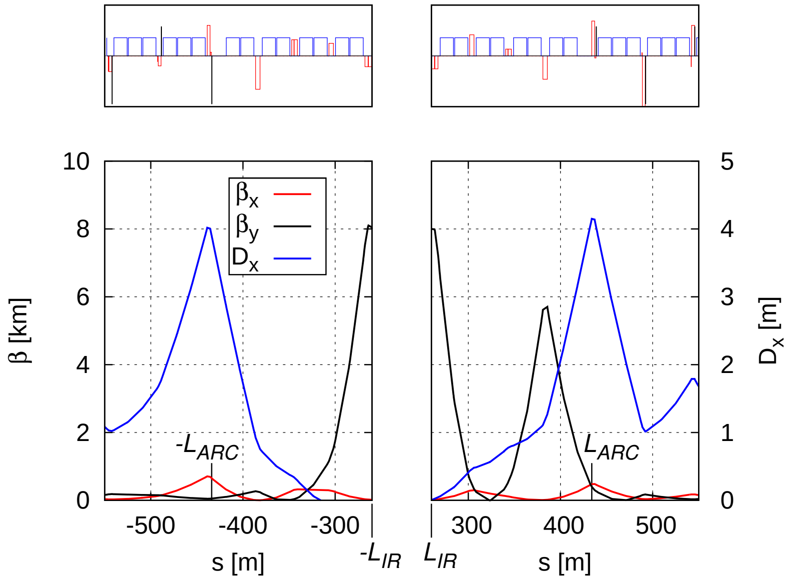

Figure 4.17: Interaction region matching to the arc at either side of the IP for Beam 1.

Figure 4.17 shows the matching at either side of the IP for Beam 1. The matching is done with the help of the quadrupole magnets of the LHC dispersion suppressor. In this first design a perfect matching to $\pm L_{ARC}$ has been accomplished, and an individual powering of the magnets in the first arc cell of the arc has been assumed to complete the matching. Even without the latter, the conditions at $\pm L_{ARC}$ are nearly met and this is useful to illustrate the fact that the matching from $\pm L_{IR}$ to $\pm L_{ARC}$ necessarily makes use of an asymmetric optics. The left side and right side matching would be equivalent (symmetric) to the respective right side and left side matching for Beam 2. Therefore, there is also an asymmetry Beam 1/Beam 2. Recalling the limitation on the difference in the excitation currents for the two beam apertures of a matching quadrupole due to the powering scheme (2.10), this latter constraint motivates the introduction of a symmetric matching, where the quadrupoles would have the same absolute value of the strength, but opposite sign.

In this section we address the particular case of matching the IR designed in this thesis, but it could be applied for the general case of matching a symmetric to an antisymmetric optics in an elegant and regular way. In this section we will refer to as matching section not what is called the LHC matching section, but the space between the regions with different kinds of symmetry, $s = \pm(L_{ARC} - L_{IR})$.

4.4.1 Twiss Functions Matching

From the point of view of the Twiss functions, the matching from $s = \pm L_{IR}$ to $s = \pm L_{ARC}$ can be made by a "symmetric left/right" and "symmetric Beam 1/Beam 2" matching section if the arc optics would fulfill the following conditions:

$$\beta_x(+L_{ARC}) = \beta_y(+L_{ARC});\ \alpha_x(+L_{ARC}) = \alpha_y(+L_{ARC}), \tag{4.10}$$

$$\beta_x(-L_{ARC}) = \beta_y(-L_{ARC});\ \alpha_x(-L_{ARC}) = \alpha_y(-L_{ARC}). \tag{4.11}$$

For $s = \pm L_{ARC}$ the Twiss functions are at the same time symmetric and antisymmetric, for both cases Beam 1/Beam 2 and left/right. Besides with $k(s) = k(-s)$, the matching section would have magnets with $k^1(s) = k^2(s)$, exactly as the magnets in the proposed interaction region.

On the other hand, an antisymmetric matching section is possible if the following conditions on the optics at $s = \pm L_{IR}$ are followed:

$$\beta_x(+L_{IR}) = \beta_y(+L_{IR});\ \alpha_x(+L_{IR}) = \alpha_y(+L_{IR}), \tag{4.12}$$

$$\beta_x(-L_{IR}) = \beta_y(-L_{IR});\ \alpha_x(-L_{IR}) = \alpha_y(-L_{IR}). \tag{4.13}$$

With those conditions, the transition between the symmetric and the antisymmetric region would be moved from $\pm L_{ARC}$ to $\pm L_{IR}$. This would be an advantage, but conditions (4.12) and (4.13) are difficult to meet for an optics with such a large β_x^*/β_y^*.

4.4.2 Dispersion Matching

Separator dipole magnets generate an antisymmetric dispersion around the IP. In general, due to the crossing of the beams, the dipolar strength of the separator magnets follows the relation $k_0(s) = -k_0(-s)$ (see Fig. 4.15) and $k_0^1(s) = -k_0^2(s)$. In the following discussion, it is assumed that the dispersion is zero at the IP. In the case of a symmetric arrangement of quadrupoles, $k_1(s) = k_1(-s)$, that is the case of the presented IR, this generates an antisymmetric dispersion

$$D_x(s) = -D_x(-s);\ D'_x(s) = D'_x(-s). \tag{4.14}$$

and for both beams, assuming a symmetric Beam 1/Beam 2 arrangement of the focusing elements, $k^1(s) = k^2(s)$:

$$D_x^1(s) = -D_x^2(s);\ D'^1_x(s) = -D'^2_x(s). \tag{4.15}$$

The dispersion has different sign at $s = L_{IR}$ and $s = -L_{IR}$, while

the dispersion in the arcs is positive at both sides:

$$D_x(L_{ARC}) \approx D_x(-L_{ARC});\ D'_x(L_{ARC}) \approx D'_x(-L_{ARC}), \tag{4.16}$$

$$D_x^1(L_{ARC}) \approx D_x^2(L_{ARC});\ D'^1_x(L_{ARC}) \approx -D'^2_x(L_{ARC}). \tag{4.17}$$

These relations were illustrated in Fig. 2.6 and Fig. 2.7. The aim is to match, for $s = \pm L_{ARC}$, conditions (4.14) and (4.15) to (4.16) and (4.17). The conditions on $D'_x(s)$ are already met, but those for the dispersion are only met if $D_x(\pm L_{ARC}) = 0$ and $D_x^1(\pm L_{ARC}) = D_x^2(\pm L_{ARC}) = 0$.

4.4.3 Modification of One LHC Cell

An attempt to meet the conditions (4.10) and (4.11) has been made by varying only the existing weak "trim quadrupoles" of the first arc cell (MQTLI.11, MQT.12, MQT.13) at both sides of the IP. The results are shown in Table 4.8. As $\beta_{x,y}(-L_{ARC}) \neq \beta_{x,y}(L_{ARC})$ and $\alpha_{x,y}(-L_{ARC}) \neq -\alpha_{x,y}(L_{ARC})$, we conclude that the trim quadrupoles do not give enough flexibility to "symmetrize" one arc cell, and we need to individually power the main quadrupole magnets of the first arc cell (MQ.11, MQ.12 and MQ.13 at both sides). The corresponding optics for Beam 1 of this new matching is shown in Fig. 4.18, and the numerical values of the optical functions are also included in Table 4.8.

Table 4.8: Optics parameters at the beginning of the arc ($s = \pm L_{ARC}$) for one arc cell modified by changing the trim quadrupoles only and by changing the strength of the main quadrupoles.

	One modified arc cell by varying trim quads		One modified arc cell by varying main quads	
s	$-L_{ARC}$	L_{ARC}	$-L_{ARC}$	L_{ARC}
$\beta_{x,y}$ [m]	136.2	145.1	137.5	137.5
$\alpha_{x,y}$	−0.71	0.60	−0.68	0.74
D_x [m]	2.1	2.5	2.1	2.1
D'_x	0.02	−0.01	0.02	−0.01

The results are much better and the optics is almost symmetric or "quasi-symmetric", as the values approximately fulfill the relations (2.3) and (2.4). It should be noted, however, that it would be expensive to individually power additional arc quads, due to their high currents. The solution is to modify the cells and to replace the MQ's by MQM's (but they will most likely be longer).

We note that the optics does not meet the conditions (4.14,4.15) because the arc dispersion has the same sign on both sides. A matching from (4.14,4.15) within $\pm L_{IR}$ to the dispersion in the arcs could be achieved by imposing one of the following two sets of conditions:

$$D_x(\pm L_{IR}) = D'_x(\pm L_{IR}) = D'_x(\pm L_{ARC}) = 0; \tag{4.18}$$

or

$$D_x(\pm L_{ARC}) = 0;\ D'_x(L_{ARC}) = D'_x(-L_{ARC}); \tag{4.19}$$

These conditions are sketched in Fig. 4.19, both showing a matching to the arcs by a symmetric section. The dipoles are not represented for the sake of simplicity, but it both plots it is assumed that the dispersion is generated by dipole magnets with $k_0(s) = k_0(-s)$.

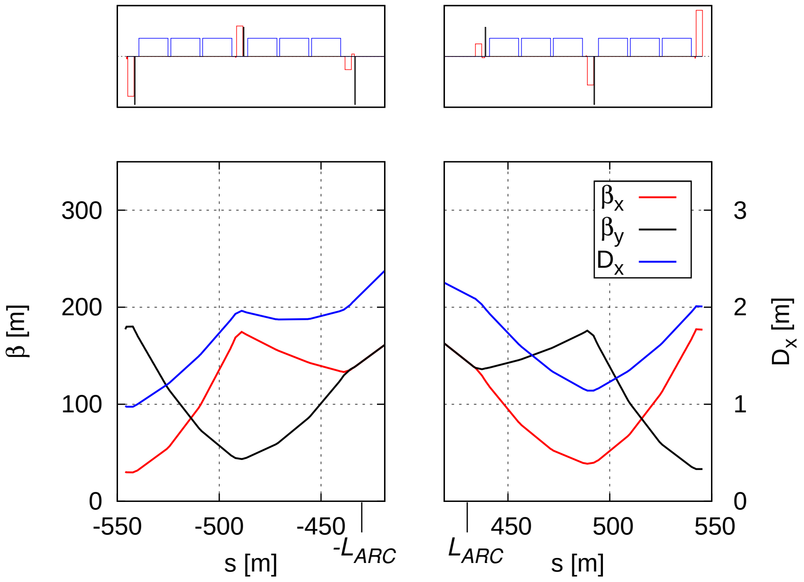

Figure 4.18: Modified optics of the first LHC arc cell on each side of the IP (Beam 1), for matching the arcs to a symmetric IR optics.

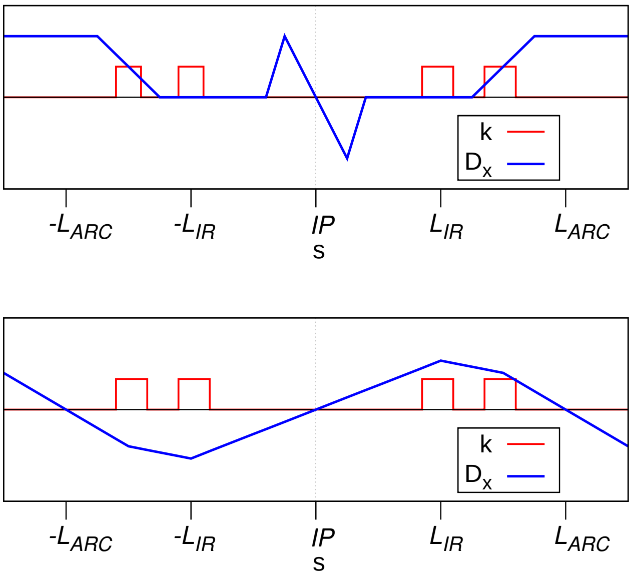

Figure 4.19: Sketch for the conditions on dispersion matching: (4.18) [top] and (4.19) [bottom].

4.4.4 Modification of Two LHC Cells

We have just seen that by modifying a single cell, the β-functions can be made to be equivalent on both sides of the IP, but this is not the case for the dispersion. Therefore, we have explored whether by modifying two cells we can make the optical functions on either side of the IP fully identical. The final two arc cells have been modified by varying the strengths in quadrupoles MQ.14 and MQ.15 in addition to those varied in the previous section. Matching to (4.18) and (4.19) has been attempted. For the right side, if $D_x(L_{ARC}) = 0$ is forced, the α-values at the beginning of the arc are inverted between the planes, $\alpha_x(L_{ARC}) \sim -\alpha_y(L_{ARC})$, and the same has been observed for the left side, namely $\alpha_x(-L_{ARC}) \sim -\alpha_y(-L_{ARC})$. Imposing $D'_x(L_{ARC}) = 0$ yielded $\alpha_x(L_{ARC}) = \alpha_y(L_{ARC})$, on the right side, while on the left side the α-functions were again inverted. Finally, as in the case for a single modified arc cell, a matching to $\beta_x(L_{ARC}) = \beta_y(L_{ARC})$, $\alpha_x(L_{ARC}) = \alpha_y(L_{ARC})$ was tried, to explore if there was a significant improvement. The result of the matching with modifications in two arc cells is shown in Fig. 4.20, and the values for the optics parameters are summarized in Table 4.9. These results are better than for one arc cell. In fact, the matching of the β- and α-functions is almost exact, but as for the case of one modified arc cell, it was not possible to fulfill the dispersion conditions (4.14) and (4.15). In this case we would have to replace the MQs magnets by MQM in two cells, which would be even more expensive than for one cell.

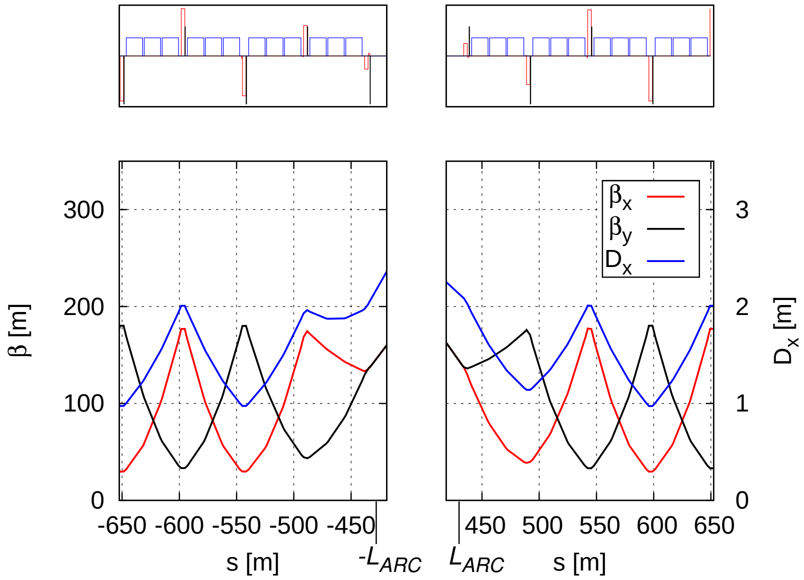

Figure 4.20: Modified optics of the two first LHC arc cells on each side of the IP (Beam 1), for matching the arcs to a symmetric IR optics.

Table 4.9: Optics parameters at the beginning of the arc for two modified arc cells.

	$-L_{ARC}$	L_{ARC}
$\beta_{x,y}$ [m]	137.5	137.5
$\alpha_{x,y}$	-0.74	0.74
D_x [m]	1.9	2.1
D'_x	0.02	-0.01

4.5 Alternatives

The large crossing angle induces a very low geometric luminosity reduction factor, that takes away a part of the luminosity gain achieved by the low beam cross section, $\pi\sigma_x^*\sigma_y^*$. We need the large crossing angle to accommodate large bunch populations. However, there is still a big margin for this, and a bigger luminosity could be made by reducing the crossing angle. This must be done by keeping the large beam separation at the double-half quadrupole, $\Delta_{beam} = 90$ mm. Two ways of reducing the crossing angle for a given aperture could be using crab cavities, or adding a dipole insertion within $s = \pm L^*$ [73]. On the other hand, the use of unequal emittances in the two planes could help to relax the constraints of this problem.

4.5.1 Crab Cavities

As commented in Sec. 4.1.4, the use of crab cavities has been discarded for our optics development. However, it is worth remarking how crab-cavities could have potential benefits. They appear as an option to increase the luminosity for the HL-LHC by reducing the effective crossing angle to zero. In a crab-waist upgrade they could be installed to reduce that angle and to increase the luminosity. They would also allow a control on the crossing angle to vary the luminosity (called luminosity levelling). A radio frequency crab cavity gives a kick on the bunch proportional to the distance from the bunch center, which produces a longitudinal bunch rotation. In the presence of the large Piwinski angle, the resonances induced by the crab-cavites would not be high [74].

4.5.2 Dipole Insertion

It would be possible to use a dipole to reduce the crossing angle. Two options can be considered. The first one would be to install a dipole in the experimental cavern in a similar way as the D0 dipoles proposed in the Early separation scheme [73], but this would have the drawback of reducing the available free length needed for the detector. The second one would leave the 23 m at each side of the IP untouched and place the dipole as first element. But this option must be discarded since the β-functions would be even larger.

4.5.3 Double-Aperture Quadrupole

Also, a very important limitation is the design of the DHQ. As we saw, it introduces some issues arising from its large sextupolar component and relatively low gradient, that imposes a large element to have a strong integrated quadrupole strength to perform the tight focusing. The ideal case would be to install double-aperture quadrupoles instead. However, this requires a larger crossing angle that decreases the luminosity drastically through the geometric luminosity reduction factor. Following the geometric condition (4.1), and taking the beam separation in the arcs, $\Delta_{beam} = 194$ mm, the crossing angle would be at least $\theta = 8.4$ mrad, and this value is too high. But this solution could be combined with those of Sec. 4.5.1 and Sec. 4.5.2 to arrive to a viable configuration.

4.5.4 Unequal Emittance in the two Planes

One of the limitations of the crab-waist collision scheme is its requirement for the beam size ratio in the interaction point (3.16). By assuming an equal emittance in the two transverse planes, this directly translates into a strict condition on the β-function, namely $\beta^*_y/\beta^*_x > 100$. If it were possible to flatten the emittance, the requirement on the β^*-ratio could be relaxed. Defining an emittance factor, $r_\epsilon = \epsilon_x/\epsilon_y$, the β-ratio could be reduced by the same factor,

$$\frac{\beta^*_x}{\beta^*_y} \geq \frac{1}{r_\epsilon} 100. \tag{4.20}$$

This would not have any influence on luminosity, but would allow easing the optics design. In particular, $r_\epsilon = 4$ would allow $\beta^*_x = 0.75$ m, $\beta^*_y = 3$ cm. In addition, a further advantage would be that the requirements on the integrated strength of the crab-waist sextupoles would be reduced through a reduction of the crab-waist IP factor (3.12). If β^*_x is kept constant, k_{sl} of the crab-sextupoles can be reduced by a factor r_ϵ; and by the factor $\sqrt{r_\epsilon}$ if the product $\beta^*_x\beta^*_y$ is the same.

On the other hand, there is a limitation on the DHQ in terms of geometrical aperture. If we assume the product of the emittances to be constant, and we denote by ϵ_r the geometric mean of the transverse emittance, $\epsilon_r = \sqrt{\epsilon_x\epsilon_y}$, the luminosity (1.77) can be re-expressed as a function of r_ϵ and ϵ_r,

$$L = \frac{N_1 N_2 f n_b}{4\pi\epsilon_r\sqrt{\beta^*_x\beta^*_y}} \left[1 + \frac{\sigma_s^2\theta^2}{4\epsilon_r\sqrt{r_\epsilon}\beta^*_x}\right]^{-1/2}. \tag{4.21}$$

The squeeze of the emittance ellipse allows fitting a larger β_y in the DHQ. In the horizontal plane we are far from the aperture limit so that we can keep the same β^*_x. Then, by reducing the β^*_y, we can increase the luminosity. The first factor in (4.21) increases as β^*_y decreases, while the second factor increases when unequal emittances are introduced ($r_\epsilon > 1$). Thus, there is an overall effect favourable for the luminosity when unequal emittances are introduced, as shown in Fig. 4.21, where we see the luminosity increase for different ϵ_r.

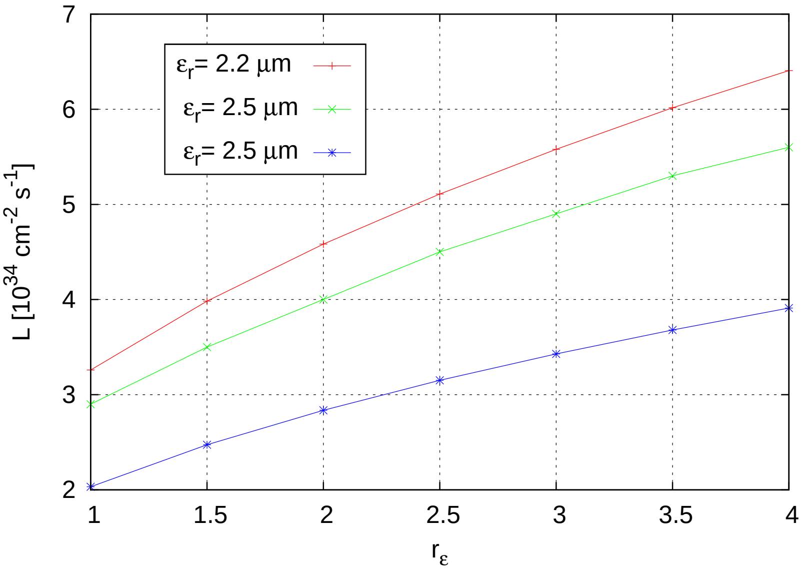

Figure 4.21: Luminosity as a function of the emittance factor ($r_\epsilon = \epsilon_x/\epsilon_y$), for different ϵ_r.

4.6 Conclusions

- An LHC with crab-waist collisions would reduce the strength of some resonances and would decrease the footprint area.
- For the same peak luminosity, a configuration with a higher number of particles yields more integrated luminosity over the same time.
- The implementation of the crab-waist collision scheme requires extremely flat beams. The optics induces large β-functions that create a chromaticity which is impossible to correct in the arcs. It is necessary to make a local chromatic correction which requires a symmetric optics and dispersion along the IR ($D_x'^* \neq 0$).
- The symmetric optics can be realized with a new element: the double-half quadrupole. Another option can be used, a pure sextupole.
- The requirements on the sextupole strength of the crab-waist sextuples are very demanding, as a consequence of the large crab-waist IP factor, $k_{sl,IP}$.
- Also very demanding is the condition $\Delta\mu_x = \pi m$. It is not difficult to achieve it at one point, but it is more difficult to maintain it along the element, which is a consequence of the demanding sextupole strength, and that the magnet must be built within a length of several meters. It is also very complicated to get at the same time a large value on $\sqrt{\beta_x}\beta_y$ in the sextupole to ease its strength.
- The optics at the crab-waist sextupole is a compromise between strength and phase advance in the sextupole. The β-functions should be as large as possible in these

elements, but a large β_x fights with the requirements on the horizontal phase advance from the IP.

- In order to match $\beta_x^* = 1.5$ m, $\beta_y^* = 1.5$ cm to the arc optics, the quadrupoles of the dispersion suppressor must be used. In principle a suppression of the dispersion is not necessary as the local chromatic correction requires dispersion along the IR. However, a $D_x = 0$ and $D_x' =0$ at the beginning of the IR would help in the dispersion matching. The matching to the arc has been done, including that of the strength of the new separator bending magnets. A geometry matching has been performed with realistic dipole magnets.
- The design explained in Sec. 4.3, in order to work, should be modified by readjusting the phase advances between the sextupoles in each pair, setting $D_x(\text{sext.3}) = D_x(\text{sext.4}) = 0$ and by adjusting the β-ratio so that it has the same value in each sextupole of both pairs. These facts, together with the too short an overlapping area and limited luminosity, motivated the design of another IR optics, described in the next chapter.

5. A Flat-Beam LHC with Local Chromatic Correction

We saw in Chapter 4 the conditions for a new IR, with a final design of the IR matched to the ring. Its study inspired the design of a second new IR design, with relaxed values of $\beta_x^* = 3.5$ m, $\beta_y^* = 3.5$ cm, which is developed in this chapter. A full analysis including chromatic corrections and tracking simulations for the crab-waist collision scheme has also been done.

5.1 Motivation of the New Design

The interaction region which was previously studied in Chapter 4, with $\beta_x^* = 1.5$ m and $\beta_y^* = 1.5$ cm, induced a very large maximum β_y ($\sim$ 50 km), resulting in a large chromaticity which was proven difficult to correct locally without creating other noticeable aberrations. In order to reduce the chromaticity, the $\beta_{x,y}^*$-values have been increased by about a factor 2.3 ($\beta_x^* = 3.5$ m, $\beta_y^* = 3.5$ cm), preserving the ratio β_x^*/β_y^*, as a requirement for the crab-waist collisions. The enlarged values of $\beta_{x,y}^*$ allow a simplification of the chromatic correction, so that only the vertical chromaticity must now be corrected locally, while the horizontal chromaticity has become small enough to be corrected using only the arc sextupoles.

Table 5.1 summarizes the parameters of this new optics. The crossing angle has been reduced to compensate the loss in luminosity arising from the enlarged values of the betatron functions at the IP. This reduction, together with the increase in σ_x^*, reduces the Piwinski angle from its previous value. However, it is still large enough, and the vertical β^* value is between the length of the overlapping area and the bunch length ($l_{OA} < \beta_y^* < \sigma_s$), showing that the Piwinski angle effectively helps in a reduction of the vertical β-function at the IP compatible with a negligible hourglass effect. With regard to the crab-waist IP factor, $k_{sl,IP}$, it is almost unchanged. Recalling its definition (3.12), the increase on β_y^* should reduce $k_{sl,IP}$, but this reduction is cancelled by the increase in β_x^* and the reduction in the crossing angle.

5.1.1 Rescaling of the DHQ

The reduced crossing angle leads to less beam separation at the entrance of the DHQ: Δ_{beam}, so that with the field distribution in Fig. 4.6 this magnet generates less focusing gradient. However, we propose to solve this issue by a smaller aperture of the DHQ in both planes. The reduction in a_x is justified by the reduced crossing angle while the reduction in a_y is possible

Table 5.1: Parameters for the new LHC optics.

$\beta^*_{x,y}$	3.5 m, 3.5 cm
$\beta_{MAX;x,y}$	5.4 km, 21 km
θ	2.6 mrad
D'^*_x	$\pm$ 0.002
ϵ_N	2.4–3.75 μm
σ^*_x	33.6–41.9 μm
σ^*_y	3.3–4.2 μm
σ_s	7.5 cm
ϕ	2.3–2.9 rad
l_{OA}	2.6–3.2 cm
Δ_{beam}	60 mm
Δ_{in}	271–217 σ_x
$k_{sl,IP}$	20.6×10^3 m$^{-1/2}$ rad^{-1}

due to the decrease of β_y in the DHQ as consequence of the larger β^*_y. For this reason, a new DHQ is proposed with reduced dimensions, but keeping $a_x = a_y$ to preserve the same square shape. Specifically, the dimensions are reduced from 120 mm to 80 mm. Figure 5.1 shows a sketch of the beams in the rescaled DHQ, where not all the coils are shown, but only those next to the window.

The maximum beam size in the DHQ would correspond to a 11-σ ellipse with dimensions $(11\sigma_x, 11\sigma_y)$ = (5.6 mm, 35.8 mm). The ellipses shown in the picture correspond to the most limiting case in aperture, with a normalized emittance of $\epsilon_N = 3.75$ μm. For $\epsilon_N = 2.4$ μm, the sizes would be smaller: $(11\sigma_x, 11\sigma_y)$ = (4.5 mm, 28.6 mm).

The field distribution has been scaled following two assumptions. The first one is to preserve the maximum value of the magnetic field, which is located at the horizontal edges of the element: $|B_{y,p}| = |B_y(\pm a_x)| = 7.5$ T. The second assumption is that all the multipoles are reduced by the same factor. After some iterations it was found that a reduction factor of 1.5 yields the same maximum B_y, which we can see in Fig. 5.2, where the resultant magnetic field distribution is plotted.

Even though all the multipole terms have been divided by the same factor, as the point of interest varies, the relation is more complicated. First of all, the gradient at the location of the beams has sligtly dropped from 116.7 T/m to 113.3 T/m, but more significant is the increase on the minimum of $|B_y|$, which is given at $x = 0$ and has grown from 2.9 T to 4.4 T. Also, the dipolar component at the respective position of the beams in each case increase, from 5.5 T to 6.1 T, hence producing a slightly larger deflection. Regarding the last parameter of interest for the optics design, the sextupolar gradient, it has increased from $|g_s| = 2.75$ kT/m^2 to 3.99 kT/m^2.

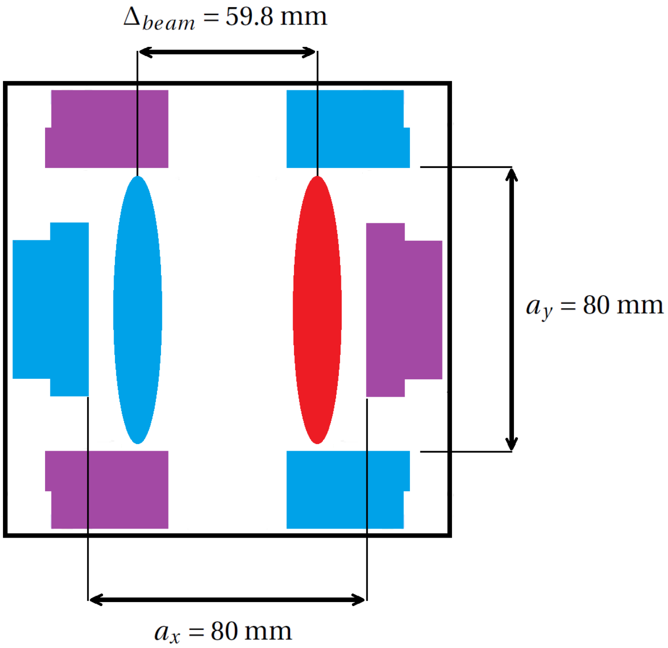

Figure 5.1: Cross section of the two beams in the DHQ represented as a 11-σ ellipse for Beam 1 (blue) and Beam 2 (red).

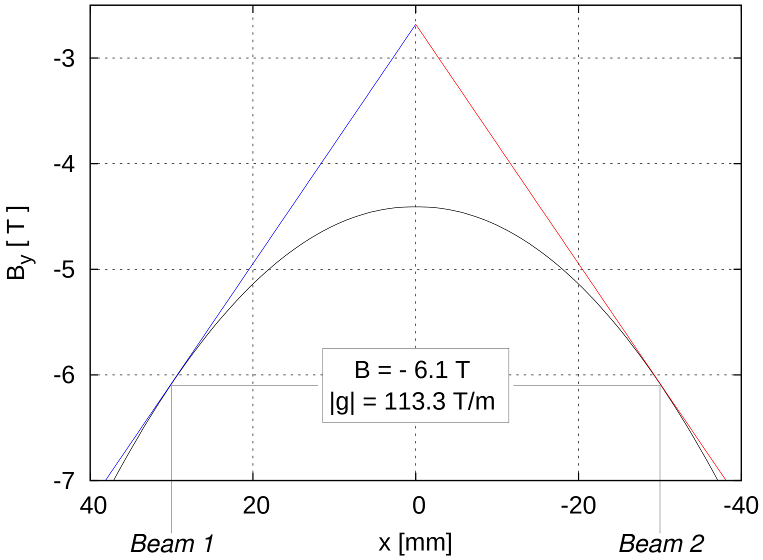

Figure 5.2: Estimation of the magnetic field distribution along the horizontal axis for the rescaled DHQ at the left side of the IP (s<0). The center of the beams is now located at $x = \pm 30$ mm.

5.2 Second Interaction Region Design

5.2.1 Optics and Geometry

The new optics is shown Fig. 5.3 for Beam 1, where dispersion and betatron functions have been fully matched to the LHC ring. The optics can be compared with that of the previous design, in Fig. 4.13. Like the optics of Chapter 4, this one is “symmetric Beam 1/Beam 2” and “symmetric left/right”, which implies the fulfillment of relations (2.1), (2.2), (2.3) and (2.4).

First of all, the position of the crab-waist sextupole (cw-sext) is the same, and so is the length of the interaction region, $2L_{IR}$, The phase advances from the IP to cw-sext are also the same, $\Delta\mu_x = 2\pi$ rad and $\Delta\mu_y = 5\pi/2$ rad. What is different is the maximum of both β-functions, which has been considerably reduced from 49 km to 22 km. This maximum value, in the case of β_y, is assumed in the DHQ and determines the integrated quadrupolar strength of the element, which in this case is less demanding.

Therefore, the length of the DHQ has been reduced from 14 to 11 m, in addition to the reduced quadrupolar strength. Another important difference is that the dispersion values are much more reduced, due to the fact that the slope of the dispersion at the IP, $D_x'^*$, is much smaller. The aim, in principle, is to locally correct the vertical chromaticity with the sextupolar component of the DHQ only. An additional sextupole (called ‘sext.3’, to be consistent with the previous design) is located at $s = \pm 173.5$ m, and its purpose is to correct the second order geometric aberrations generated by the DHQ. As for the first design, the focalizing elements DHQ and a new set of quadrupoles (quad.2, quad.3 and quad.4) with interleaved dipoles substitute the present LHC triplet (Q1, Q2, Q3). The parameters of the proposed new

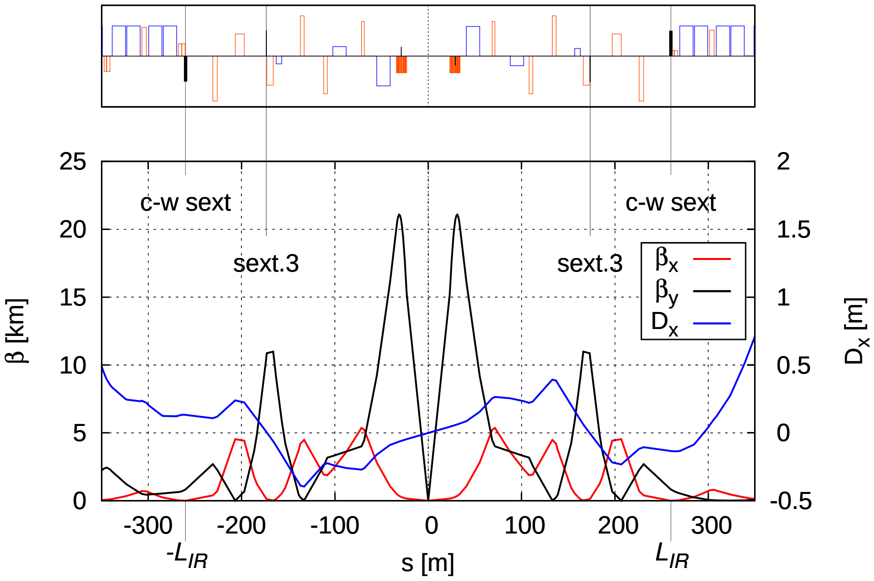

Figure 5.3: New LHC IR1 & IR5 optics for Beam 1, with β_x^*/β_y^* = 3.5 m/3.5 cm, with the sextupoles at their potential locations and with their respective polarity.

quadrupoles are listed in Table 5.2. A comparison with those of the first design (Table 4.3) shows that the elements are much stronger but on the other hand they are much shorter. In fact the integrated quadrupole strengths are slightly reduced. It should be noted that the aperture radius represents the minimum for hosting the beam as a 11-σ ellipse, but there is sufficient margin to increase the magnetic field, so that the radius can be increased if required.

Table 5.2: Parameters of the final-focus double aperture quadrupoles for the second design: gradient, magnetic length, aperture radius, maximum magnetic field in the coil and integrated quadrupole strength. The radius is computed as 11max(σ_x, σ_y)+5 mm, with $\epsilon_N = 2.4\ \mu m$, and the maximum magnetic field in coil as $|B_p| = gr$.

	g [T/m]	L_q [m]	r [mm]	$\lvert B_p\rvert$ [T]	k_l [10^{-3}m^{-1}]
quad.2	240	3.0	19.5	4.7	30.8
quad.3	−260	4.0	16.0	4.2	−44.5
quad.4	278	4.0	18.0	5.0	47.6

The reference orbits are shown in Fig. 5.4, with a sketch of the dipoles and of the dipolar component of the DHQ. The maximum excursion of the orbits in the interaction region has been drastically reduced from 30.8 cm (Fig. 4.15) to 10.6 cm. The parameters of the three bending magnets installed in place of the present LHC dipole separator magnets D1 and D2 are presented in Table 5.3. These magnets are weaker than those of the previous design and the magnet production would be easier. In fact, the fairly small orbit shifts (See Eq. (4.7)) in sepd.2 and sepd.3 allows fabricating these magnets with parallel apertures, like the separator magnet D2 for the present LHC. The magnet that will present more problems for a straight magnet geometry is sepd.1.

Table 5.3: List of separation bending magnets indicating the magnetic length, maximum magnetic field, and maximum orbit excursion.

	L_b [m]	$\lvert B_y\rvert$ [T]	ΔX_{MAX} [mm]
sepd.1	14.3	8.2	22.2
sepd.2	14.3	2.6	5.1
sepd.3	6.0	2.1	3.8

For the computation of the bending magnet strength and position we had to take into account several boundary conditions affected by these magnets:

- Geometric requirements of the reference orbits: required crossing angle at the interaction point, $X'(0) = \theta$, and LHC half beam separation after the compensator sextupole, $X(\text{sext.3}) = 97$ mm.
- Zero dispersion in the compensator sextupole, $D_x(\text{sext.3}) = 0$.
- Slope of dispersion in the compensator sextupole as small as possible, $D_x(\text{sext.3}) \sim 0$, in order to ease the matching to the arc; otherwise it would have negative values in c-w sext.

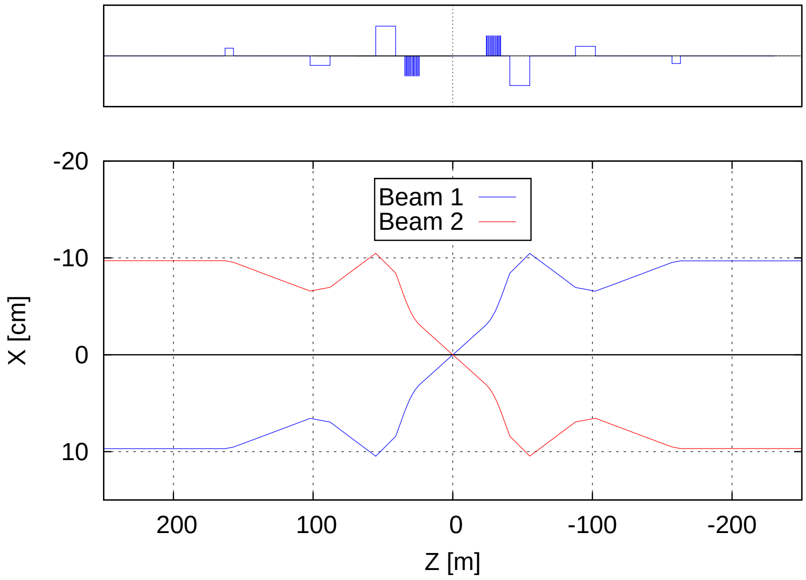

Figure 5.4: IR crossing scheme for the second design, showing the reference orbits for both beams. The upper plot represents for Beam 1 the dipolar strength of the dipoles and of the DHQ (as a filled blue box).

- Dispersion as small as possible in the crab-waist sextupole D_x(c-w sext)~ 0. If not, it will create additional chromaticity, as pointed out in Sec. 4.3.3.

The dispersion-orbit matching was done together with the β-matching, as the strengths of the quadrupoles affect the dispersion function. The aims of the betatron matching are:

- Same β-ratio at the center of the DHQ and at the compensator sextupole, (β_x/β_y)(DHQ)= (β_x/β_y)(sext.3) and $(\beta_y \gg \beta_x)$.
- Requirement for phase advance $\Delta\mu_x = \pi$, $\Delta\mu_y = \pi$ from the center of the DHQ.
- Requirement for the phase advance of the crab-waist sextupoles from the IP (See 3.5), and maximizing β_y on c-w sext to minimize its strength.
- Possibility to match the IR to the arc optics.

5.2.2 Chromatic Correction

The vertical chromaticity, Q'_y, is compensated directly in the DHQ, making use of the large sextupole component and nonzero dispersion in this magnet. The value of the D'_x at the IP has been carefully calculated in order to correct locally Q'_y with the help of the sextupolar component of the DHQ.

The compensator sextupole compensates most of the geometric aberrations. As the dispersion is zero at its location, it does not contribute to the chromaticity and its strength influences only the aberration correction. Table 5.4 lists the total chromaticity for the LHC with the new IR introduced for at IP1 and the present nominal IR (with $\beta^*_{x,y}$ = 0.55 m) in IP5. The total chromaticities are shown for different strengths of the positive arc sextupoles k_{sf} (located next to the focusing arc quadrupoles) and the negative ones, k_{sd} (next to the defocusing quadrupoles).

Table 5.4: Chromaticity of the full LHC machine with the second design IR (β^*_x/β^*_y = 3.5 m/3.5 cm) for IP1, for different configurations of the arc sextupole strengths.

	arc sext. switched off	arc sext. like nominal LHC	optimal configuration for the arc sext.
k_{sf} [m^{-3}]	0	0.10	0.17
k_{sd} [m^{-3}]	0	−0.17	−0.18
Q'_x	−246	−107	2.0
Q'_y	−122	11	2.0

With all the arc sextupoles set to zero (first column), the horizontal chromaticity Q'_x is much higher than the vertical, because it is not locally corrected. The second column represents the case where the arc sextupoles are excited at the strength needed to correct the chromaticity in the present LHC to $Q'_x = 2$, $Q'_y = 2$. There is still a large residual Q'_x, but it can be compensated by setting the sextupole strengths as shown in the third column. This is a very elegant solution, as $k_{sf} \approx k_{sd}$. The higher dispersion in the focalizing sextupoles is the reason why they can correct the horizontal chromaticity with approximately the same sextupolar strength as the defocalizing sextupoles.

If the new flat-beam IR is to be introduced in IP5 as well, the arc sextupoles alone cannot be excited strongly enough to correct the full horizontal chromaticity. Another correction scheme should then be used. Possible solutions include the Achromatic Telescopic Squeeze, already addressed in Sec. 3.1.1, use of the sextupole spool pieces in the dipole magnets, or a dedicated local correction for the horizontal plane in the IR region. For the latter option, we addressed the difficulty of such design in Chapter 4, but the reduced β-functions of this second IR optics will make it more feasible.

5.2.3 Aberration Compensation

The aim of the compensator sextupole (sext.3), is the cancellation of the geometric aberrations generated by the sextupolar component of the DHQ. It was a design constraint to have the same β_x/β_y as in the center of the DHQ, in view of the condition (1.69).

The sextupole strength of sext.3 is very large. Its integrated strength is $|k_{sl}| = 5.06$ m^{-2}, and this is an excessive value if we compare it, for example, with the integrated strength of the LHC defocusing sextupoles, which has a value of $|k_{sdl}| = 6.27 \times 10^{-2}$ m^{-2}, i.e. two orders of magnitude lower.

A look at (1.68) shows us that the required large k_{sl}-value of sext.3 comes from two facts. The first one is the large ratio between the values of the betatron functions in the DHQ and sext.3: $(\beta_x(\mathrm{DHQ})/\beta_x(\mathrm{sext.3}) = \beta_y(\mathrm{DHQ})/\beta_y(\mathrm{sext.3}))$. This condition cannot be easily relaxed, as the β-functions must reduce progressively from their maximum value in the DHQ to their values in the arcs without generating too much additional chromaticity. The second cause for the large k_{sl} is the length of the DHQ, that imposes a large integrated sextupolar component $k_{sl,DHQ}$. This is a consequence of the large ratio between the sextupole and the quadrupole component of the DHQ. The length of this element is 11 m, which is approximately the double of the first quadrupole (Q1) for the present LHC, while its gradient is half of that of Q1. This implies that the DHQ contains a very large $k_{sl,DHQ}$.

On the other hand, there is a further issue. From (1.69) the optics must preserve the ratio (β_x/β_y) along the DHQ and the sextupole. As they are long elements and the β-functions and quadrupolar fields are different, this ratio is not preserved, and there is also a considerable phase advance along these elements. From Fig. 5.5 we extract that in principle, the aberrations cannot be completely compensated.

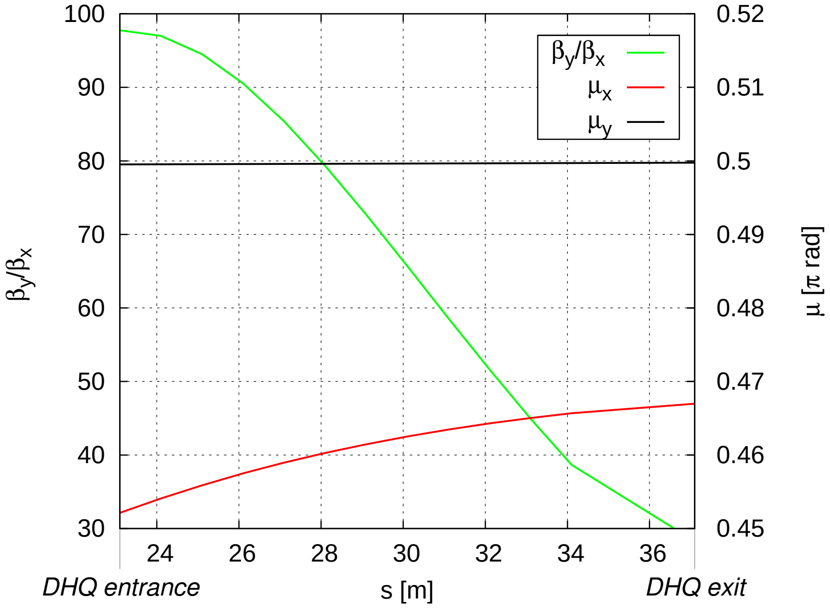

Figure 5.5: β-ratio and phase advances from the IP in the range of the DHQ.

Both issues indicate that a realizable optics would not be possible with a scheme involving a large DHQ. A possible alternative scheme could be to use a combined element for the vertical focusing. This element would be a combination of a DHQ and a double aperture quadrupole with opposite gradient for both beams. The DHQ provides a fraction of the required focusing as well as assisting in the beam separation, thanks to its dipolar field component. Following this pair of elements, bending magnets could be installed to help bring the beams to an optimum separation so that they could pass through different channels of an upstream quadrupole with much higher quadrupolar field. Such a scheme is sketched in Fig. 5.6. In case the sextupolar component is not large enough to correct the chromaticity, an additional sextupole can be added for this purpose, so that the chromatic correction does not exclusively rely on the sextupolar component of the DHQ, but on the sum of this component and the additional sextupole.

However, in order to finalize the present optics considered above and being able to perform the tracking simulations that will be presented later on in this chapter, $k_{sl,DHQ}$ has been added in the model (Fig. 5.3) as a thin sextupole (with zero length), located in the center of the DHQ. The strength of the sextupole is taken to be the same as the integrated one of the DHQ, as the worst case scenario. If the strength were reduced, this would imply a larger $D_x'^*$, as the chromatic correction is approximately proportional to the product $k_{sl,DHQ} \cdot D_x(\mathrm{DHQ})$ (1.95).

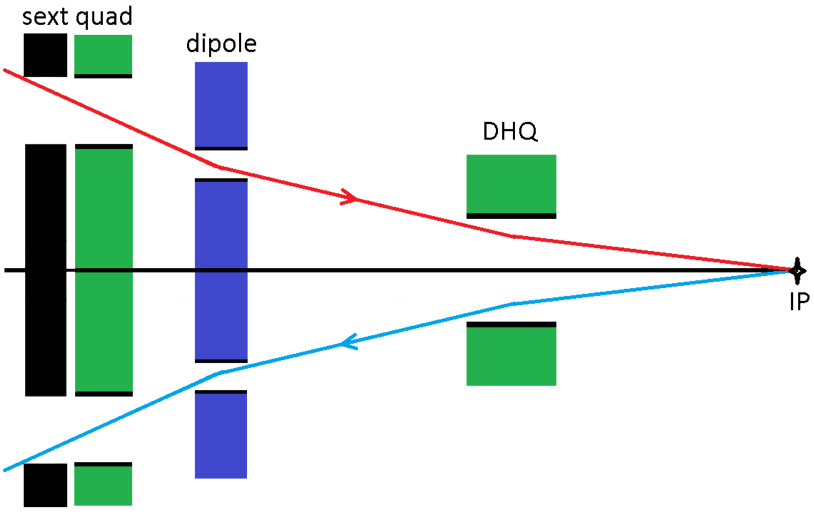

Figure 5.6: DHQ plus quad, showing the reference orbit of the two beams.

With regard to the compensator sextupole, it has also been modelled as an element of zero length. The accuracy of the phase advance between the center of the DHQ and the compensator sextupole is $\left(1 - |\Delta\mu_x|\right) = \left(1 - |\Delta\mu_y|\right) = 0.2 \times 10^{-8}\pi$ rad. If we compare it with the values achieved in the previous model (Table 4.6), we observe that the error is 5 orders of magnitude smaller. Tracking simulations have proven that these phase advance errors are small enough to effectively suppress the geometric aberrations as we will comment in Sec. 5.3.3.

5.2.4 Matching to the Arc Optics

As in the first design, the matching is done from a symmetric (IR) to an antisymmetric optics (LHC arc). Therefore, the matching shown in Fig. 5.7 is asymmetric. The betatron functions are considerably reduced compared with the first design, due to the higher $\beta^*_{x,y}$. Moreover, the dispersion is higher, and this is a consequence of the larger value of the dispersion at the end of the interaction region, $D_x(\pm L_{IR})$. In order to obtain a more regular optics, the considerations of Sec. 4.4 can be taken into account.

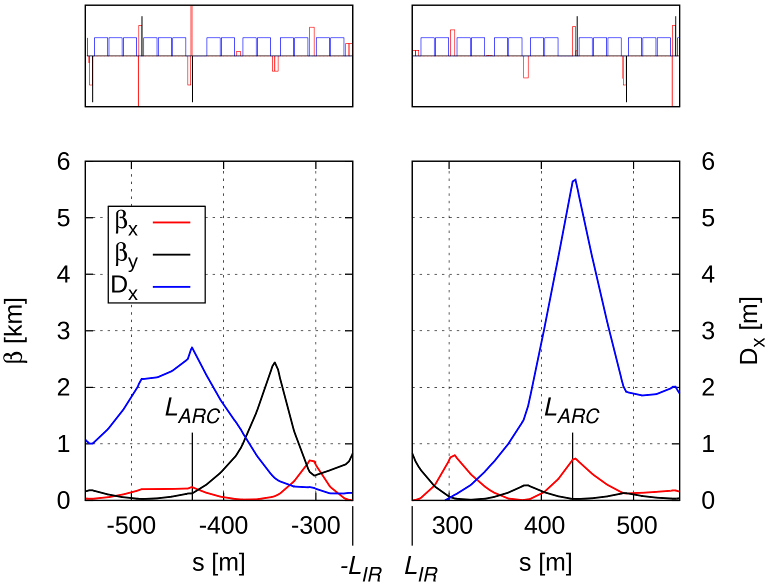

Figure 5.7: Detail of the IR matching to the arcs for Beam 1.

5.3 System Performance

5.3.1 Luminosity

Figure 5.8 illustrates the peak luminosity and the beam-beam parameter as a function of bunch intensity for one interaction region. In case the flat-beam IR is substituted in both IP1 and IP5, as the crossing takes place in the horizontal plane in either IP, the values of ξ_x and ξ_y are simply doubled, still remaining below 0.01. For the present LHC, bunch populations above 3 $\times 10^{11}$ would not be possible at the same ϵ_N, due to an excessive beam-beam tune shift. It should be noted that bunch intensities above 2.2×10^{11} fall out of the limits indicated in Table 4.1, but one of the main limitations, that of the beam-beam tune shift, has been clearly overcome.

5.3.2 Chromatic Beta Beat

A parameter that shows directly the benefit of the chromatic correction of all the machine is the chromatic β-beat. For its computation, expressions (1.96) and (1.97) have been used for the horizontal and for the vertical β-beat, respectively, with $\delta = 3 \cdot \sigma_\delta = 3.3 \times 10^{-4}$. Both integrals are calculated over all the machine. They are very sensitive to the transverse tunes used, (Q_x, Q_y), i.e., the working point. In particular, if the tune for a given plane approaches an integer or half integer value, the β-beat in that plane blows up. The reason is that $Q^0_{x,y} = n/2$ represents a singularity according to (1.96) and (1.97).

The nominal tune for the present LHC is $(Q_x, Q_y) = (64.31, 59.32)$, whose decimal values are far from any resonance. However, the different phase advances in the new interaction region changed the global tunes of the machine to (65.28, 60.40), where some resonances

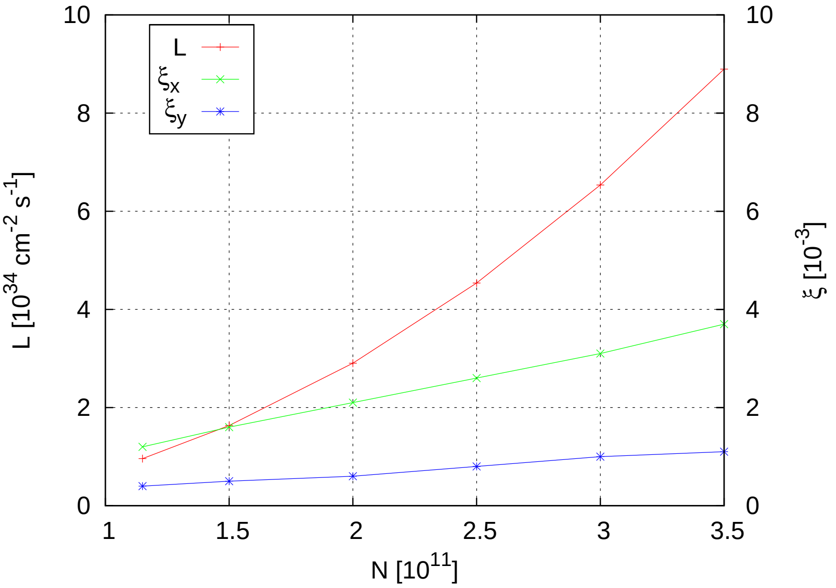

Figure 5.8: Luminosity and beam-beam tune shifts at one IP for the new IR with $\epsilon_N = 2.4$ μm as a function of bunch population. For the luminosity calculation, the total number of bunches is taken to be $n_b = 2808$.

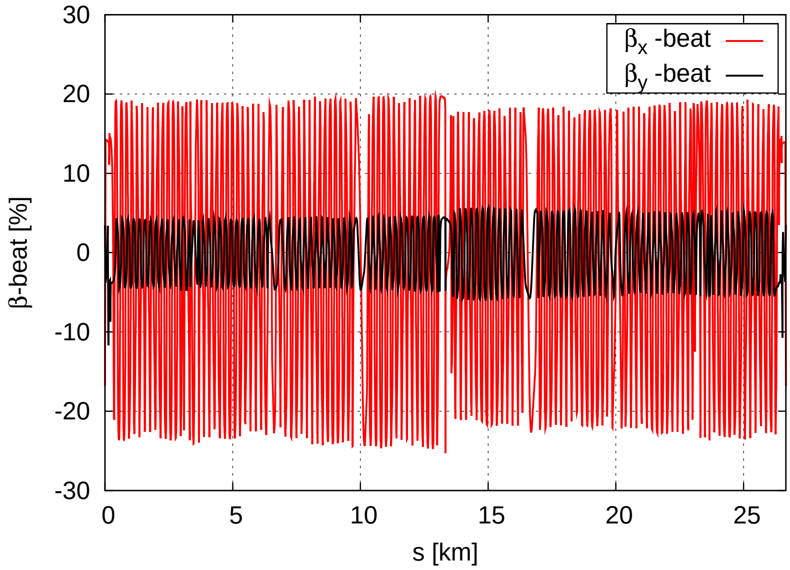

Figure 5.9: Off-momentum beta-beat of the LHC with the new IR optics in IR1, for $\delta = 3.3 \times 10^{-4}$.

may be excited. In order to study the β-beat due to the new chromatic correction scheme without the influence of the new working point, the tune values must be changed. To do so, the trim quadrupoles of the arcs could be recomputed, but this may affect the performance of the chromatic correction. To make the latter comparable to the one of the nominal LHC, the phase advance between sextupoles in the arcs is kept unchanged, and instead the tune adjustment has been performed by a rotation matrix located in IP5. The tune was changed from $(Q_x, Q_y) = (65.28, 60.40)$ to $(65.31, 60.32)$. The resulting off-momentum β-beat is shown in Fig. 5.9, illustrating the proper correction of the geometric aberrations. The fact that β_x-beat is bigger than the β_y-beat reflects the positive effect of the local chromatic correction, that takes place in the vertical plane only.

5.3.3 Tracking Simulations

Tracking simulations were performed with the interaction region fully matched to the ring. In the simulations presented, a particle tracking was done with a grid of particles with initial values ranging $x = [\sigma_x, 20\sigma_x]$ and $y = [\sigma_y, 10\sigma_y]$ and relative momentum deviation $\delta = 3\sigma_\delta$. The energy offset allows checking the effectiveness of the chromatic correction, and the particles at different initial positions draw a map of the aberration cancellation. The larger the initial amplitude is, the stronger the aberration gets and the more sensitive the motion becomes to a given error in phase advance.

The result of the simulations after 10^3 turns is shown in Fig. 5.10. The black dots represent the initial positions of particles that survived. Fig. 5.11 shows the corresponding result for 10^4 turns. No limitation was found for the horizontal plane up to $20\sigma_x$, but vertically particles are lost from about 6–7σ_y.

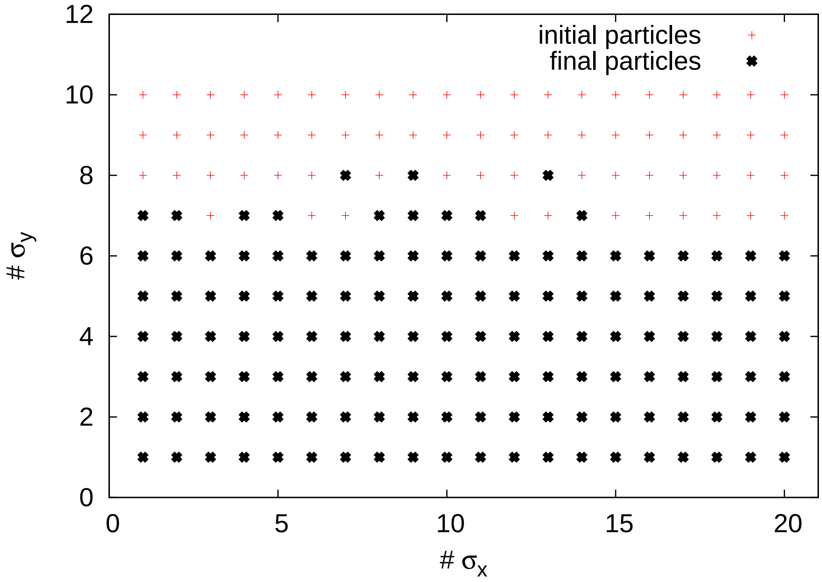

Figure 5.10: Survival plot for 10^3 turns at $\delta = 3\sigma_\delta$.

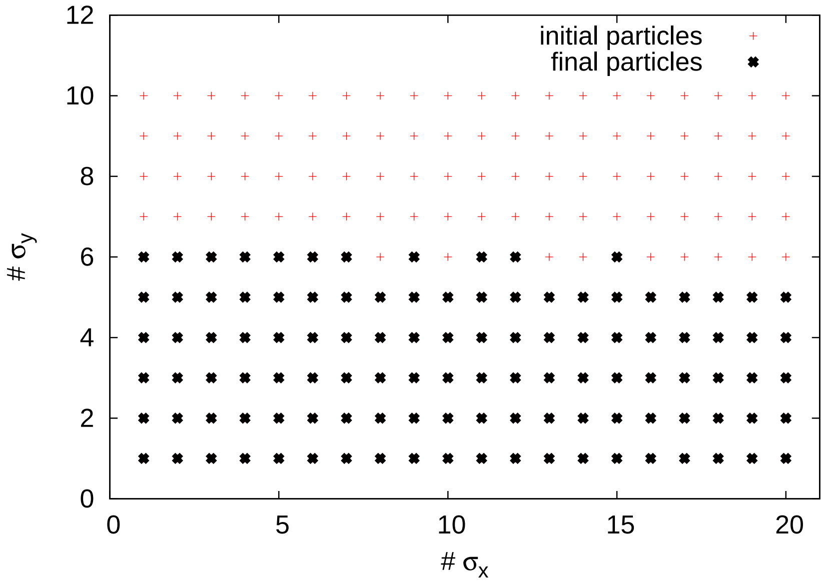

Figure 5.11: Survival plot for 10^4 turns at $\delta = 3\sigma_\delta$.

5.4 Non-Colliding Optics

5.4.1 Injection Optics

Due to the adiabatic damping, the geometric emittance at injection energy is much larger than at collision. As explained in Sec. 2.2.3, in order to provide sufficient aperture at injection, $\beta^*_{x,y}$ must be enlarged. The difficulty here, besides matching the new $\beta^*_{x,y}$ to the arc, is to maintain the local chromatic correction. As there are no collisions, the crab-waist sextupoles are switched off and the constraints on the phase advance are more relaxed than for the collision optics.

In principle, a local chromatic correction is not needed at injection energy, due to the low values of the betatron functions. If the chromaticity can be corrected in the arcs, there is another restriction less. However, for the DHQ, the sextupolar component is there even if not needed, and it generates aberrations that must be compensated, so there are still requirements on the compensator sextupole. In addition, between the injection and collision optics, a set of optics should be produced to make the transition, as discussed in Sec. 3.2.1.

In order to choose the values of $\beta^*_{x,y}$, we have to consider the most limiting factor: the maximum β_y in the DHQ at injection energy. From (1.71), the emittance at injection is enlarged from its value at collision at the same ratio as that of their respective energies, (7000 GeV)/(450 GeV)≈ 15.55. In order to prevent the injection beam size in the DHQ from being bigger than in collision, the maximum β_y should be reduced by the same factor, so $\beta_{MAX;y}(DHQ) = 1350$ m.

Regarding β_x, it should pass from 520 m at the exit of the DHQ at collision energy to 35 m at injection, but in principle this restriction is not as tight as the other one, if the DHQ is built in a segmented way with larger horizontal aperture at the end of the element.

In principle, preserving the same β_y^*/β_x^* should help in requiring the same transfer matrix between the DHQ and the compensator sextupole without changing the relative strength of the quadrupoles within the region between those elements. We have to make minor adjustments only to the phase advances. However, the aperture radius proposed in Table 5.2, would not be sufficient, instead we should use the values in Table 5.5. For the worst case, that of collision energy, the peak fields are still reasonable. Their values are far below 9 T and in principle we should be able to use superconducting magnets with NbTi technology. The proposed injection optics features $\beta_x^*/\beta_y^* = 55$ m/55 cm and is presented in Fig. 5.12.

Table 5.5: Revised parameters of the final-focus double aperture quadrupoles for the injection optics of the second design: aperture radius, gradient for injection and collision energy; and maximum magnetic field in the coil. The radius is computed as 11max(σ_x,σ_y)+5 mm, with $\epsilon_N = 2.4\ \mu m$, and the maximum magnetic field in coil as $|B_p| = gr$.

		Injection energy	Collision energy	
	r [mm]	g [T/m]	g [T/m]	$\lvert B_M\rvert$ [T]
quad.2	29.2	15.4	240	7.0
quad.3	18.1	-16.7	−260	4.7
quad.4	23.8	17.9	278	6.6

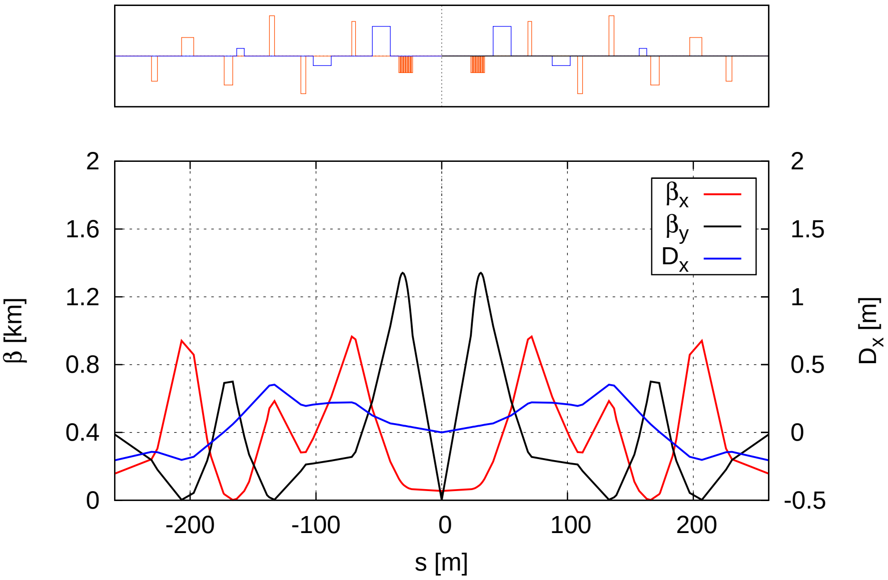

Figure 5.12: injection optics with $\beta_x^*/\beta_y^* = 55$ m/55 cm.

5.4.2 Beam Separation

In the LHC, just after the acceleration process is finished and all the superconducting magnets have been ramped up, the beams are not yet in collision, but they are separated through the IP orbit bumps. The center of the beams is separated by 1 mm. The crossing in IR1 and IR5 is realized in different orthogonal planes. The separation is done in the plane opposite to the crossing plane. That is, the separation is done in the horizontal plane in IR1 and vertically in IR5.

In the presented interaction region, both crossings occur in the same (horizontal) plane, and the non-colliding beam separation must be established in the vertical plane in both cases. For this purpose, bumps similar to those in the present LHC can be used.

5.5 Conclusions

- A new IR design has been completed with $\beta_x^* = 3.5$ m, $\beta_x^* = 3.5$ cm and $\theta = 2.6$ mrad. For this reduced crossing angle, the DHQ has been rescaled and its multipole components estimated. The new IR optics has been fully matched to the ring.

- This conceptual IR design could boost the LHC luminosity by an order of magnitude, making use of the available high brightness beams by means of a large Piwinski angle.

- The new design includes a place for a compensator sextupole (sext.3) on each IP side. It fulfills the conditions on phase advance $\Delta\mu_{x,y} = \pi$ from the center of the DHQ with sufficient accuracy (the error is 5 orders of magnitude smaller than in the first design). In addition, relations (1.68) and (1.69) are fulfilled from the center of the DHQ. Finally, the dispersion is zero at the location of sext.3. The high chromaticity has been successfully corrected with the new IR installed in one of the two luminosity experiments.

- The bottleneck of this design is the DHQ. A solution involving such a large element is very challenging, but the DHQ could be substituted by a DHQ+quadrupole, with a bending magnet in the middle. Another solution would be a new design of the DHQ with higher quadrupole gradient and less sextupolar component at the position of the beams.

- The required strength of the compensator sextupole is excessive, but a more developed design of the DHQ with reduced g_s at $x = \pm\Delta_{beam}/2$ could also improve the vertical dynamic aperture. Also, choosing a different working point in the tune diagram, away from the third-order resonance line, could further improve the dynamic aperture.

- Finally, some solutions related to the non-colliding injection optics have been proposed.

6. Future Colliders in the LHC Tunnel

The tunnel that hosts the LHC was built for the previous e^+e^- collider, LEP [16], that ran from 1989 to 2000, including its upgrade, LEP2. This 26.7-km tunnel still has the potential to serve for new accelerators after LHC and HL-LHC commissioning. In this chapter two such potential accelerators are commented. The first one is a new lepton collider to study the Higgs boson, that is, a Higgs factory, and called LEP3; the second one, a proton collider (either pp or $p\bar{p}$) at high energy, called HE-LHC. We discuss the possibility of applying to the HE-LHC a collision scheme similar to the one described in Chapter 4 and Chapter 5, including simulations that investigate the potential benefit of this scheme.

6.1 A New Circular e^+e^- Collider: LEP3

LEP3 is a proposed e^+e^- circular collider with a E_{cm} of up to 240 GeV. A circular lepton collider has the drawback of a high synchrotron emission, which prevents it from reaching as high an energy as its counterpart linear colliders: CLIC and ILC, without an excessive energy demand on the accelerating system for the compensation of the SR losses.

However, the discovery of a Higgs boson, with a mass of 126 GeV/c^2, has launched again the idea of a circular collider for the study of the properties of the new object, as not so much energy is needed for this purpose. This is why a circular collider is still able to cope with the SR radiation at this energy, emerging as an interesting option instead of a linear collider, as it can run at much higher luminosity. The first design considerations for such future circular collider are reported in [21].

The use of crab-waist collisions could be considered as an interesting solution [75]; in fact, lepton machines are the natural place for this collision scheme. However, a recent study does not recommend its use, as its effects would be diluted due to the fact that LEP3 is a beamstrahlung dominated machine [76].

6.2 A Higher Energy Proton Collider: HE-LHC

Present LHC arc bending magnets are designed for an operational magnetic field of $B = 8.33$ T, which is limited by the critical field of the superconducting material used for the coils: NbTi. Another technology must be used to operate at higher magnetic fields and to bend particles that will circulate at a higher energy. It is likely that the superconducting magnet technology will improve in order to provide a magnetic field of 20 T [77, 78], though even the more recent and advanced Nb_3Sn-cables are not able to provide a field above 16 T. An interesting option could be the use of high temperature superconducting materials. The required magnetic field would be a factor 2.4 larger than the present LHC field. Assuming the same length for the future bending magnets, the energy could be increased by the same factor, opening the possibility of having collisions at $E_{cm} = 33$ TeV. The bases of this new project were examined on [79, 80].

Following the relation (1.109), the power of the emitted synchrotron radiation would be $(33\text{ TeV}/14\text{ TeV})^4 \sim 31$ times that of LHC, and it would have remarkable effects on beam operation. Damping times in lepton rings are of the order of milliseconds, while in past hadron rings including the LHC, they are of the order of several hours, more than a run time. HE-LHC has damping times on the order of the run time or smaller, and this causes the beam sizes to shrink during beam operation. This is a totally new phenomenon in a hadron collider arising from its very high energy.

The VHE-LHC in a new 80–100 km tunnel would be another candidate for a future high energy proton collider, that could use synergies with TLEP, by making use of the same tunnel after operation. The higher radius would enable collisions at $E_{cm} = 100$ TeV.

The objective of this chapter is to explore the application of the concept described in Chapter 4 and Chapter 5, that is, a local chromatic correction that would allow for crab-waist collisions, for one of these high energy colliders. It was decided to perform the study for the HE-LHC and not for the VHE-LHC, because the design of this second machine has many more uncertainties, like the geometry of the ring that determines the length of each section. Arcs, long straight sections and dispersion suppressors are already known for the HE-LHC, as their layout is identical to that of the LHC (Fig. 2.1). The emphasis is not put on the optics design, but on the exploration of different possible initial beam parameters compatible with the technology, with the objective of simulating their dynamic behaviour.

6.2.1 Starting Point

We assume that the optics in the arcs is identical to that of the present LHC, which means stronger quadrupoles magnets in order to get the same normalized quadrupolar strengths. We also assume that the HE-LHC would run with two experiments (IR1 & IR5) that would use the existing caverns, hence the free length being the same ($L^* = 23$ m). The bunch separation is taken to be 50 ns, so that the total number of bunches would be $n_b = 1404$.

Regarding the peak luminosity, it had arbitrarily been decided to have the same value as for HL-LHC, namely $L_{peak} = 5 \times 10^{34}\text{cm}^{-2}\text{s}^{-1}$. In principle this seems to be a conservative value, but one has to consider that the energy is a factor 2.4 higher. First of all, the inelastic cross section is larger at this energy, increasing from 85 to 93 mb, which would create a slightly larger number of events. Secondly, the total number of bunches is halved, creating a larger luminosity per single bunch crossing (L_{sc}). These two conditions determine a total of $L_{sc}\sigma_p = L_{peak}\sigma_p/(f n_b) = 295$ events per bunch crossing [81, Sec. 7.3.5]. One reason for not going to higher luminosities is the limit on the tolerable radiation levels in the IR.

6.2.2 A Special Proton Storage Ring

The short damping times produce a significant emittance reduction. By substituting (1.110) in (1.83) we get the beam size evolutions:

$$\sigma_x(t) = \sigma_{0,x}e^{-t/2\tau_x}, \qquad \sigma_y(t) = \sigma_{0,y}e^{-t/2\tau_y}, \qquad \sigma_s(t) = \sigma_{0,s}e^{-t/2\tau_s}. \tag{6.1}$$

The time constants (τ_x, τ_y, τ_s) give time evolution only under influence of SR damping. But the effect of the intra beam scattering (IBS) introduces another contribution, that is expressed in the form of additional exponential time parameters: ($\tau_{IBS,x}, \tau_{IBS,y}, \tau_{IBS,s}$). These parameters have an opposite sign to the SR damping ones. so that the total time constants are modified as

$$\left(\frac{1}{\tau_x}, \frac{1}{\tau_y}, \frac{1}{\tau_s}\right) \to \left(\frac{1}{\tau_x}, \frac{1}{\tau_y}, \frac{1}{\tau_s}\right) - \left(\frac{1}{\tau_{IBS,x}(s)}, \frac{1}{\tau_{IBS,y}(s)}, \frac{1}{\tau_{IBS,s}(s)}\right). \tag{6.2}$$

The difference of the IBS time parameters with respect to the SR constants is that while the last ones are in principle constant over time, the set of τ_{IBS} depends in general of time, so that the evolution in (6.1)

has no longer a pure exponential dependence if the effect of the intra-beam scattering is considered. The reasons for this time-dependence are many. Just to mention one, as the number of particles decreases due to the particle burn-off, the probability of scattering is inferior and this mechanism becomes weaker.

During a run, the number of particles reduces due to burn-off, contributing to the reduction of luminosity. This always happens if all the other parameters are constant, for example, if there is no luminosity levelling. But a look at (1.77) shows that a reduction on $\sigma_x^*\sigma_y^*$ is beneficial for the luminosity, helping to compensate the luminosity loss due to burn-off or even provide a positive slope on the luminosity during a time interval ($dL/dt > 0$).

On the other hand, the evolution of the Piwinski angle is obtained by substituting (6.1) in (1.78), where a horizontal crossing is assumed:

$$\phi(t) = \frac{\theta}{2}\frac{\sigma_s(t)}{\sigma_x(t)} = \frac{\theta}{2}\frac{\sigma_{0,s}}{\sigma_{0,x}} \cdot exp\left[-\frac{t}{2\tau_s(s)} + \frac{t}{2\tau_x(s)}\right]. \tag{6.3}$$

This relation can also be expressed as

$$\phi(t) = \phi_0 e^{-t/2\tau_\phi(s)}, \tag{6.4}$$

with

$$\phi_0 = \frac{\theta\sigma_{0,s}}{2\sigma_{0,x}}, \qquad \frac{1}{\tau_\phi(s)} = \frac{1}{\tau_s(s)} - \frac{1}{\tau_x(s)}. \tag{6.5}$$

From (6.4) we get that the Piwinski angle decreases with time. This effect can be profitable for the luminosity through the geometric luminosity reduction factor. However, there is an inconvenience for the nominal parameters of the HE-LHC ($\beta^*_{x,y} = 0.35$ m). The decrease of both ϕ and the normalized emittance ϵ_N, can result in the total tune shift (1.106) to increase above the tolerable value of $\xi_{x,y} = 0.01$. An emittance blow up must then be introduced by means of a noise injection [82] in order keep the tune shifts under the limit, that is, $\xi_{x,y} \leq 0.01$). This procedure introduces an additional beam size increase that reduces the potential positive effects from the SR emission. In fact, a limitation on the tune shift limits the luminosity gain from the tune shift (1.107). More details on the blow up of the emittance for the HE-LHC can be found in [81, Appendix C] and [83].

6.3 A Symmetric IR for the HE-LHC

Here we apply the idea of having crab-waist collisions and a local chromatic correction with a large crossing angle to the HE-LHC IR. As for the proposed IR in Chapter 4 and Chapter 5, the lower β^*_y allowed by the large Piwinski angle creates a large beam divergence, so that the IR optics would be "symmetric Beam 1/Beam 2" and "symmetric left/right". In principle, we consider the case of a pp collider, where for a symmetric optics, opposite fields must be created for each beam.

There would be two possibilities. The first one would be to keep an antisymmetric optics in the arc quadrupoles, where the gradient for both beams in each element is identical. Then, we would have to match the symmetric IR optics to the antisymmetric arc optics, as it is proposed for the LHC in Chapter 4 and this would have drawbacks similar to those pointed out in Sec. 4.4. However, as the machine is to be built from zero and all the magnets will be designed only for the purpose of this new machine, it would make more sense to make the optics symmetric in the whole ring. Then, all the quadrupoles, including those in the arcs, should have opposite magnetic field distribution for each beam (4.5).

Regarding the interaction region, a scheme similar to the one proposed in Chapter 4 and illustrated in Fig. 4.3 is proposed. In both cases, a vertical focalizing element for both beams in the first quadrupole should be used. Two options for this element emerge, depending on the crossing angle:

- $\theta = 2$ mrad: For this crossing angle, a double-half quadrupole, like the one shown in Sec. 4.2 is proposed, since the beam separation, $\Delta_{beam} = 46$ mm, is not enough for a double-aperture focusing element.
- $\theta = 8$ mrad: In that case the beam separation ($\Delta_{beam} = 184$ mm) would allow for separated apertures.

For the second case, a double-aperture quadrupole with this beam separation has been designed and whose cross section is shown in Fig. 6.1. The color scale on the left side represents the longitudinal component of the magnetic vector potential which is related with the magnetic field as $\boldsymbol{B} = \nabla \times \boldsymbol{A}$. This can be compared to a quadrupole presenting an opposite sign gradient

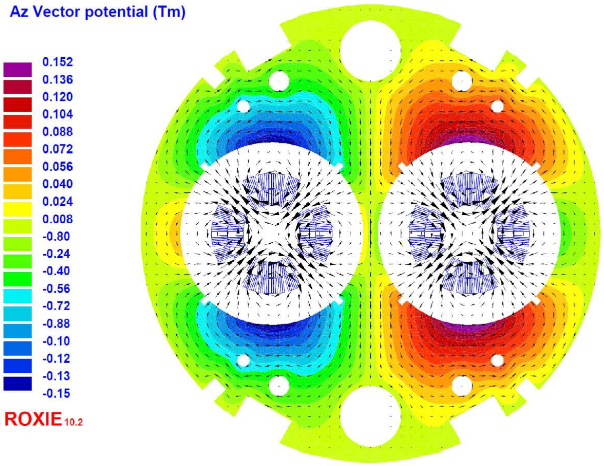

Figure 6.1: Cross section of a double-aperture quadrupole magnet with opposite sign gradient in the apertures, $|g| = 219$ T/m. The beam separation (distance between the centers of the two apertures) is Δ_{beam} = 184 mm.

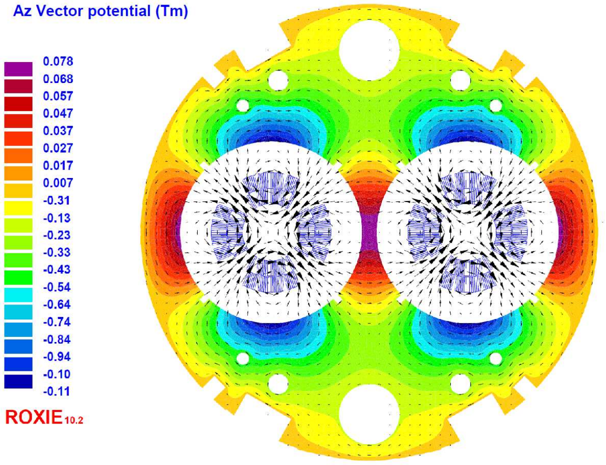

Figure 6.2: Cross section of a double-aperture quadrupole magnet with identical gradient in both apertures, $|g| = 220$ T/m. The beam separation is Δ_{beam} = 184 mm.

(like those of the present LHC arcs) illustrated in Fig. 6.2. In principle the latter presents a better use of the coil current to generate a gradient. Indeed, Fig. 6.1 shows more field lines into the yoke than Fig. 6.2. However, with a separation of 184 mm (10 mm less than in the LHC arc quadrupoles), there is scarcely a 0.45 % drop on the field gradient.

Table 6.1 compares the parameters for the two options. In both cases the respective values of the β-functions at the IP are identical, and chosen so as to have a beam size ratio of 10 with the same initial emittance in the two planes, implying ($\beta_x^*/\beta_y^* = 100$). The number of particles per bunch has been computed in order to have the same peak luminosity, but the initial luminosity is different for each case.

Table 6.1: HE-LHC Optics and beam parameters for the two options presented. The subindex '0' refers to the initial values of the respective variable.

	$\theta = 2$ mrad	$\theta = 8$ mrad
technology for first element	double-half quad.	double-aperture quad.
β_x^*, β_y^* [m]	3, 0.03	
$\epsilon_{N,0}$ [μm]	2.1	
$\sigma_{0,x}^*$, $\sigma_{0,y}^*$ [μm]	19, 1.9	
n_b	1404	
θ [mrad]	2	8
Δ_{beam} [mm]	46	184
ϕ_0 [rad]	4.1	16.3
$l_{OA;0}$ [cm]	2	0.5
$\xi_{0,x}$, $\xi_{0,y}$ [10^{-3}]	3.2, 1.3	0.3, 0.4
$\xi_{peak,x}$, $\xi_{peak,y}$ [10^{-3}]	8.9, 2.4	1.1, 1.2
Δ_{in} [σ_x]	317	12680
L_0 [10^{34} cm^{-2}s^{-1}]	2.3	2
L_{peak} [10^{34} cm^{-2}s^{-1}]	4.9	4.9
N [10^{11}]	2.45	3.05

6.3.1 Parameter Evolution

Some simulations of the dynamic behaviour for different parameters have been performed with the help of the code HALO [81, Appendix C] for the two options presented in Table 6.1.

Figure 6.3 represents the evolution of the transverse beam size in the two planes and for the two options considered. After a certain time, the beam sizes for the case of 8-mrad crossing angle are larger than the corresponding ones for $\theta = 2$ mrad. This is due to the shorter damping times as a consequence of the denser bunches for the case of the larger crossing angle, as more intra beam collisions are produced. The vertical beam sizes always exhibit a decreasing behaviour while the horizontal ones are characterized by three regions, a decreasing, an increasing and a decreasing branch. The reason for this difference between the

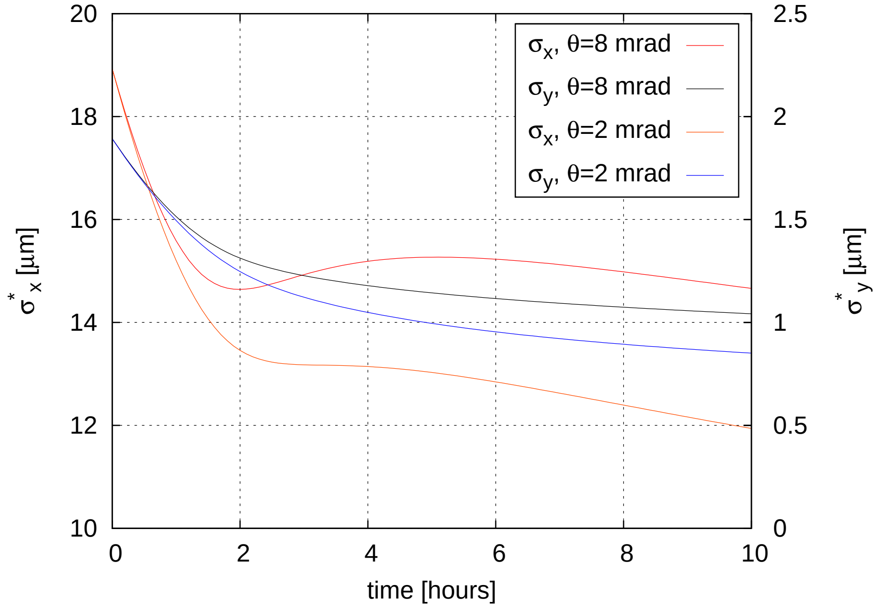

Figure 6.3: Transverse beam size evolutions for the two crossing angles.

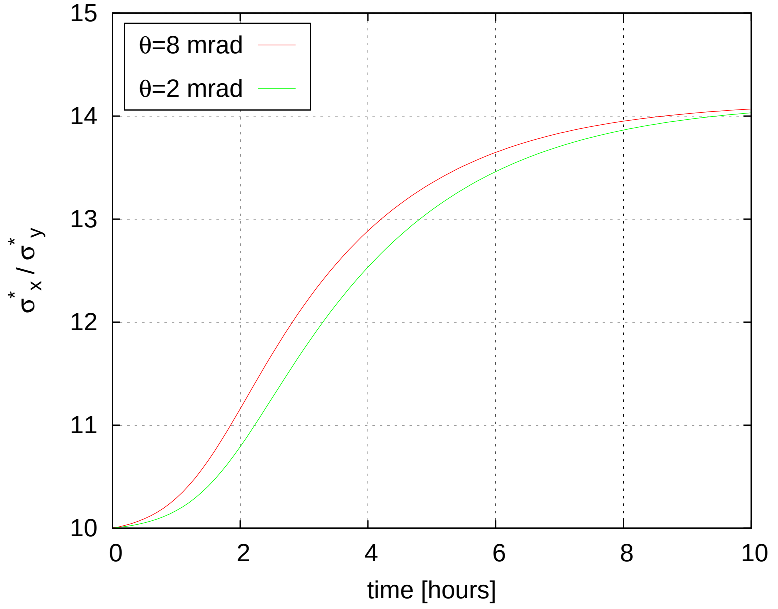

Figure 6.4: Evolution of the beam size ratio.

two planes is that the IBS rise times are shorter in the horizontal plane. The second increasing region for the horizontal beam size is due to the decrease in the longitudinal beam size. All of this results in a σ^*-ratio which varies over time, as Fig. 6.4 shows. It starts with a value of 10, to fulfilling the requirement for crab-waist collisions (3.16), but it increases up to 14 at a later time. To be more precise, after approximately 3 hours of operation the ratio has already exceeded the value 12. This suggests that the relation (3.16) could be relaxed at the beginning, which could ease the optics and make the general design more feasible. Then, the initial value of (σ_x^*/σ_y^*) should be determined by simulations as well as the tolerable run time, also examining the time needed for the beam size ratio to approach the value of 10. All of this study should help determining the integrated luminosity.

The longitudinal beam size evolution is represented in Fig. 6.5 together with that of the Piwinski angle. Both quantities are decreasing with time. The fact that the Piwinski angle is decreasing was commented upon in Sec. 6.2.2.

The instantaneous luminosity is shown in Fig. 6.6. The initial luminosity is bigger for the double-half quadrupole as the final element (smaller crossing angle). The reason is the influence of the crossing angle on the geometric luminosity reduction factor. However, it should be noted that after two hours, the other case shows superior luminosity, due to the longer lifetime which is a consequence of the larger initial number of particles. Here the difference between the initial and the peak luminosity becomes noticeable. This difference makes the choice of parameters for a given L_{peak} more complicated, as it requires simulations to know the integrated luminosity for each parameter configuration. In addition, the optimum run times (T_R) are also indicated in the plot.

These times have been computed by optimizing L_{int} over a run time. The optimum run time and the optimum integrated luminosity are given by the following relations:

$$\left[\frac{d}{dT_r}\left(\frac{L_{int}(T_r)}{T_p+T_r}\right)\right]_{T_r=T_R}=0, \qquad L_{int,opt}=L_{int}(T_r)|_{T_r=T_R}; \tag{6.6}$$

where T_p, the turnaround time, represents the preparation time for each fill, that is, the time between the end of a physics run and the beginning of the next one. We have assumed $T_p = 5$ h.

The last simulation plot in Fig. 6.7 shows the total tune shift in both planes considering the two interaction points. That is, they correspond to $2\xi_{x,y}$ as the crossing is in the same plane (the horizontal one) for the two IPs. The parameters ξ_x and ξ_y were computed as defined in (1.101) and (1.102), respectively. There are three contributions to the tune shifts: number of particles, emittances and Piwinski angle. In all the cases considered the tune shift increases initially with time as a consequence of the $\sigma^*_{x,y}$ decrease, but after a certain time it decreases, as the decrease of N due to the burn off becomes stronger. Anyway, the peak values are extremely low compared with other colliders, or with the baseline option for the HE-LHC, where the design conservative tune shift is 0.01. Different from the baseline case, an artificial emittance blow-up is not necessary. Here the effect of the large crossing angles is visible, according to (1.105) there is no luminosity limitation from the beam-beam tune shift, allowing to translate the ξ_y increase during the store into a luminosity increase.

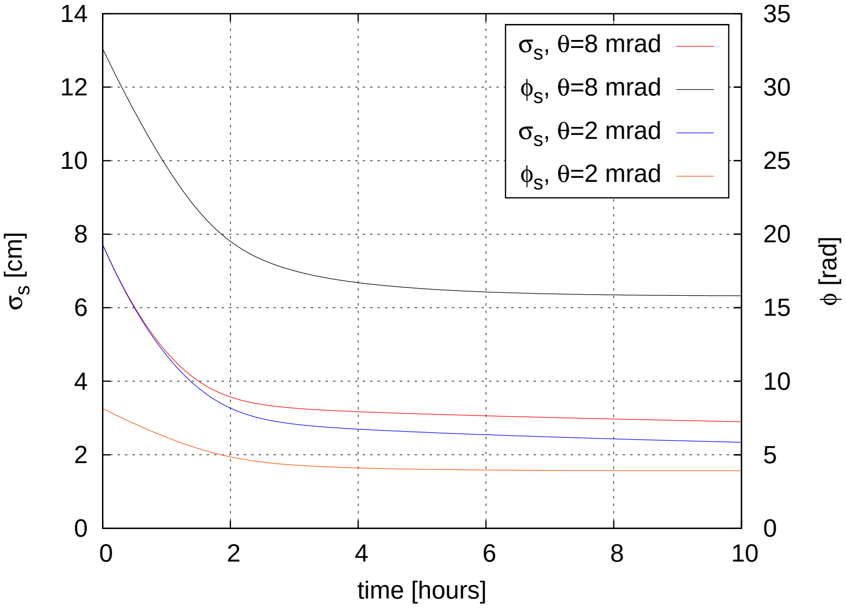

Figure 6.5: Longitudinal beam size and Piwinski angle evolutions.

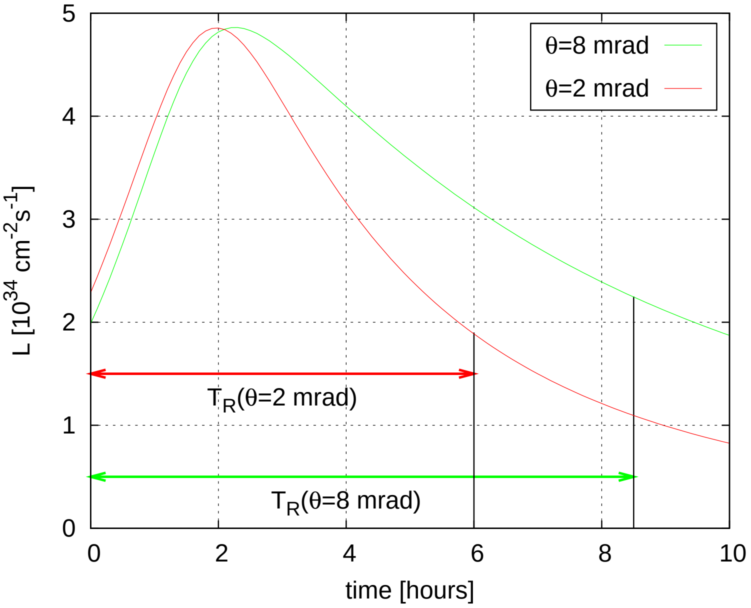

Figure 6.6: Luminosity evolution. T_R represents the optimum run time for the two crossing angles assuming a turnaround time $t_p = 5$ h. The integrated luminosities per run are $L_{int} = 0.75$ fb^{-1} and 1.08 fb^{-1}.

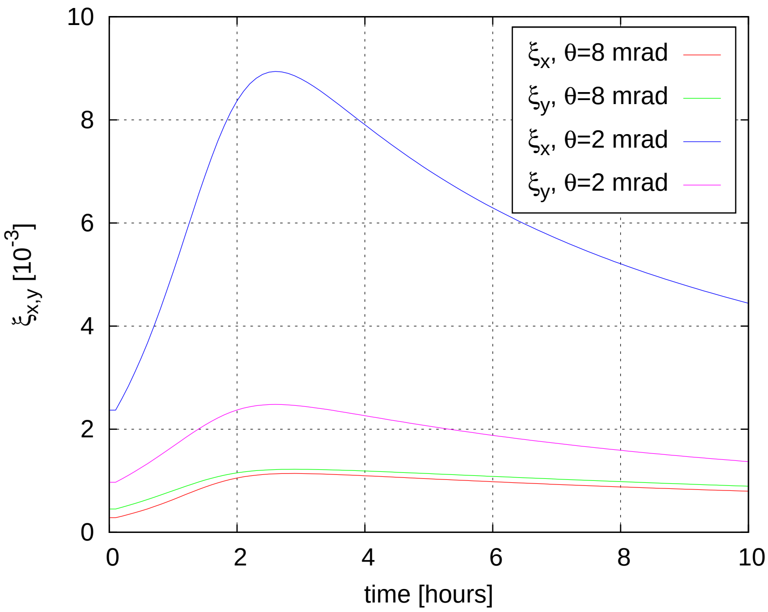

Figure 6.7: Tune shifts for the two crossing angles.

Finally, the results from all the simulations are summarized in Table 6.2, where the optimum integrated luminosity per day has been computed as

$$L_{int,opt,day} = L_{int,opt}\,\frac{24\ h.}{T_R + T_p}, \tag{6.7}$$

where the IBS growth times refer to the initial state as they vary over time.

Table 6.2: SR Damping times, IBS damping times, luminosity lifetime (τ), optimum run time and optimum daily luminosity. $\tau_{SR;x,y,s}$ refer to the initial values.

	$\theta = 2$ mrad	$\theta = 8$ mrad
$\tau_{SR;s}$ [h]	1.01	
$\tau_{SR;x,y}$ [h]	2.02	
$\tau_{IBS;x}$ [h]	37.5	21.1
$\tau_{IBS;y}$ [h]	72.0	42.2
$\tau_{IBS;s}$ [h]	72.4	40.7
τ [h]	14.6	29.9
T_R [h]	6	8.5
$L_{int,opt,day}$ [fb^{-1}]	1.63	1.93

6.3.2 HE-LHC as a Proton-Antiproton Collider

The advantage of colliding particles of opposite sign is that $(q\boldsymbol{v})$ has the same sign for the two beams, and the same field distribution (B_x, B_y) can be used for the two beams to create an identical optics. The arc optics would rely on double-aperture quadrupoles identical to the LHC ones, but the optics would now fulfill the properties (2.1), (2.2), (2.3) and (2.4).

Most importantly, a DHQ is no longer necessary to accomplish the same k for the two beams in the same aperture, and for the first element in the IR, a standard quadrupole with common aperture can be used, like those used in present LHC. This is why this option would be very powerful in case HE-LHC is to be built as a $p\bar{p}$ collider [84]. Regarding the bending magnets, they should present the same field distribution, and this would mean that the effect of the weak focusing is the same for both beams. It should be noted that from the optics point of view this option would be the most interesting, and would produce equivalent physics results to a pp collider. However, the luminosity would be considerably reduced due to the difficulty to produce highly populated bunches of antiprotons [85].

6.4 Conclusions

- An extremely-flat beam optics ($\beta_x^*/\beta_y^* = 100$) is conceptually possible for the HE-LHC, with large Piwinski angle, local chromatic correction and the possibility to have crab-waist collisions that can increase luminosity and suppress resonances.

- The large crossing angle allows for a drastic reduction of the tune shifts, removing the need for an emittance blow up. It can accept beams of higher brightness to increase the integrated luminosity.

- The short SR damping times makes it necessary to study the time evolution of the parameters. Their influence on the beam size can be profitable for the overall integrated luminosity.

- If the collider were a $p\bar{p}$ collider, a symmetric optics Beam 1/ Beam 2 would be implemented in an easy way: the final focus could be built with pure quadrupoles and common aperture for both beams.

7. Final-Focus System for the LHeC

This chapter summarizes the LHeC project and the layout of its interaction region. It contains the design work for a new final-focus system of the electron line, comparing different options. In particular, an optics with unequal β-functions in the two planes and local chromatic correction.

7.1 The LHeC

The ECFA-CERN-NuPECC design study for a Large Hadron electron Collider (LHeC) [11] based on the LHC, considers two options for the electron line, either installing a ring accelerator, similar to LEP, on top of the LHC or adding a linear accelerator tangential to the LHC. For the latter, two options are contemplated. The first is a 60-GeV energy recovery linac (ERL) operating in continuous wave that can offer an electron-proton luminosity of 10^{33} cm^{-2} s^{-1}. The second, a pulsed 140-GeV linac without energy recovery, offering a luminosity of 1.4×10^{31} cm^{-2} s^{-1}. The option explored here is the 60-GeV ERL, that is sketched in Fig. 7.1.

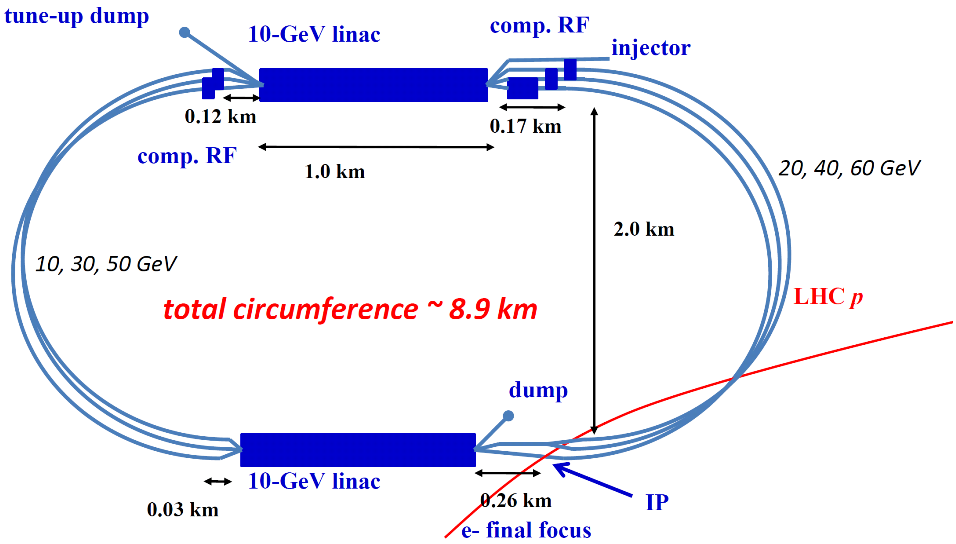

Figure 7.1: Schematic layout of the LHeC ERL. Courtesy of the LHeC study group.

The infrastructure of the electron linac is separate and fully decoupled from the LHC operation, including LHC upgrades (e.g., HL-LHC and HE-LHC), with the exception of the interaction region.

A possible configuration in LHC IR2 is to transport the electrons in the same direction as the LHC Beam 1 and collide them head-on with Beam 2 only (see Fig. 7.2), so that proton Beam 1 does not suffer any collision in the LHeC IP. The beam sizes of protons and electrons are matched at the IP, $\sigma_p^* = \sigma_e^*$, and as the geometrical emittance is supposed to be the same, β^* has the same value for the two particle beams. To comply with the high luminosity requirements, the proton β-function at the IP must be smaller than in the LHC pp high luminosity insertions. Specifically, we choose $\beta^* = 0.1$ m. This is a very challenging value for the LHC protons, as it has been proven in this thesis work, but it can be achieved by reducing the free length, L_p^*, from 23 to 10 m and squeezing the colliding beam only.

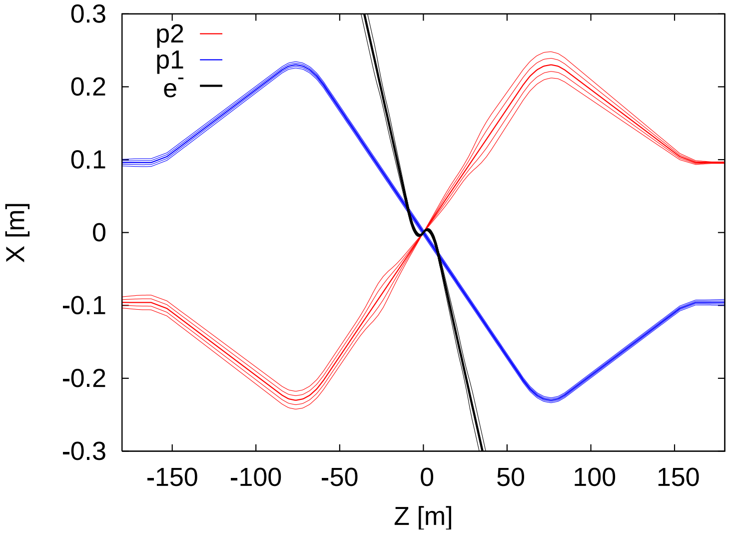

Figure 7.2: LHeC IR, showing the trajectories in the colliding proton beam (p2), the non-colliding proton beam (p1) and the electron beam trajectories with their 5-σ_x and 10-σ_x envelopes. Courtesy of Dr. Rogelio Tomás.

7.2 Interaction Region Layout

The free length for electrons should be much larger than for protons ($L_e^* = 30$ m), in order to provide enough separation between the final quadrupoles for the protons and leptons. However, the magnetic rigidity for electrons is much lower here than for the protons, ($(p/q)_e \sim 0.2 \times 10^3$ T·m, $(p/q)_p \sim 23 \times 10^3$ T·m), so that this β^* should not be a difficult issue, even though the free length is much longer than for the protons, $L_e^* \gg L_p^*$. The electrons will pass through the first proton quadrupole, Q1, in a special region without magnetic field, as indicated in Fig. 7.3.

The electron and proton beams need to be separated by 7 cm to enter through their respective holes in Q1 at $s = 10$ m, a zone with high field gradient for protons and a field-free region for electrons. However, the required crossing angle would be too large, inducing a

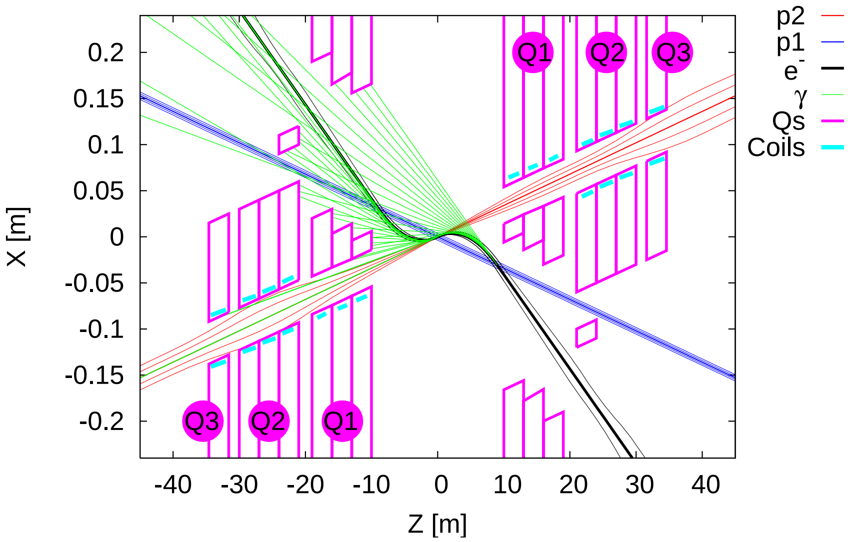

Figure 7.3: LHeC IR with a schematic view of the synchrotron radiation. The parameters of the Q1 and Q2 segments correspond to the magnets of Fig. 7.4. Only the colliding proton beam passes through the triplet. The electron beam passes through the field-free region of Q1. Courtesy of Dr. Rogelio Tomás.

substantial luminosity degradation through the geometric luminosity reduction factor. The solution is to include detector-integrated dipoles of 0.3 T over a length of ±9 m around the IP, so that the beam separation can be accomplished with a zero crossing angle. The 7-cm separation is compatible with a mirror quadrupole design for Q1 based on Nb_3Sn technology, that is presented in Fig. 7.4.

The proton beam-beam tune shift is not a limitation here. It is of the order of 10^{-4}, much lower than that of the high luminosity insertions, so this contribution to the total tune shift is negligible. This is due to the low charge of the electron bunches.

7.3 Optics

Some preliminary computations have shown that the total chromaticity for the proton triplet is too high. It amounts to 960 units from the two IP sides [68], and therefore requires a dedicated chromatic correction section. For the non-colliding beam (Beam 1), the LHC "alignment optics" was chosen as the starting point [86]. This beam passes through the field-free region of magnets Q1 and Q2.

There are some limitations for the final focus. Apart from constraints on the aperture, magnet strength limitations, and SR power loss, there is an important limitation in length. About 200 m are available for the electron final-focus system between the exit of the linac and the IP of which at least 40 m should be kept for collimation and beam diagnostics. Respecting this constraint, together with $L_e^* = 30$ m, three alternative final-focus optics for the electron beam have been developed. They are compared next. An electron normalized emittance of 50 μm is assumed.

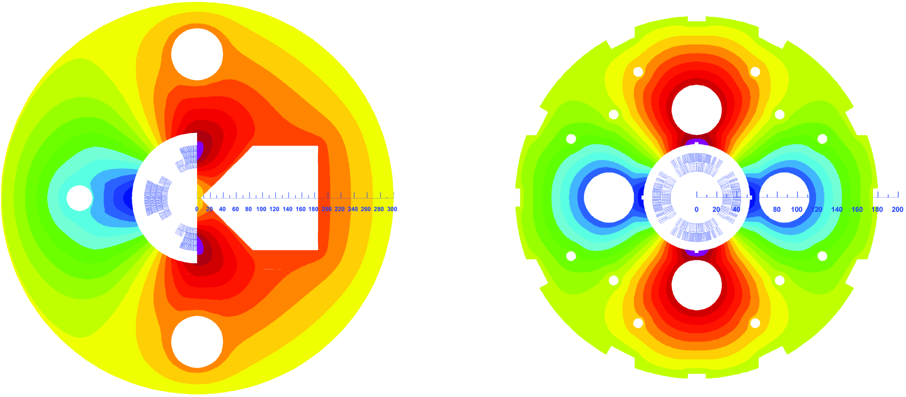

Figure 7.4: Left: Q1, half quadrupole with field-free region. Beam 2 of the LHC passes on the left hand side of the mirror plate, through a region with a quadrupolar field. The electrons and the non-colliding proton beam travel on the right hand side of the mirror plate in a quasi field-free region. Right: Q2, single aperture quadrupole. Courtesy of Dr. Stephan Russenschuck.

Table 7.1 presents the parameters for the quadrupole magnets of the triplet and the two doublet optics. An estimation of the aperture radius is made by imposing a requirement of 11σ in each plane plus an additional margin of 5 mm. In the doublet solution the third and fourth quadrupole, Q3 and Q4, are located further upstream. In that case, the beam sizes at the IP are modified, in order to have different beam divergence in the two planes and to perform the chromatic correction. Instead of $\beta^*_{e;x,y} = 0.1$ m, as in the triplet, the different doublet optics feature $\beta^*_{e;x} = 0.2$ m and $\beta^*_{e;y} = 0.05$ m, which leads to a beam size aspect ratio of 2. In that case we assume that the optics of the two colliding beams is matched, so that $\beta^*_{p;x} = 0.2$ m and $\beta^*_{p;y} = 0.05$ m.

Table 7.1: Final electron quadrupole parameters for the triplet and the two doublet optics: Gradient, magnetic length and aperture radius. The radius is computed as 11max(σ_x, σ_y)+5 mm.

	triplet			short doublet			long doublet		
Name	g[T/m]	L_q[m]	r[mm]	g[T/m]	L_q[m]	r[mm]	g[T/m]	L_q[m]	r[mm]
Q1	19.7	1.34	20	−28.6	1.1	40	−19.1	1.1	36
Q2	−38.8	1.18	32	28.5	1.1	39	17.7	1.1	37
Q3	−3.46	1.18	20	−32.7	1.1	38	−14.7	1.1	41
Q4	22.3	1.34	22	40.0	1.1	38	11.8	1.1	41

7.3.1 Triplet Design

The first electron optics is a round-beam electron optics with $\beta^*_{e;x,y} = 0.1$ m, that can be realized by a plain triplet without any sextupoles. An example optics is shown in Fig. 7.5. Upstream bending magnets complement the separation dipole so as to match the dispersion at the IP. The total length of the system is 90 m. The SR radiation power is small, about 25 kW on the incoming side of the IP, coming almost entirely from the separation dipole before the interaction point. Without any chromatic correction the IP beam size increase for an rms relative momentum spread of $\sigma_\delta = 3 \times 10^{-4}$ is about 9 % horizontally and 21 % vertically, leading to a 14 % luminosity loss.

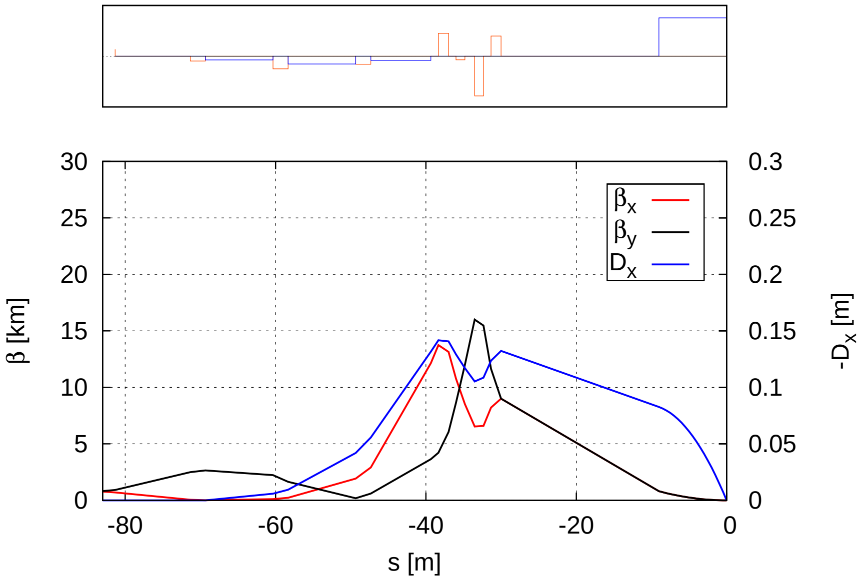

Figure 7.5: Electron final-focus optics for $\beta^*_{x,y}$ = 0.1 m, based on a triplet. Total length is ~ 80 m.

7.3.2 Short Doublet Design

An alternative system is proposed, for use with unequal IP beta functions: $\beta^*_{e;x} = 0.2$ m, $\beta^*_{e;y} = 0.05$ m. The optics consists of a final doublet with local chromatic correction in the two transverse planes. For that, 4 sextupoles are used following the compact final-focus scheme proposed for future linear colliders [41, 42]. The two sextupoles in the high dispersion region perform the chromatic correction and the other two, which are located where $D \approx 0$, are used to compensate for the geometric aberrations generated. Each compensating sextupole is separated in betatron phase by $\Delta\mu_{x,y} = \pi$ from the corresponding sextupole of the same polarity, as in the first correction scheme of Table 1.1.

The dispersion is generated by bending magnets between the quadrupoles. Sextupoles have opposite sign to the quadrupoles next to them, due to the negative sign of the dispersion. The optimization of the strength of the sextupoles has been done by MAPCLASS [87]. This code gives the beam sizes in an analytical way, including high order aberrations, without the need of particle tracking.

The geometric aberrations come from the strength of the sextupoles in compensating the chromaticity created by the doublet. If the dispersion in the final doublet is decreased, the chromaticity can be corrected with a lower strength in the sextupoles, hence generating

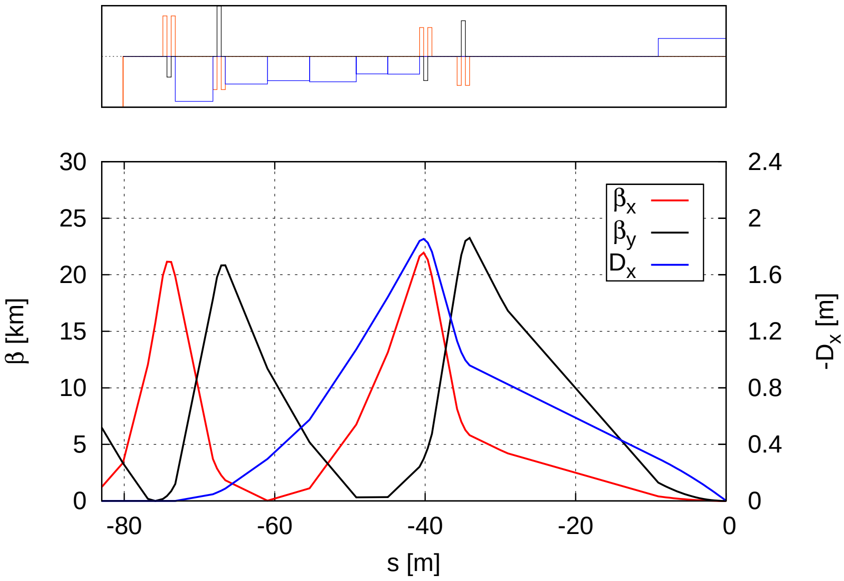

Figure 7.6: Electron final-focus optics for β_x^*/β_y^* = 0.2 m/0.05 m, based on a doublet with local chromatic correction. Total length is ~ 90 m.

less geometric aberrations. For the optics shown the synchrotron radiation power loss is considerable, 500 kW. That is due to the big angles of the bending magnets that generate the required high dispersion in the final doublet within a short space. This problem can be solved by means of extending the total length. Besides, the longer system generates less chromaticity due to the fact that weaker quadrupoles are needed for focusing the beam at the IP.

7.3.3 Long Doublet Design

The optics for a longer doublet design is shown in Fig. 7.7. It has a length of 150 m. The SR power is 84 kW for the entire final focus on the incoming side of the IP, of which only about one third, 24 kW, is due to last separation dipole, with (at least) the same 24 kW again on the outgoing side. With this optics the IP beam size increase for $\sigma_\delta = 3 \times 10^{-4}$ is about 2.3 % horizontally and 2.6 % vertically, only due to optical aberrations. There has been a discrepancy when trying to determine the total beam size increase including the effect of the synchrotron radiation, with the different codes used, that will be explained in Sec. 7.4. However, synchrotron radiation increases the horizontal beam size by 138 %.

An effective way of comparing the two systems is by comparing the beam sizes at different orders, computed by the MAPCLASS code. Figure 7.8 shows the beam sizes for a monochromatic and for a beam with $\sigma_\delta = 3 \times 10^{-4}$, so that the effect of the chromatic aberrations is visible. The first two orders represent the linear effects. The non-linear effects are visible from order 2 and due to the effect of the sextupoles. The strengths were optimized so as to minimize the beam sizes for a beam with $\sigma_\delta \neq 0$ at order 4, even though in this particular case the beams sizes at orders 2,3 and 4 are the same as there are not any element of order higher than 2. If the

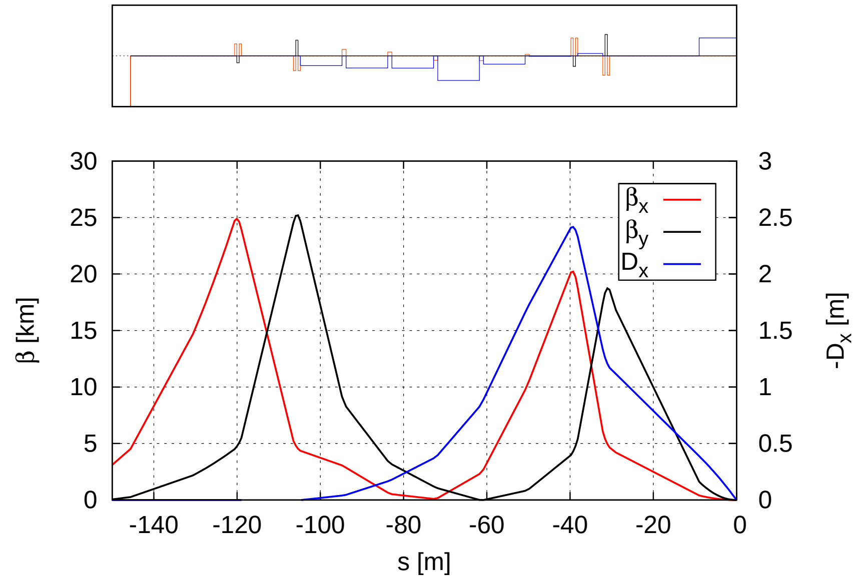

Figure 7.7: Electron final-focus optics for β^*_x/β^*_y = 0.2 m/0.05 m, based on a doublet with local chromatic correction. Total length is ~ 150 m.

strength of the sextupoles is increased, the difference with respect to the monochromatic beam is decreased. However, the non-linear contribution increases, as the geometric aberrations coming from the sextupoles are not so efficiently corrected, thus blowing up the beam size. This effect is discussed with more detail in Sec. 7.4.1. Also, in the opposite case of reducing the strength of the sextupoles, the beam grows in size due to chromaticity while the non-linear effects are decreased.

Figure 7.9 shows the beam sizes for the long doublet. Both geometric and chromatic aberrations are cancelled, showing how a longer system reduces the beam size, due to a larger dispersion in sextupoles and weaker focusing quadrupoles.

7.4 Tracking Simulations and Comparison

The bandwidth of a system illustrates the different aberrations leading to an IP beam size increase. Figure 7.10 represents the dependence of the β-functions at the IP on the momentum offset. This is expressed as the ratio between $\beta^*_{x,y}(\delta)$ and its value for $\delta = 0$, $\beta^*_{x,y;0}$. The bandwidth was computed by MAD-X for a monochromatic beam with zero energy spread and varying offset from the design beam energy, δ. The comparison of this plot with the bandwidth of the long doublet (Fig. 7.11) reveals the benefit of a chromatic correction. Without the sextupoles, the bandwidth for the long doublet is smaller than for the triplet, but when the sextupoles are switched on, it greatly expands.

Table 7.2 summarizes the relative beam-size increase for the triplet and for the long doublet. An indication of the luminosity loss due to the beam size growth of the electrons is

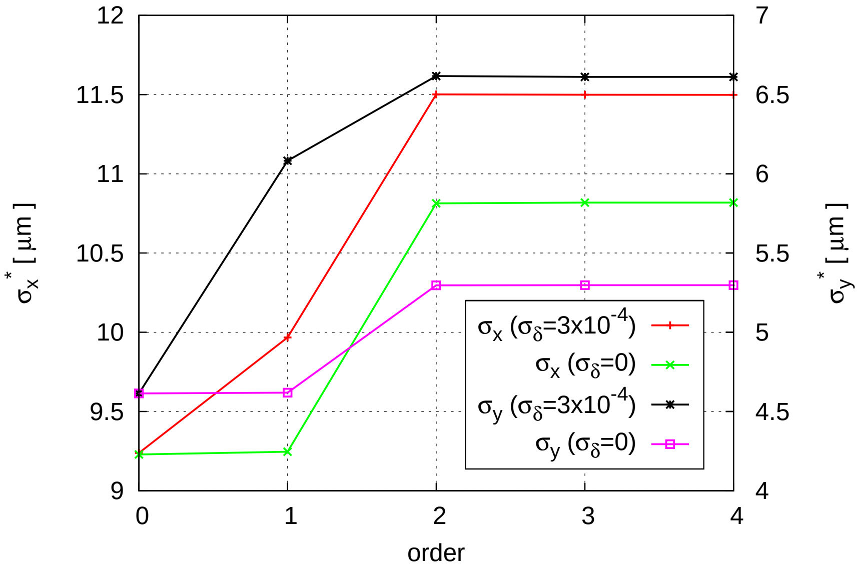

Figure 7.8: Short doublet: beam size at the IP as a function of the order computed by MAPCLASS for a monochromatic beam and for a beam with $\sigma_\delta = 3 \times 10^{-4}$.

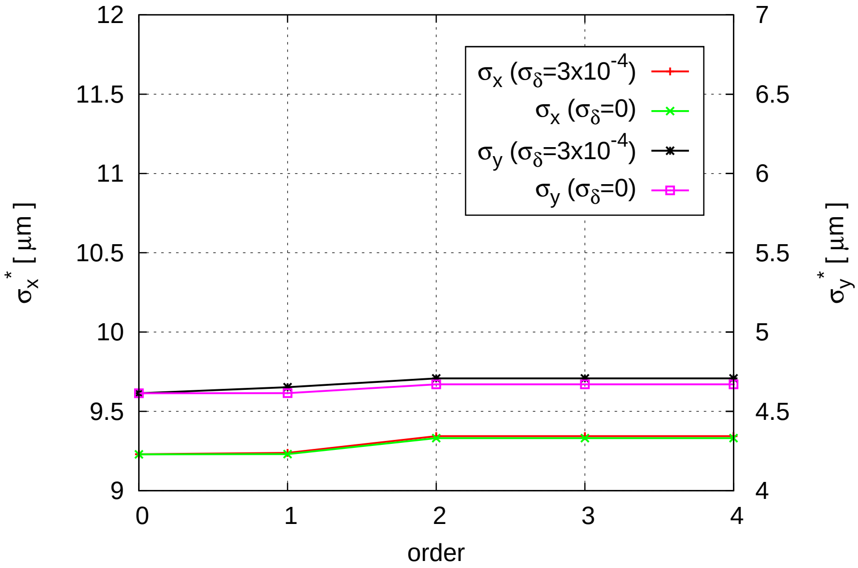

Figure 7.9: Long doublet: beam size at the IP as a function of the order computed by MAPCLASS for a monochromatic beam and for a beam with $\sigma_\delta = 3 \times 10^{-4}$.

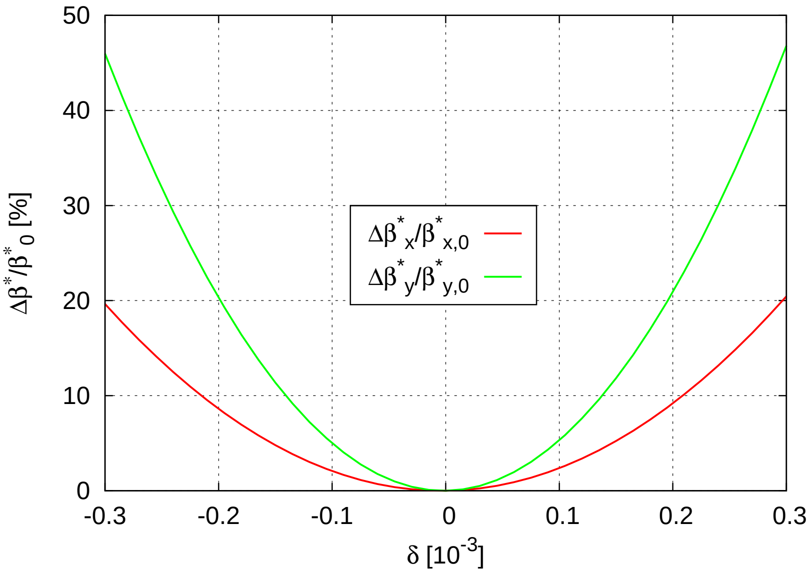

Figure 7.10: Bandwidth plot of the triplet design. Relative variation of $\beta^*_{x,y}$ with momentum offset.

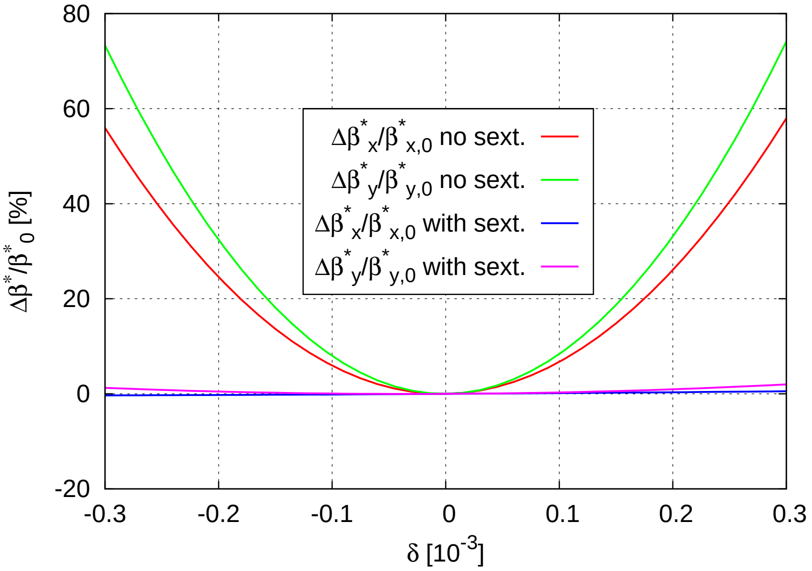

Figure 7.11: Bandwidth plot of the long doublet. Relative variation of $\beta^*_{x,y}$ with momentum offset, comparing the case where the sextupoles are optimized to correct aberrations with that where the sextupoles are switched off.

also given, considering that there is no beam size growth for the proton line. The luminosity for unequal beams is given by replacing the term $4\sigma_x^*\sigma_y^*$ in (1.77) by $2\sqrt{\sigma_{e;x}^{*2}+\sigma_{p;x}^{*2}}\sqrt{\sigma_{e;y}^{*2}+\sigma_{p;y}^{*2}}$ [6]. Then, the relative luminosity loss is given as

$$\frac{L-L_0}{L_0}=2\left[\left(\frac{\sigma_{e;x}^{*2}}{\sigma_{x;0}^{*2}}+1\right)\left(\frac{\sigma_{e;y}^{*2}}{\sigma_{y;0}^{*2}}+1\right)\right]^{-1/2}-1, \tag{7.1}$$

where $\sigma_{e;x,y}^*$ gives the electron beam sizes while $\sigma_{x,y;0}^*$ represents the sizes for protons and leptons in a monochromatic beam (nominal). The tracking has been done with 10^5 particles using PTC-TRACK in the MADX code [88].

Table 7.2: Relative IP electron beam-size increase with respect to the linear spot size $\sigma_{x,y;0}^*=\sqrt{\epsilon_{x,y}\beta_{x,y}^*}$, considering a Gaussian momentum distribution of $\sigma_\delta=3\times10^{-4}$. Results obtained with MAPCLASS and with a tracking of 10^5 particles are compared, for the cases with and without considering the effect of the synchrotron radiation. The luminosity loss is also indicated.

		triplet		short doublet		long doublet	
		mapclass	track.	mapclass	track.	mapclass	track.
no SR	$(\sigma_x^*-\sigma_{x,0}^*)/\sigma_{x,0}^*$	9.6 %	9.1 %	24.5 %	24.5 %	1.23 %	1.34 %
	$(\sigma_y^*-\sigma_{y,0}^*)/\sigma_{y,0}^*$	21.1 %	20.7 %	43.3 %	44.2 %	2.03 %	1.67 %
with SR	$(\sigma_x^*-\sigma_{x,0}^*)/\sigma_{x,0}^*$	–	9.1 %	–	24.1 %	–	2.33 %(*)
	$(\sigma_y^*-\sigma_{y,0}^*)/\sigma_{y,0}^*$	–	20.8 %	–	45.2 %	–	2.56 %
	$(L-L_0)/L_0$	–	−14 %	–	−29 %	–	−2.4 %(*)

We see that there is a good agreement between the values given by MAPCLASS and those given by the particle tracking for the case where the SR radiation is not considered. There is no comparison for the case with SR, as MAPCLASS does not give a result for this case.

(*) There is a disagreement between the values obtained by PLACET (141 %) and with MADX (2.33 %). For the worst case, the luminosity loss is 46 %, this result being in a good agreement with (1.111) (Courtesy of Héctor García).

The chromaticities as tune variation for off-momentum particles have been computed as (1.94) and (1.95), where the integral is done over the IR. The chromaticities for the three designs are presented in Table 7.3. Even though we are not interested in the off-momentum tune variation as the particles are lost, this number gives an indication of the chromaticities.

We see that even though the compensation is good for the long doublet final focus, when the SR effects are included, there is beam size growth (See (1.111)), mainly due to the fact that the dipole length and field are not optimized and that the dipoles are located in regions where the behaviour of the Twiss functions in (1.113) makes $\mathscr{H}$ large.

Another option for the local chromatic correction of the electron line has been proposed, based on a modular chromatic correction, where the chromaticity is compensated in two

Table 7.3: Natural chromaticities and corrected chromaticities for the three designs.

		triplet	short doublet	long doublet
no sext	Q'_x	-102.35	-472	-148
	Q'_y	-159.58	-586	-226
with sext	Q'_x	–	-107	-7.33
	Q'_y	–	-233	-37.9

dedicated sections, each of which corrects the chromaticity in one plane [89]. The separated optics with strictly defined functions makes the system relatively simple to design. However, as the chromaticity is not locally corrected the bandwidth of the system is limited by the off-momentum breakdown of the proper relations between the sextupoles. This option has been studied and compared to the long doublet with local chromatic correction in [90]. The main drawback is that the required length for this system is too large.

7.4.1 Phase Advance Study

The phase advance in the two planes between the two sextupoles of each pair, {sext.1, sext.3} and {sext.2, sext.4} is $\sim \pi$. Table 7.4 presents the deviations of these phase advances from their ideal value between sextupoles for both the short and long doublet optics. In units of π rad, the phase advances in the four cases should ideally be zero. The errors make the transfer matrix be not exactly $-I$, and the aberrations are not perfectly cancelled, growing with the sextupole strength. As a higher dispersion in the long doublet implies weaker sextupoles, the geometric aberration cancellation is better.

Table 7.4: Comparison between the short doublet and the long doublet designs. The first four columns present the errors in the phase advance between sextupoles in a pair; the last two, the integrated sextupole strength of the 4 sextupoles and the dispersion at the location of each sextupole.

	short doublet	long doublet
$\left(1-\lvert\mu_{x,1}-\mu_{x,3}\rvert\right)$ [$10^{-5}\pi$ rad]	130.55	171.33
$\left(1-\lvert\mu_{y,1}-\mu_{y,3}\rvert\right)$ [$10^{-5}\pi$ rad]	58.67	121.96
$\left(1-\lvert\mu_{x,2}-\mu_{x,4}\rvert\right)$ [$10^{-5}\pi$ rad]	113.15	152.98
$\left(1-\lvert\mu_{y,2}-\mu_{y,4}\rvert\right)$ [$10^{-5}\pi$ rad]	25.45	108.08
$\lvert k_{sl1}\rvert, \lvert k_{sl2}\rvert, \lvert k_{sl3}\rvert, \lvert k_{sl4}\rvert$ [m^{-2}]	0.23, 0.16, 0.33, 0.13	0.13, 0.07, 0.10, 0.04
$\lvert D_{x1}\rvert, \lvert D_{x2}\rvert, \lvert D_{x3}\rvert, \lvert D_{x4}\rvert$ [m]	0.99, 1.83, 0.07, 0.00	1.21, 2.39, 0.01, 0.00

7.4.2 Synchrotron Radiation Power

The energy emitted by a particle through a whole passage in a bending magnet of radius ρ_i and length $L_{b,i}$ is obtained by integrating over time the radiation power P (1.109), $E_e = \int_{L_{b,i}} P \cdot dt = P \cdot L_{b,i}/c$. Multiplying E_e by the number of particles per second, I_B/e, and summing over all the bending magnets in the dipoles, we get the total power emitted by the electrons along all the system:

$$P_e = \frac{e}{6\pi\epsilon_0}\left(\frac{E}{m_e c^2}\right)^4 I_B \sum_i \frac{L_{b,i}}{\rho_i^2}, \tag{7.2}$$

where I_B represents beam current. The values obtained with (7.2) are shown in Table 7.5 for the three designs discussed in this chapter, and assuming $I_B = 6.6$ mA. They represent the power emitted until the IP only, including the 9-m dipole integrated in the detector. For a conservative estimation of the total power in all the IR, including the part after the IP, the power emitted by the other 9 meters of the bending magnet after the IP should be added (24.9 kW).

Table 7.5: SR power emitted by the electrons in the interaction region until the IP.

	triplet	short doublet	long doublet
P_e [kW]	26.4	233.7	117.3

The long doublet generates half the synchrotron radiation of the short doublet. The power emitted by one magnet scales as $\sim L_{b,i}/\rho_i^2$, so that the shorter but stronger magnets in the short doublet generate more power, due to the quadratic dependence on the bending radius. For the same reason, both designs consume much more power than the triplet, as for the doublet systems the bending magnets are designed not only to compensate the dispersion of the last separation dipole, but also to generate the dispersion required for the local chromatic correction.

7.5 Conclusions

Different solutions have been proposed and studied for a final-focus system in the electron beam line of he LHeC, from which several conclusions can be drawn:

- A chromatic correction minimizes variations in $\beta^*_{x,y}$ due to off-momentum particles, expanding the β^*-bandwidth.
- A final-focus system with a dedicated chromatic correction section requires a long system, that may not fit in the 200 m available between the exit of the linac and the IP.
- A local chromatic correction section appears to be a good candidate, due to its compactness. Its efficiency to correct the aberrations depends on the length. For an optimal correction of the aberrations (without taking into account the effect of the synchrotron radiation) the required length is less than 200 m.
- The beam size dilution due to the SR emission is an essential ingredient. Tracking simulations show that for the local chromatic system, the luminosity loss due to this effect is unacceptably large, even in the case of the long doublet solution. The system

should be optimized to minimize $\mathscr{H}$ in the bending magnets, and to, thereby, reduce the horizontal beam size at the IP.

- Finally, the system may be optimized further by fine-tuning the phase advance between sextupoles. This would allow lowering the dispersion at the sextupole magnets and thus the SR emission.

8. Summary and Final Conclusions

A novel interaction region scheme for a luminosity upgrade of the LHC has been designed and studied, based on flat beams, large Piwinski angle, and optional crab waist. The possibility of a local chromatic correction in the LHC has been demonstrated for the vertical plane. The new scheme provides the lowest vertical β^* ever considered for the LHC, together with a high ratio between the horizontal and the vertical IP beta functions.

A key ingredient of the pertinent interaction region is the new magnetic element required, a double-half quadrupole (DHQ). In order to maximize the quadrupole gradient of this element so as to perform the tight focusing, the beams must be separated transversely, implying an excessive luminosity loss through the geometric luminosity reduction factor. On the other hand, the large sextupolar strength of the DHQ is difficult to compensate. Therefore, the beam brightness must be increased beyond the specifications of the planned LHC Injector Upgrade, in order to achieve a luminosity gain. A new design of the DHQ exhibiting a larger ratio between the quadrupole and the sextupole terms at the position of the beams would solve the problem of the aberration compensation and would allow for higher luminosities at lower brightness.

In addition, the symmetric optics required for the aberration compensation and for the crab-waist collisions implies that the interaction-region quadrupole magnets should be of opposite polarity for the two beams. These magnets, including the DHQ and the new separation magnets should be built specifically for this optics, suggesting the need for targeted R&D.

For all the reasons explained above, this scheme is not recommended for the HL-LHC, as it requires major hardware changes, i.e. more changes than the baseline option of the HL-LHC, which like the present LHC makes use of a triplet as a final focus system and distributed chromatic correction. The proposed scheme allows operating with beams of higher brightness that would be above the beam-beam limit for a conventional collision scheme. However, the brightness values needed for a considerable luminosity increase are still far from being achieved.

Regardless, this scheme, or a variation thereof, should be taken into account as a promising future option for a new high energy hadron collider (HE-LHC or VHE-LHC), where the very high energies of the particles have a direct effect on the parameter evolution during the store, due to synchrotron radiation (SR). In particular the large Piwinski angle allows profiting from the SR-induced strong emittance damping. This removes the need for continually applying an intentional emittance blow up which would be detrimental for the luminosity. In addition, the β-ratio at the IP could be relaxed by choosing an operation mode with unequal horizontal and vertical emittance. This could render this optics more feasible.

In particular, a symmetric IR appears to be a natural option for a proton-antiproton collider. The difference is that for such a collider a large crossing angle would not be necessary, so that the luminosity loss coming from the expected less populated antiproton bunches is partially compensated.

Finally, for the LHeC final-focus, the local chromatic correction is the best option. A triplet without local chromatic correction presents a larger beam size growth at the IP, though it is much simpler and requires fewer magnetic elements than one with a chromatic correction. However, the benefit of the chromatic correction is visible in the enlarged momentum bandwidth and smaller emittance dilution. The much better performance with a local chromatic correction becomes evident when simulating colliding beams with a momentum offset.

In conclusion, the studies performed in this thesis, and the novel principles presented here, provide a solid foundation for the interaction-region design of future highest-energy colliders.

A. Transfer Maps

A transfer map is an operator, or set of operators, that relate the state of a particle at two different instants. That is, from an initial state at $s = s_1$: $\boldsymbol{z_1} \equiv (x, x', y, y', \delta)|_{s=s_1}$ we can get the state at $s = s_2$: $\boldsymbol{z}_2 \equiv (x, x', y, y', \delta)|_{s=s_2}$. Each variable of the final state is related to the variables of the initial one as follows:

$$z_{i,2} = K_i + \sum_j R_{ij} z_{j,1} + \sum_{jk} T_{ijk} z_{j,1} z_{k,1} + \sum_{jkl} U_{ijkl} z_{j,1} z_{k,1} z_{l,1} + ... \tag{A.1}$$

where the operators K_i, R_{ij}, T_{ijk}, U_{ijkl} are the maps at zero, first, second and third order.

A.1 Single Particle Tracking

Once the map is known, the particles can be tracked from the initial to the final position. In order to know the beam evolution in terms of the beam variables (1.72), one must generate a particle distribution with $\boldsymbol{\sigma_1} = (\sigma_x, \sigma'_x, \sigma_y, \sigma'_y, \sigma_\delta)|_{s=s_1}$ in the initial point, whose probability density function normalized to the number of particles (N) is

$$n(x, x', y, y', \delta) = N \frac{e^{-x^2/2\sigma_x^2} e^{-x'^2/2\sigma_x'^2} e^{-y^2/2\sigma_y^2} e^{-y'^2/2\sigma_y'^2} e^{-\delta^2/2\sigma_\delta^2}}{(2\pi)^{5/2}\, \sigma_x\, \sigma_y\, \sigma'_x\, \sigma'_y\, \sigma_\delta} \tag{A.2}$$

After the particle distribution has been generated, one must track these particles one by one and treat the final data to determine the beam distribution at the final point, $\boldsymbol{\sigma_2} = (\sigma_x, \sigma'_x, \sigma_y, \sigma'_y, \sigma_\delta)|_{s=s_2}$. The error is minimized by tracking a large number or particles, increasing the computing time. A compromise must be found between precision and time.

A.2 Beam Tracking: MAPCLASS

The drawback in the particle tracking is the time needed for the particle tracking, that does not easily allow for an optimization. An analytical tracking can be done, that allows one to pass directly form the initial to the final beam variables [91]. Each final beam variable $\sigma_{i,2}$ is

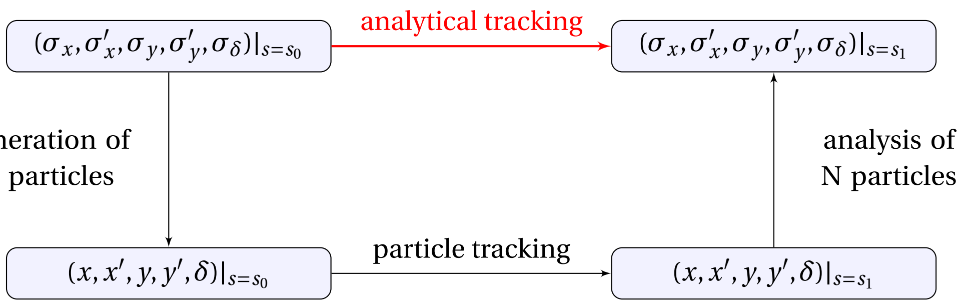

Figure A.1: Diagram comparing the analytical and the particle tracking.

computed through the maps and all the initial beam variables,

$$\sigma_{i,2} = f(K_i, R_{ij}, T_{ijk}, U_{ijkl}, \ldots, \sigma_{x,1}, \sigma'_{x,1}, \sigma_{y,1}, \sigma'_{y,1}, \sigma_{\delta,1}). \tag{A.3}$$

Figure A.1 compares the two tracking methods. Once the map (A.1) is generated, and the initial state in the phase space defined ($\boldsymbol{\sigma_1}$), MAPCLASS makes the analytical tracking to get the final state, $\boldsymbol{\sigma_2}$. This process can be incorporated to an optimization routine in order to, for example, minimize the beam size at a certain order. A particle tracking is then used after the optimization process to confirm the results.

A.3 Transfer Matrix between Elements

The operator R_{ij} in (A.1), as a linear operator, can be expressed as a matrix. If we assume there is no coupling between the horizontal and the vertical planes, and there is no change in the energy of the particle:

$$R = \begin{pmatrix} R_{11} & R_{12} & 0 & 0 & R_{15} \\ R_{21} & R_{22} & 0 & 0 & R_{25} \\ 0 & 0 & R_{33} & R_{34} & R_{35} \\ 0 & 0 & R_{43} & R_{44} & R_{45} \\ 0 & 0 & 0 & 0 & 1 \end{pmatrix}, \tag{A.4}$$

and this motivates the introduction of an independent matrix for each plane

$$M_x = \begin{pmatrix} R_{11} & R_{12} \\ R_{21} & R_{22} \end{pmatrix}; \qquad M_y = \begin{pmatrix} R_{33} & R_{34} \\ R_{43} & R_{44} \end{pmatrix}. \tag{A.5}$$

By assuming there is no coupling between the planes, the horizontal, $\boldsymbol{x} = (x, x')$ and vertical, $\boldsymbol{y} = (y, y')$, coordinates can be mapped independently as

$$\boldsymbol{x_2} = M_x \boldsymbol{x_1} + \begin{pmatrix} R_{15} \\ R_{25} \end{pmatrix} \delta; \qquad \boldsymbol{y_2} = M_y \boldsymbol{y_1} + \begin{pmatrix} R_{35} \\ R_{45} \end{pmatrix} \delta. \tag{A.6}$$

The matrices $M_{x,y}$ can be computed if the optical functions in the initial and in the final point, $(\beta_1, \alpha_1, \mu_1, \beta_2, \alpha_2, \mu_2)$ are known. The matrix in each plane is [1, Sec. 5.3]

$$M = \begin{pmatrix} \sqrt{\beta_2/\beta_1}(\cos\Delta\mu + \alpha_1 \sin\Delta\mu) & \sqrt{\beta_1\beta_2}\sin\Delta\mu \\ -\frac{1}{\sqrt{\beta_1\beta_2}}[(\alpha_2 - \alpha_1)\cos\Delta\mu + (1 + \alpha_1\alpha_2)\sin\Delta\mu] & \sqrt{\beta_1/\beta_2}(\cos\Delta\mu - \alpha_2 \sin\Delta\mu) \end{pmatrix}, \tag{A.7}$$

where the functions (β, α, μ) are referred to the respective plane and $\Delta\mu = \mu_2 - \mu_1$.

Bibliography

[1] H. Wiedemann, “Particle accelerator physics,” Springer, 2007.

[2] E. D. Courant and H. S. Snyder, “Theory of the alternating gradient synchrotron,” Annals Phys. **3** (1958) 1 [Annals Phys. **281** (2000) 360].

[3] G. W. Hill, “On the part of the motion of the lunar perigee which is a function of the mean motions of the sun and moon,” Cambridge, Mass., Press of J. Wilson and son, 1877.

[4] M. Giovannozzi, “Sources of emittance growth,” CAS 2003; Chios, Greece.

[5] A. Piwinski, “Intrabeam scattering,” In *Noordwijkerhout 1991, Proceedings, Advanced accelerator physics* 226-242. (see HIGH ENERGY PHYSICS INDEX 30 (1992) No. 9905).

[6] W. Herr and B. Muratori, “Concept of luminosity,” CAS 2003; Zeuthen, Germany.

[7] R. Helm and J. Irwin, “Final focus systems for linear colliders,” In *Ottawa 1992, Proceedings, Linear accelerator, vol. 1* 258-262. and SLAC Stanford - SLAC-PUB-5876 (92/08,rec.Nov.) 5 p. C

[8] W. Scandale and F. Zimmermann, “Two scenarios for the LHC luminosity upgrade,” In Special meeting Protons Accelerators for the future, April 2007.

[9] J. L. Laclare, “Introduction To Coherent Instabilities - Coasting Beam Case,” In *Gif-sur-yvette 1984, Proceedings, General Accelerator Physics, Vol. 2*, 377-414.

[10] H. Mais and C. Mari, “Introduction to beam-beam effects,” DESY-M-91-04.

[11] J. L. Abelleira Fernandez *et al.* [LHeC Study Group Collaboration], “A Large Hadron Electron Collider at CERN: Report on the Physics and Design Concepts for Machine and Detector,” J. Phys. G **39** (2012) 075001 [arXiv:1206.2913 [physics.acc-ph]].

[12] P. Raimondi and M. Zobov, “Tune shift in beam-beam collisions with a crossing angle,” DAFNE-TECHNICAL-NOTE-G-58.

[13] F. Ruggiero and F. Zimmermann, “Luminosity optimization near the beam-beam limit by increasing bunch length or crossing angle,” Phys. Rev. ST Accel. Beams **5** (2002) 061001.

[14] K. Ohmi, “Beam-beam Limit in a Hadron Collider,” Conf. Proc. C **1205201** (2012) 3208.

[15] V. Shiltsev, “Beam-beam observations in the Tevatron,” ICFA Mini-Workshop on Beam-Beam Effects in Hadron Colliders. February 18-22; 2013, CERN, Switzerland.

[16] “LEP Design Report: Vol. 2. The LEP Main Ring,” CERN-LEP-84-01.

[17] W. Herr et al, “Results of long-range beam-beam studies – scaling with beam separation and intensity,” CERN-ATS-Note-2012-070 (2012).

[18] K. Ville, “Synchrotron radiation,” JUAS 2011, Archamps, France.

[19] M. Aicheler (.ed), P. Burrows, M. Draper, T. Garvey, P. Lebrun, K. Peach and N. Phinney *et al.*, “A Multi-TeV Linear Collider Based on CLIC Technology : CLIC Conceptual Design Report,” CERN-2012-007.

[20] K. Buesser, “The International Linear Collider,” arXiv:1306.3126 [physics.acc-ph].

[21] A. Blondel and F. Zimmermann, “A High Luminosity e^+e^- Collider in the LHC tunnel to study the Higgs Boson,” arXiv:1112.2518.

[22] M. Koratzinos, A. P. Blondel, R. Aleksan, O. Brunner, A. Butterworth, P. Janot, E. Jensen and J. Osborne *et al.*, “TLEP: A High-Performance Circular e+e- Collider to Study the Higgs Boson,” arXiv:1305.6498 [physics.acc-ph].

[23] F. Zimmermann, “A simulation study of electron-cloud instability and beam-induced multipacting in the LHC,” LHC Project-Report 95, 1997.

[24] M. Sands, “Emittance Growth From Radiation Fluctuations,” SLAC/AP-047.

[25] ATLAS detector and physics performance : Technical Design Report, 1 CERN-LHCC-99-014.

[26] CMS Physics : Technical Design Report Volume 1: Detector Performance and Software, CERN-LHCC-2006-001.

[27] S. Chatrchyan *et al.* [CMS Collaboration], “A new boson with a mass of 125-GeV observed with the CMS experiment at the Large Hadron Collider,” Science **338** (2012) 1569.

[28] O. S. Bruning, P. Collier, P. Lebrun, S. Myers, R. Ostojic, J. Poole and P. Proudlock, “LHC Design Report. 1. The LHC Main Ring,” CERN-2004-003-V-1.

[29] W. Herr, “Dynamic behaviour of nominal and PACMAN bunches for different LHC crossing schemes,” CERN LHC Project Report 856 (2005).

[30] A. Faus-Golfe, “Looking for a symmetric LHC low-beta insertion,” LHC note 336, 1995.

[31] W. Scandale, “Revisiting the Problem of the LHC Insertion Symmetry,” CERN SL/Note 94-42 (AP), 1994.

[32] B. Autin, “Dispersion Suppression With Missing Magnets In A Fodo Structure - Application To The Cern Anti-proton Accumulator. (talk),” IEEE Trans. Nucl. Sci. **26** (1979) 3493.

[33] K. Schindl, “The injector chain for the LHC,” CERN-PS-99-018-DI.

[34] A. Faus-Golfe, R. de Maria, R. Tomas; “Limits on Chromaticity correction,” LHC-LUMI-06 Proceedings.

[35] W. Herr *et al.*, “Head-on beam-beam tune shifts with high brightness beams in the LHC,” CERN-ATS-Note-2011-029 (2011).

[36] B.J. Holzer *et al.*, “Optics design and lattice optimization for the LHC,” Proc. IPAC’13 Shanghai, China.

[37] R. Calaga, “Crab Cavities for the LHC Upgrade,” Proceedings of Chamonix 2012 workshop on LHC Performance.

[38] J. P. Koutchouk, “Luminosity Optimization and leveling,” Proceedings of Chamonix 2012 workshop on LHC Performance.

[39] E. Todesco, F. Zimmermann (eds.), “The High-Energy Large Hadron Collider,” Proc. EuCARD-AccNet-EuroLumi Workshop. Malta, Oct. 2010, CERN-2001-003.

[40] S. D. Fartoukh, “An Achromatic Telescopic Squeezing (ATS) Scheme for LHC Upgrade,” Conf. Proc. C **110904** (2011) 2088.

[41] P. Raimondi and A. Seryi, “A Novel final focus design for high-energy linear colliders,” SLAC-PUB-9722.

[42] P. Raimondi and A. Seryi, “A Novel final focus design for future linear colliders,” Phys. Rev. Lett. **86** (2001) 3779.

[43] C. J. Johnstone, “Local chromaticity correction of the LHC,” Conf. Proc. C **970512** (1997) 119.

[44] R. de Maria, O. S. Bruning and P. Raimondi, “LHC IR upgrade: A dipole first option with local chromaticity correction,” Conf. Proc. C **060626**, 571 (2006).

[45] Y. Alexahin *et al.* [Neutrino Factory and Muon Collider Collaboration], “Muon Collider Lattice with Local Interaction Region Chromaticity Correction,” FERMILAB-CONF-09-161-APC.

[46] S. Fartoukh, “Prospective for flat beam optics,” Presented at LHC MAC 15-17 June 2006.

[47] M. Solfaroli and J. Wenninger, private communication.

[48] C. M. Bhat *et al.* [LARP Collaboration], “LHC luminosity upgrade with large Piwinski angle scheme: a recent look,” Conf. Proc. C **110904** (2011) 1879 [arXiv:1201.5905 [physics.acc-ph]].

[49] K. Ohmi and K. Oide, “Chaos and emittance growth due to nonlinear interactions in a circular accelerator,” Phys. Rev. ST Accel. Beams **10** (2007) 014401.

[50] K. Ohmi, “Study of beam-beam interaction with a large Piwinski angle at LHC,” CERN-2008-005.

[51] J.L. Abelleira *et al.*, “Large Piwinski angle,” CERN-ATS-Note-2012-091 MD.

[52] K. Cornelis, W. Herr and M. Meddahi, “Proton anti-proton collisions at a finite crossing angle in the SPS,” Conf. Proc. C **910506** (1991) 153.

[53] K. Ohmi, “Large Piwinski Angle studies,” contribution to CARE-HHH working meeting-LHC beam-beam and beam compensation. August 28, 2008, CERN, Switzerland.

[54] D. V. Pestrikov, “Vertical synchrobetatron resonances due to beam-beam interaction with horizontal crossing,” Nucl. Instrum. Meth. A **336** (1993) 427.

[55] P. Raimondi, D. N. Shatilov and M. Zobov, “Beam-Beam Issues for Colliding Schemes with Large Piwinski Angle and Crabbed Waist,” physics/0702033 [PHYSICS].

[56] C. Milardi, D. Alesini, M. E. Biagini, C. Biscari, A. Bocci, M. Boscolo, F. Bossi and B. Buonomo *et al.*, “Experience with DAFNE upgrade including crab waist,” PAC09-MO4RAI01.

[57] M. Zobov, P. Raimondi, D. Shatilov and K. Ohmi, “Crab Waist Collision Studies for e+ e- Factories,” arXiv:0802.2667 [physics.acc-ph].

[58] C. Milardi, M. A. Preger, P. Raimondi and F. Sgamma, “High luminosity interaction region design for collisions inside high field detector solenoid,” JINST **7** (2012) T03002 [arXiv:1110.3212 [physics.acc-ph]].

[59] Methodical Accelerator Design - X
http://cern.ch/madx.

[60] F. Bossi, “The KLOE-2 project,” J. Phys. Conf. Ser. **171** (2009) 012099.

[61] P. Raimondi, “Crab waist options for LHC,” contribution to CARE HHH APD Workshop on Interaction Regions for the LHC Upgrade, DAFNE and SuperB (IR’07). Frascati, Italy, 6-9 November 2007.

[62] K. Ohmi, “A crab-waist scheme for the LHC,” contribution to CARE-HHH working meeting-LHC beam-beam and beam compensation. August 28, 2008, CERN, Switzerland.

[63] D. Shatilov, E. Levichev, E. Simonov and M. Zobov, “Application of frequency map analysis to beam-beam effects study in crab waist collision scheme,” Phys. Rev. ST Accel. Beams **14** (2011) 014001 [arXiv:1002.3733 [physics.acc-ph]].

[64] J. Laskar, “The chaotic motion of the solar system: A numerical estimate of the size of the chaotic zones,” Icarus **88** (1990) 266.

[65] O. S. Bruning, “HL-LHC Parameter Space and Scenarios,” Proccedings of Chamonix 2012 workshop on LHC performance.

[66] D. Shatilov and M. Zobov, “Beam-beam collisions with an arbitrary crossing angle: analytical tune shifts, tracking algorithm without Lorentz boost, crab-crossing,” ICFA Beam Dyn. Newslett. **37** (2005) 99.

[67] D. Shatilov, “Beam-beam simulations for crabbed bunches,” ICFA Beam Dyn. Newslett. **52** (2010) 42.

[68] J. L. Abelleira, R. Tomas, F. Zimmermann, N. R. Bernard and S. Russenschuck, “Design Status of LHeC Linac-Ring Interaction Region,” Conf. Proc. C **110904** (2011) 2796.

[69] E. Bondarchuk, N. Doinikov, B. Kitaev, V. Korshakov, N. Kozhukhovskaya, V. Krasnoperov, V. Lokiev and N. Maksimenkova *et al.*, “Normal conducting QM quadrupole for the HERA luminosity upgrade,” Conf. Proc. C **980622** (1998) 1972.

[70] K. Kanazawa, H. Nakayama, T. Ogitsu, N. Ohuchi, T. Ozaki, K. Satoh, R. Sugahara and M. Tawada *et al.*, “The interaction region of KEKB,” Nucl. Instrum. Meth. A **499** (2003) 75.

[71] S. Fartoukh, “A semi-analytical method to generate an arbitrary 2D magnetic field and determine the associated current distribution,” CERN-LHC-PROJECT-REPORT-1012.

[72] S. Russenschuck, “Field computation for accelerator magnets: Analytical and numerical methods for electromagnetic design and optimization,” Wiley 2010, ISBN: 978-3-527-40769-9.

[73] G. Sterbini, “An Early Separation Scheme for the LHC Luminosity Upgrade,” CERN-THESIS-2009-136, EPFL-THESIS-4574.

[74] S. M. White, R. Calaga and R. Miyamoto, “Synchro-Betatron Effects in the Presence of Large Piwinski Angle and Crab Cavities at the HL-LHC,” Conf. Proc. C **1205201** (2012) 190.

[75] K. Oide, “SuperTRISTAN. A possibility of ring collider for Higgs factory,” KEK Seminar, 13 February 2012.

[76] V. I. Telnov, “Restriction on the energy and luminosity of e^+e^- storage rings due to beamstrahlung,” Phys. Rev. Lett. **110** (2013) 114801 [arXiv:1203.6563 [physics.acc-ph]].

[77] J. Van Nugteren, “Concept studies for 20 T dipole magnets,” contribution to joint EuCARD-HiLumi-Snowmass Workshop on “Frontier Capabilities for Hadron Colliders.” February 22-23; 2013, CERN, Switzerland.

[78] E. Todesco, “Dipole magnets for HE LHC,” contribution to joint EuCARD-HiLumi-Snowmass Workshop on “Frontier Capabilities for Hadron Colliders,” February 22-23; 2013, CERN, Switzerland.

[79] R. Assmann, R. Bailey, O. Bruning, O. Dominguez, G. de Rijk, J.M. Jimenez, S. Myers, L. Rossi, L. Tavian, E. Todesco, F. Zimmermann, “First Thoughts on a Higher-Energy LHC,” CERN-ATS-Note-2010-177.

[80] L. Rossi and F. Zimmermann, contributions to joint EuCARD-HiLumi-Snowmass Workshop on “Frontier Capabilities for Hadron Colliders,” February 22-23; 2013, CERN, Switzerland.

[81] O. Dominguez, “Electron cloud studies for the LHC and future proton colliders,” EPFL-Thesis.

[82] T. Toyama, D. Arakawa, S. Igarashi, J. Kishiro, E. Nakamura, H. Someya, K. Takayama and Y. Shimosaki, “Bunch shaping by rf voltage modulation with a band-limited white signal: Application to the KEK-PS,” Proceedings of EPAC 2000, Vienna, Austria.

[83] O. Dominguez, “HE-LHC/VHE-LHC parameters, time evolutions & integrated luminosities,” contribution to joint EuCARD-HiLumi-Snowmass Workshop on “Frontier Capabilities for Hadron Colliders.” February 22-23; 2013, CERN, Switzerland.

[84] P. McIntyre and A. Sattarov, “PETAVAC: 100 TeV Proton-Antiproton Collider in SSC Tunnel,” PAC09-WE6PFP041.

[85] D. McGinnis, “P pbar option-Tevatron experience, accelerator complex, recycler scheme, beam separation, state of the art of p-pbar production,” contribution to joint EuCARD-HiLumi-Snowmass Workshop on “Frontier Capabilities for Hadron Colliders.” February 22-23; 2013, CERN, Switzerland.

[86] A. Verdier, “Alignment optics for LHC,” LHC Project Note 325 (2003).

[87] R. Tomas, “MAPCLASS: a code to optimize high order aberrations,” CERN AB-Note-2006-017 (ABP) (2006).

[88] F. Schmidt, “MAD-X PTC integration,” Conf. Proc. C **0505161** (2005) 1272.

[89] K. Oide, “Design of Optics for the Final Focus Test Beam at SLAC,” Conf. Proc. C **8903201** (1989) 1319.

[90] J. L. Abelleira, R. Tomas, F. Zimmermann and H. Garcia, “Final-Focus Optics for the LHeC Electron Beam Line,” Conf. Proc. C **1205201** (2012) 1861.

[91] R. Tomas, “Nonlinear optimization of beam lines,” Phys. Rev. ST Accel. Beams **9** (2006) 081001.